

**LABORATORY INVESTIGATIONS OF AITKEN MODE PARTICLE  
GROWTH BY  $\alpha$ -PINENE OZONOLYSIS**

by

Justin M. Krasnomowitz

A dissertation submitted to the Faculty of the University of Delaware in partial fulfillment of the requirements for the degree of Doctor of Philosophy in Chemistry and Biochemistry

Fall 2019

© 2019 Justin M. Krasnomowitz  
All Rights Reserved

**LABORATORY INVESTIGATIONS OF AITKEN MODE PARTICLE  
GROWTH BY  $\alpha$ -PINENE OZONOLYSIS**

by

Justin M. Krasnomowitz

Approved: \_\_\_\_\_  
Brian Bahnson, Ph.D.  
Chair of the Department of Chemistry and Biochemistry

Approved: \_\_\_\_\_  
John A. Pelesko, Ph.D.  
Dean of the College of Arts and Sciences

Approved: \_\_\_\_\_  
Douglas J. Doren, Ph.D.  
Interim Vice Provost for Graduate and Professional Education and  
Dean of the Graduate College

I certify that I have read this dissertation and that in my opinion it meets the academic and professional standard required by the University as a dissertation for the degree of Doctor of Philosophy.

Signed:

---

Murray V. Johnston, III, Ph.D.  
Professor in charge of dissertation

I certify that I have read this dissertation and that in my opinion it meets the academic and professional standard required by the University as a dissertation for the degree of Doctor of Philosophy.

Signed:

---

Karl S. Booksh, Ph.D.  
Member of dissertation committee

I certify that I have read this dissertation and that in my opinion it meets the academic and professional standard required by the University as a dissertation for the degree of Doctor of Philosophy.

Signed:

---

Lars Gundlach, Ph.D.  
Member of dissertation committee

I certify that I have read this dissertation and that in my opinion it meets the academic and professional standard required by the University as a dissertation for the degree of Doctor of Philosophy.

Signed:

---

George W. Luther, III, Ph.D.  
Member of dissertation committee

## ACKNOWLEDGMENTS

First, I would like to thank my research advisor Dr. Murray Johnston for his incredible support and guidance throughout my time at the University of Delaware. This dissertation and my development as an analytical chemist would not have been possible without him. I would also like to thank the rest of my dissertation committee, Dr. Karl Booksh, Dr. Lars Gundlach and Dr. George Luther for their valuable time and insight during committee meetings.

I would like to thank Dr. Shanhu Lee, Lee Tiszenkel and Qi Ouyang for their collaboration on various projects. Discussions of various results was incredibly helpful in moving work forward. This work would also not be possible without the funding and support from the National Science Foundation.

I need to thank all the other members of the Johnston Group that I had the opportunity to work with. Every member has helped me to grow and I am grateful for all the memories I have of working in the lab. I would especially like to thank Dr. Andrew Horan for helping me become accustomed to aerosol research from my first day, Dr. Chris Stangl for the countless hours of collaboration working on the flow tube and even more laughs along the way and finally, Michael Apsokardu for all of his invaluable help along the way along with daily coffee trips.

Finally, I would like to thank all my friends and family. My parents, Rich and Michele and sister Courtney for their unending support. My grandparents, Donald and Elizabeth Cox for always believing in me and lastly my girlfriend Tori for always staying by my side and reminding me that anything is possible.

## TABLE OF CONTENTS

LIST OF TABLES .....	vii
LIST OF FIGURES .....	viii
ABSTRACT .....	xii
Chapter	
1 INTRODUCTION .....	1
1.1 Current Understanding of Atmospheric Aerosols .....	1
1.2 Environmental Effects of Aerosol .....	3
1.3 Health Effects of Aerosol .....	5
1.4 New particle Formation .....	5
1.5 Particle Growth by Organics .....	7
1.6 Studying Particle Growth in the Laboratory .....	12
1.7 Scope of This Dissertation .....	14
REFERENCES .....	15
2 EXPERIMENTAL METHODOLOGY .....	20
2.1 Scanning Mobility Particle Sizer .....	20
2.2 Flow Tube Reactor .....	22
2.3 Condensation Growth Chamber .....	26
2.4 Composition Measurements .....	27
REFERENCES .....	30
3 GROWTH OF AITKEN MODE AMMONIUM SULFATE PARTICLES BY $\alpha$ -PINENE OZONOLYSIS .....	31
3.1 Atmospheric Effects of Aitken Mode Particles .....	31
3.2 Flow Tube Reactor to Study Particle Growth .....	34
3.3 Simulations of Flow Within the Flow Tube Reactor .....	37
3.4 Particle Growth Experiments .....	39
3.5 Kinetic Modeling of Particle Growth .....	41
3.6 Particle Growth Measurements .....	46
3.7 Mechanism of Particle Growth .....	53

3.8	Comparison of Yields Based on Gas vs. Particle Phase Measurements	. 60
3.9	Conclusions	62
REFERENCES		63
4	EFFECT OF REALTIVE HUMIDITY ON AITKEN MODE PARTICLE GROWTH	69
4.1	Growth of Particles Under High Relative Humidity Conditions	69
4.2	Experimental Modifications For High Relative Humidity Experiments	71
4.3	Experimental Measurements of Particle Growth	77
4.4	Kinetic Modeling of Measured Growth Enhancement	84
4.5	Particle Composition Measurements	90
4.6	Conclusion	92
REFERENCES		93
5	CONCLUSSIONS AND FUTURE DIRECTIONS	97
REFERENCES		103
Appendix		
A	LIST OF ACRONYMS	104
B	COPYRIGHTS	106

## LIST OF TABLES

Table 1-1 Common biogenic precursors known to contribute to SOA. <sup>a</sup> HOM Yields taken from reference 20. ....	8
Table 1-2 Comparison of reactant mixing ratios used for flow tube reactor experiments in this dissertation compared to ambient mixing ratios. Ambient mixing ratios taken from reference 20. ....	14
Table 2-1 explanation of mole fraction apportionment for NAMS data. ....	28
Table 3-1. Molar Yield of Condensable Molecules From $\alpha$ -Pinene Ozonolysis .....	59

## LIST OF FIGURES

Figure 1-1. Ambient concentrations of particles. Adapted from reference 2.....	2
Figure 1-2. An illustration of how particles cool the Earth by reflecting light from the sun.....	4
Figure 1-3. Generalized process of CCN formation in the atmosphere by growth of secondary organic aerosol. ....	5
Figure 1-4. Overview of NPF and particle growth into CCN activation. Adapted from reference 14 .....	6
Figure 1-5. Simplified reaction scheme showing various pathways of $\alpha$ -pinene ozonolysis. Adapted from references 21-24.....	11
Figure 2-1. Schematic of the scanning mobility particle sizer (SMPS). ....	20
Figure 2-2. Schematic of a differential mobility analyzer (DMA) demonstrating how positively charged particles are size selected based on mobility diameter. ....	22
Figure 2-3. Cartoon showing the general layout of the flow tube reactor and how particles grow as they pass through the tube. Blue circles represent size selected ammonium sulfate and the green represents organics condensing onto the particle phase growing the seeds.....	23
Figure 2-4. Cartoon of particle charge states distribution and the effect of a second radioactive neutralizer before the measurement SMPS on the measured particle size distribution. ....	25
Figure 2-5. Schematic of the condensation growth chamber (CGC) and demonstrating how the three different temperature regions create a supersaturation of water vapor causing condensation onto particles. ....	26
Figure 3-1. Experimental setup and flow tube reactor. Flow A contains seed particles and ozone while Flow B contains $\alpha$ -pinene vapor and hydrogen gas.....	35

Figure 3-2. Residence time distribution of particles exiting flow tube. Dark line shows average distribution of five trials. The gray shaded region represents one standard deviation. The blue line represents the modeled residence time using the particle tracing module in COMSOL. ....	36
Figure 3-3. Calculated velocity through the flow tube shown as vertical slices along the length of the reactor. ....	37
Figure 3-4. HOM mixing ratio over time under different CS conditions. ....	44
Figure 3-5. Calculated mixing ratio (a) and exposure (b) of HOMs for each ozone concentration over the residence time of the flow tube. These plots used a molar yield of 12.5% for $\alpha$ -pinene ozonolysis with wall loss modeled as a constant diameter and condensation sink (seed particles of 40 nm) for the experiment shown in Figure 3-5. ....	45
Figure 3-6. Growth experiment of 40 nm ammonium sulfate seed particles. At the top is a contour plot of aerosol size distribution measured by SMPS, followed by ozone mixing ratio, median particle diameter, volume and particle number concentration exiting the flow tube. The green vertical line indicates when $\alpha$ -pinene vapor injection began. Gray vertical lines indicate when increments of the ozone mixing ratio were made. Dots represent raw data and the black lines are ten-point moving averages. Bars below the contour plot indicate the time where data were averaged for further analysis. ....	47
Figure 3-7. Average size distribution for each ozone mixing ratio in experiments with 40, 60 and 80 nm dia. seed particles. Approximate ozone mixing ratios are 30, 80, 140, 200 and 250 ppbv. ....	49
Figure 3-8. Growth experiment using 60 nm ammonium sulfate seed particles. ....	51
Figure 3-9. Growth experiment using 80 nm ammonium sulfate seed particles. ....	52
Figure 3-10. Seed particle growth (increase in median diameter) vs ozone mixing ratio. Squares and circles represent duplicate experiments with error bars representing one standard deviation. The lines represent predicted particle growth using modeling as described in section 2.4 with a molar yield of 12.5% for formation of HOMs from $\alpha$ -pinene ozonolysis. ....	54
Figure 3-11. Molecular composition of particle-phase organics upon exit of the flow tube. ....	57

Figure 3-12. Average NAMS spectra from 60 individual particle hits. 80 nm ammonium sulfate seed particles were exposed to oxidation products formed from 11 ppbv $\alpha$ -pinene and ~250 ppbv ozone in the flow tube reactor.....	58
Figure 4-1. Experimental setup for high relative humidity experiments.....	73
Figure 4-2. Explanation of efflorescence and deliquescence of ammonium sulfate seed particles. ERH denotes the efflorescence relative humidity and DRH denotes the deliquescence relative humidity.....	74
Figure 4-3. Measured change in diameter of a) seeds and b) seeds exposed to ~200 ppbv ozone caused by the removal of diffusion dryer tubes before measurement SMPS allowing for measurement of wet particles.....	76
Figure 4-4. Time series over a typical growth experiment. Green line represents when $\alpha$ -pinene was started with subsequent gray lines representing an increase in ozone concentration. Solid bars at the top represent time period over which data was averaged for analysis. Measured ozone mixing ratio, median diameter and number concentration of the distribution exiting the flow over time are shown. The $\alpha$ -pinene mixing ratio was 11 ppbv.....	77
Figure 4-5. Particle growth of size-selected 40 nm particles after exposure to increasing ozone mixing ratio with constant $\alpha$ -pinene (11 ppbv) under different RH conditions: a) shows dry seed particles at an RH of 10% b) shows dry seed particles at an RH of 60% and c) shows seeds with ALW at an RH of 60%.....	79
Figure 4-6. Particle growth data for a) 40 nm and b) 60 nm dry diameter ammonium sulfate seed particles. Each plot shows the change in median diameter of the (dry) particle size distribution exiting the flow tube as a function of ozone mixing ratio, for the three different RH conditions.....	82
Figure 4-7. Particle growth data for a) 30, b) 50 and c) 80 nm dry ammonium sulfate seed particles.....	83
Figure 4-8. Simplified mechanism describing various pathways for gas-phase product formation from $\alpha$ -pinene ozonolysis. HOM formation occurs by the green route, while water vapor only affects the blue route. This figure is the same as Figure 1-5 and is shown here for the convenience of the reader.....	84

Figure 4-9. Condensation sink values determined by the three methods described in the text for ammonium sulfate seed particles with a dry diameter of 40 nm (purple) and the grown particles after exposure to 11 ppbv  $\alpha$ -pinene and 200 ppbv ozone in the flow tube (green). “Measured 50% RH” represents the lower limit calculation of the condensation sink. “AS” represents the upper limit calculation of the condensation sink. “AS+SOA” represents the best guess calculation of the condensation sink. .... 88

Figure 4-10. Determined percent yield of  $\alpha$ -pinene oxidation products that must contribute to growth to explain the measured change in particle diameter. .... 89

Figure 4-11. Mass spectra of collected particles exiting the flow tube. a) dry conditions (10% RH). b) high relative humidity (60% RH) with ALW. .... 90

## ABSTRACT

Atmospheric aerosols represent the greatest remaining uncertainty in the overall understanding of climate change. Currently climate models do not accurately predict cloud condensation nuclei (CCN) concentrations leading to high uncertainty in the overall cooling effect on global climate by aerosols. Small nanoparticles (10-100 nm in diameter) have also been shown to have negative effects on human health. The growth of particles in this size range is complex and many processes are poorly understood leading to over simplifications in climate models. Growth in this size range is dominated by low volatility organics that are present in the gas phase of the ambient atmosphere. These gas phase molecules are oxidation products of organic precursors that can be emitted from various natural and anthropogenic sources. These precursors are oxidized by species such as ozone, OH and NO<sub>3</sub> to produce a large number of oxidation products with a wide range of chemical properties. The wide range of chemical properties cause particles to grow by several processes including condensation, equilibrium partitioning and particle phase reaction, further increasing complexity. Finally, the simultaneous presence of many precursors and oxidants in the atmosphere even further increases the number of potential oxidation products that can be created.

The work described in this dissertation aims to improve the understanding of particle growth in this size range by simulating different atmospheric conditions in a flow tube reactor and measuring the resulting particle diameter and composition changes. The flow tube reactor used in this work was custom built from a quartz tube

with stainless steel funnels on either end. The reactor was characterized both experimentally and using computational fluid dynamic (CFD) simulations to ensure a known and reproducible residence time of particles, which was approximately four minutes under the conditions used in these experiments. Knowing the reaction time along with the concentrations of reactants allowed for kinetic modeling of oxidation products formed in the flow tube. Growth of size-selected ammonium sulfate seed particles by  $\alpha$ -pinene ozonolysis was studied under dry conditions (RH 10%) at room temperature to determine the amount of condensable material needed to explain the measured growth. Based on the results, a molar yield of highly oxidized molecules (HOMs) of  $13\pm 1\%$  is reported for  $\alpha$ -pinene ozonolysis.

The experimental setup was then modified to allow experiments to be done under high relative humidity and with seed particles containing aerosol liquid water (ALW). The results showed that growth of dry seed particles was independent of relative humidity (RH), providing evidence that formation of condensable molecules in the gas phase is independent of water vapor. However, when aerosol liquid water was present in the particles, a significant growth enhancement was observed, especially at smaller seed particle diameters where seeds were more likely to be homogeneous. The work described here provides valuable insight into the mechanisms by which aerosol particles grow when exposed to  $\alpha$ -pinene oxidation products and will help to increase the understanding of particle growth into CCN size ranges in order to improve predictions made by climate models.

## Chapter 1

### INTRODUCTION

#### 1.1 Current Understanding of Atmospheric Aerosols

Aerosols are defined as solid or liquid particles suspended in a gas and are commonly found within the Earth's atmosphere. These airborne particles are complex in nature due to the wide variety of chemical species that they can contain. The most basic way to classify airborne particles is by their aerodynamic size, which refers to the diameter of a spherical particle with the same settling velocity as the particle of interest<sup>1</sup>. Particles present in the atmosphere are generally placed into three main categories based on their aerodynamic size: ultrafine particles are those with diameters less than 100 nm, fine particles have diameters between 100 nm and 2.5  $\mu\text{m}$  and coarse particles are those with diameters greater than 2.5  $\mu\text{m}$ <sup>2</sup>.

Particles can be traced back to two different source types: primary, where particles are directly emitted into the atmosphere from processes such as combustion and secondary, where particles are formed in the atmosphere from clustering and condensation of gas phase species<sup>3</sup>. Secondary particles originate from a process known as new particle formation (NPF) where low volatility gas-phase molecules collide to form small clusters of only a few molecules and can grow to stable particles when low volatility molecules irreversibly condense. Primary particles are produced across the entire size range, while secondary particles from NPF are in the ultrafine size range.

Ultrafine particles can be subdivided into nucleation mode (<10 nm) and Aitken mode (10-100 nm) size ranges<sup>2</sup>. While these particles contribute very little in terms of mass concentration of ambient particulate matter, they do account for the largest fraction of particles in terms of number concentration<sup>4</sup>. The high number concentration of these particles causes their climate and human health effects to be substantial, especially as they grow to larger sizes. Figure 1-1 illustrates typical size distributions of ambient particles, with nanoparticles showing the greatest number concentrations.

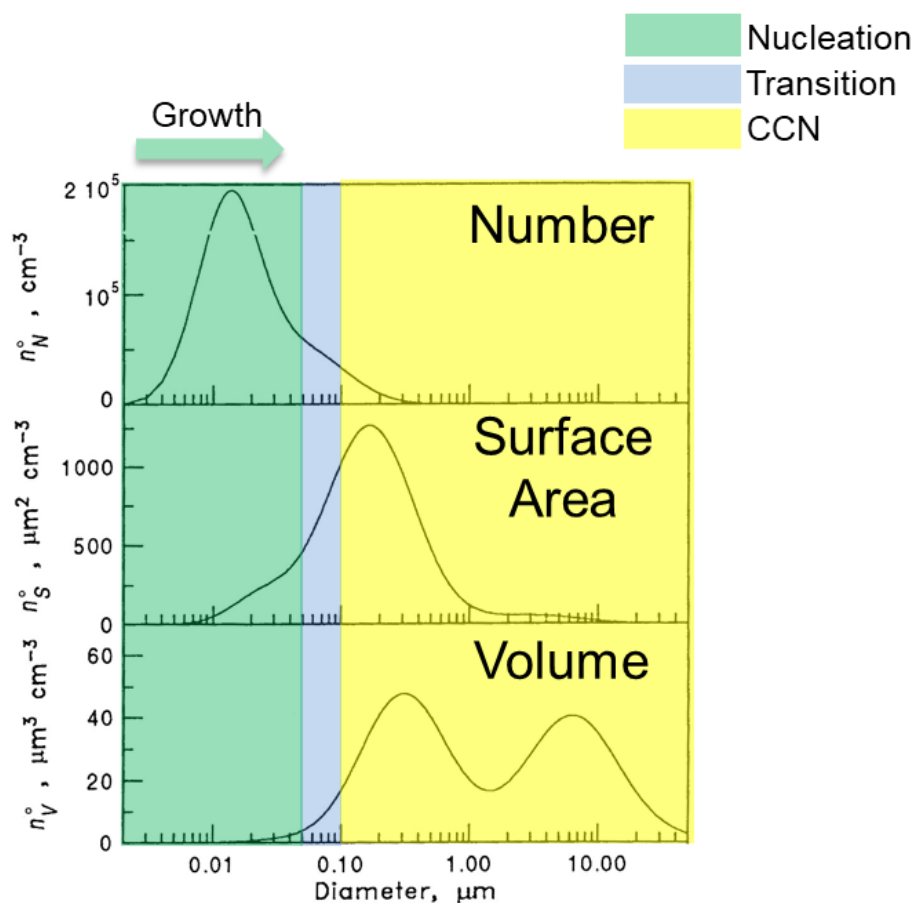


Figure 1-1. Ambient concentrations of particles. Adapted from reference 2.

## **1.2 Environmental Effects of Aerosol**

Aerosol particles have a significant cooling effect on the Earth's atmosphere. This cooling effect has two components. First is the direct effect, where light coming from the sun towards the Earth is reflected off the particles back into space. Second is the indirect effect where particles act as seeds for cloud droplet formation. Particles that are large enough to allow water to irreversibly condense on them are referred to as cloud condensation nuclei (CCN)<sup>2,5</sup>. Both of these effects cool the Earth by causing less sunlight to make it to the planet's surface. Figure 1-2 shows an illustration of these effects. While aerosols are known to produce a cooling effect, the magnitude of this effect is still highly uncertain, making aerosols the largest remaining uncertainty in the overall understanding of climate change<sup>5-7</sup>. Recently, climate models have been shown to underpredict both ambient particle and CCN concentrations<sup>8</sup>. This highlights the need for a better understanding of how particles form and grow in the atmosphere. If climate models do not properly incorporate the complex processes associated with aerosol formation and growth, then they cannot accurately predict the impact of CCN<sup>9,10</sup>. In order to improve predictions of how the climate has changed since the industrial revolution and how climate will continue to change into the future it is necessary to better understand the processes that dictate aerosol formation and growth so that climate models can be improved.

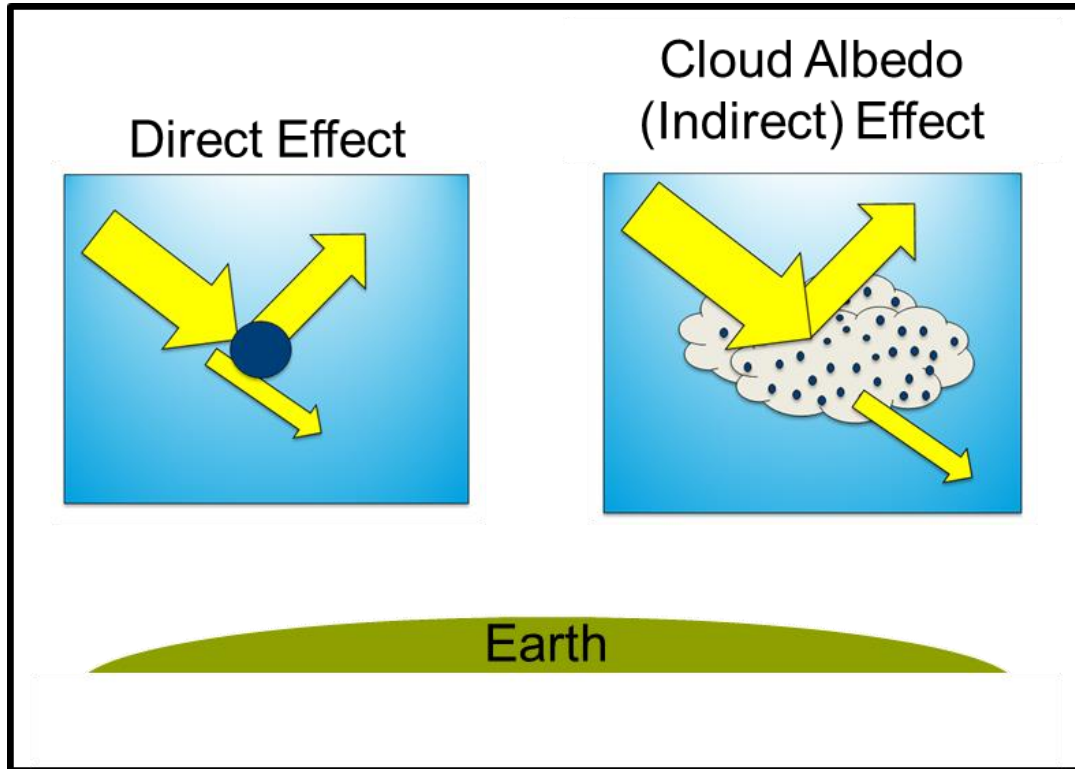


Figure 1-2. An illustration of how particles cool the Earth by reflecting light from the sun.

Under typical atmospheric conditions, newly formed particles must grow to a size of 50-100 nm in diameter in order to be able to serve as CCN<sup>11-13</sup>. In this size range CCN activity is dependent on both particle size and composition. However, once the particle diameter increases above approximately 100 nm, the composition becomes less important and most particles are able to activate as CCN. Therefore, understanding the growth of particles in this size range becomes very important for accurately predicting CCN concentrations. A generalized process describing CCN formation in the atmosphere is shown in Figure 1-3.

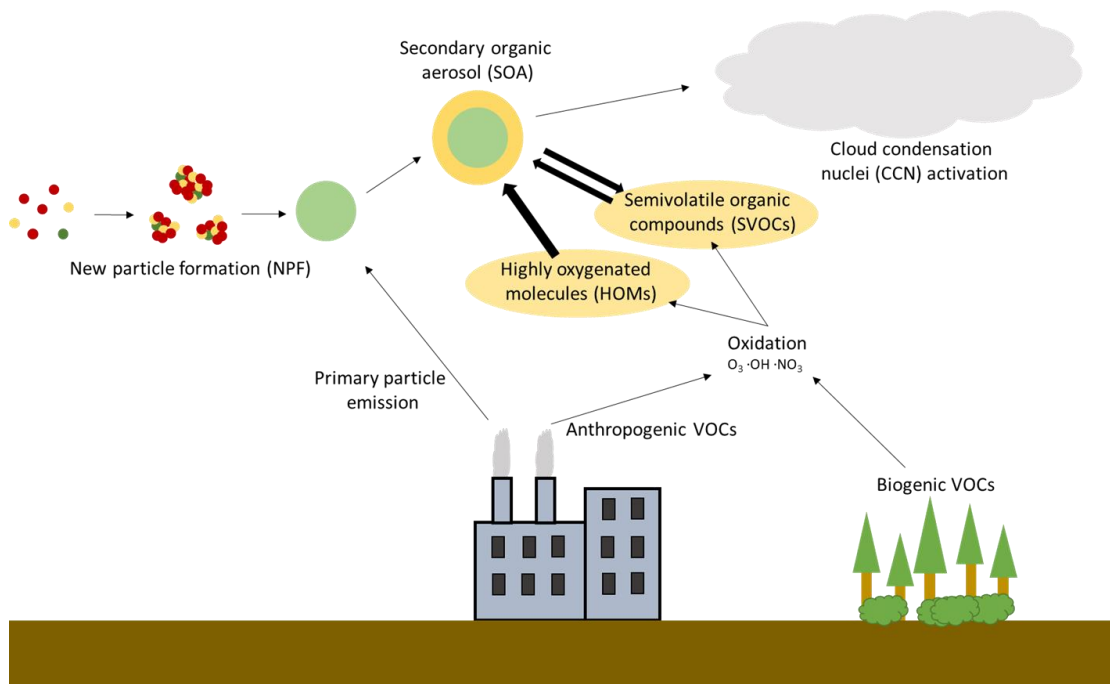


Figure 1-3. Generalized process of CCN formation in the atmosphere by growth of secondary organic aerosol.

### 1.3 Health Effects of Aerosol

Aerosols have also been shown to have negative health effects on humans, as aerosols have been linked to outcomes such as cardiovascular disease and asthma. Ultrafine particles are particularly important as they have been shown to enter the deepest part of the lungs and have the potential to cause the most harm<sup>4</sup>. Therefore, gaining a better understanding of how particles form, grow to larger sizes and the molecules composing the particles can provide insight into how to best minimize any health effects caused by increased exposure to aerosols.

### 1.4 New particle Formation

Ultrafine particles are typically formed through NPF where gas-phase molecules with very low volatility such as sulfuric acid, collide and form small

clusters. Sulfuric acid is commonly found in the atmosphere as it can be formed by photooxidation of  $\text{SO}_2$  by  $\text{OH}^{14,15}$ . Sulfuric acid clusters form and continue to grow by condensation of sulfuric acid. The acidic clusters can be stabilized by basic molecules such as ammonia and some water molecules creating a ternary process of nucleating new particles. However, once the particles grow to a few nanometers in diameter the complexity of the growth processes increases substantially as organic molecules begin to significantly contribute to the growth. This complexity is caused by the wide range of organic molecules produced in the atmosphere, many of which are extremely nonvolatile. An overview of NPF and particle growth in the ambient atmosphere is shown in Figure 1-4.

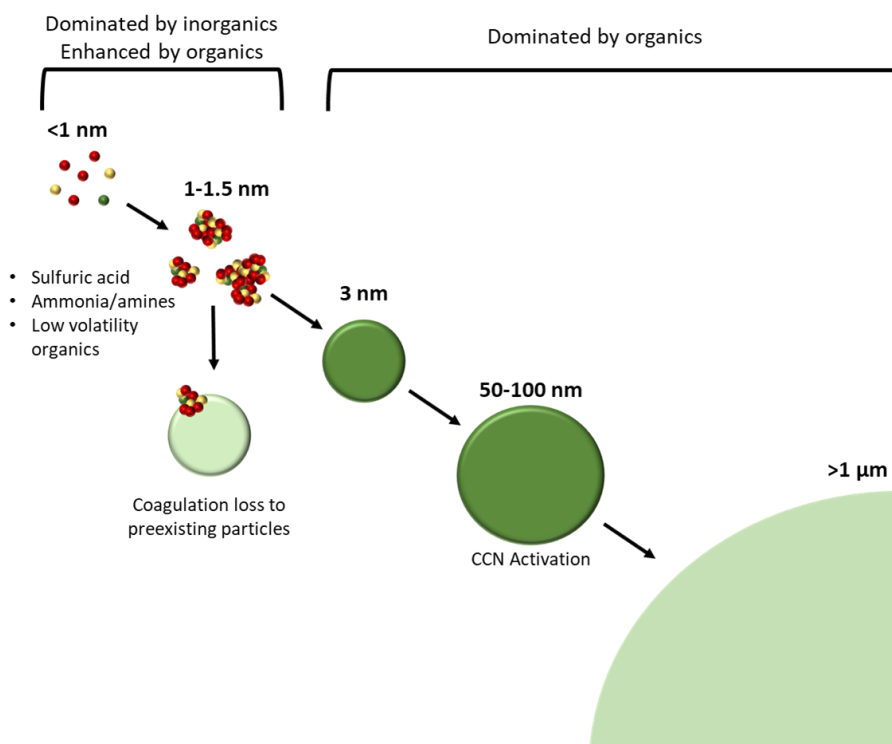


Figure 1-4. Overview of NPF and particle growth into CCN activation. Adapted from reference 14

## 1.5 Particle Growth by Organics

A number of molecules present in the atmosphere are capable of contributing to growth of particles when oxidized. These molecules are known as volatile organic molecules (VOCs) with those naturally emitted into the atmosphere being referred to as biogenic volatile organic compounds (BVOCs)<sup>16,17</sup>. Isoprene is the most commonly emitted BVOC with estimated global emissions to be over 500 TgC per year<sup>18</sup>.

Monoterpenes are another group of commonly emitted BVOCs with emission estimated near 100 TgC per year<sup>19</sup>. Some common BVOCs are shown in Table 1-1. The most common monoterpene is  $\alpha$ -pinene with emissions of 32 TgC per year. Due to the large amount of global emission and large yield of highly oxidized molecules (HOMs) compared to isoprene and other monoterpenes,  $\alpha$ -pinene was chosen as the focus of this work.

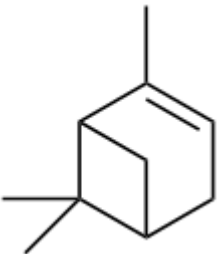
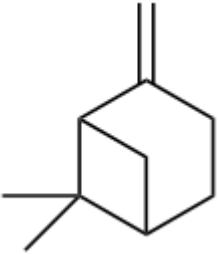
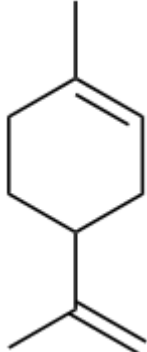
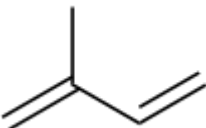
	$\alpha$ -Pinene	$\beta$ -Pinene	Limonene	Isoprene
Structure				
Formula	C <sub>10</sub> H <sub>16</sub>	C <sub>10</sub> H <sub>16</sub>	C <sub>10</sub> H <sub>16</sub>	C <sub>5</sub> H <sub>8</sub>
MW	136.238	136.238	136.238	68.119
HOM yield (%) <sup>a</sup>	3.4	0.12	5.3	0.01

Table 1-1 Common biogenic precursors known to contribute to SOA. <sup>a</sup>HOM Yields taken from reference 20.

Monoterpenes such as  $\alpha$ -pinene can be oxidized in the atmosphere by oxidants such as ozone and OH to produce a large number of products with a wide range of chemical properties<sup>16,18,19</sup>. Ozone is commonly present in the atmosphere with ambient mixing ratios frequently between 30-100 ppbv<sup>20</sup> while OH is frequently found in the pptv range. The higher mixing ratio of ozone in the atmosphere leads to as much as 80% of emitted  $\alpha$ -pinene reacting with ozone. Due to ozonolysis being the primary oxidation fate of  $\alpha$ -pinene, ozone was chosen as the oxidant used throughout this work. A generalized reaction scheme for  $\alpha$ -pinene ozonolysis is shown in Figure 1-5<sup>21-24</sup>. Here the ozone attacks the double bond within  $\alpha$ -pinene to create a primary ozonide. Due to the exothermic nature of this reaction the primary ozonide becomes excited and breaks down to form a carbonyl oxide biradical, which is commonly known as a Criegee intermediate (CI). CIs can form with a number of different molecular structures with the two most common formed during  $\alpha$ -pinene ozonolysis shown in Figure 1-5. These molecules are very reactive due to the biradical and can further react by a number of different pathways. Three main reaction pathways relevant to this work are shown in Figure 1-5. The first pathway involves unimolecular isomerization of the CI followed by repeated addition of O<sub>2</sub>. Products formed from this pathway are classified as HOMs and generally have very low volatility leading to them condensing into the particle phase. Alternately, the CI can undergo collisional stabilization with gas molecules to form a stabilized Criegee intermediate (sCI). sCIs can go on to react with gases such as H<sub>2</sub>O, NO<sub>x</sub>, SO<sub>2</sub> or other oxidation species to produce commonly found oxidation products such as pinic acid and pinonaldehyde. Figure 1-5 only shows a small fraction of potential products

formed from  $\alpha$ -pinene ozonolysis as hundreds of unique products have been observed from this process.

A frequent byproduct of  $\alpha$ -pinene ozonolysis is OH, another potential oxidant of  $\alpha$ -pinene. The OH yield from  $\alpha$ -pinene has been shown to be as high as 80%<sup>19</sup>. In laboratory experiments, this leads to a buildup of OH above what is typically found in the atmosphere and OH can begin to compete with ozone to react with  $\alpha$ -pinene. An additional oxidant further complicates possible reaction pathways and becomes less similar to atmospheric conditions since ozonolysis is much more likely in the ambient environment. Therefore, in experiments described throughout this dissertation a scavenger was added to react with OH and isolate the reaction between ozone and  $\alpha$ -pinene. H<sub>2</sub> was chosen as the OH scavenger in this work for a number of reasons. First, high purity tanks of H<sub>2</sub> gas are readily available and easily introduced into a reaction chamber. Second, H<sub>2</sub> is selectively reactive with OH and does not react with ozone or  $\alpha$ -pinene. Finally, the reaction products from H<sub>2</sub> scavenging OH will have little effect on the overall reaction products as the ultimate product of this process is water. The main product of concern is HO<sub>2</sub> which can react with sCIs as shown in Figure 1-5. However, HO<sub>2</sub> has been shown to exist in the atmosphere at mixing ratios on the order of tens of pptv<sup>25</sup>. Assuming all OH is converted to HO<sub>2</sub> during the experiments described in Chapters 3 and 4; a maximum mixing ratio on the order of hundreds of pptv HO<sub>2</sub> would exist in the reactor. Therefore, mixing ratios are similar to those found in the atmosphere. Additionally, HO<sub>2</sub> would only affect the Syn-sCI pathway shown in Figure 5-1 and would have little effect on the HOM pathway which is the primary focus of this work. For these reasons the effect of OH produced from  $\alpha$ -pinene is assumed to be insignificant in all experiments described in this dissertation.

The hundreds on potential oxidation products from  $\alpha$ -pinene ozonolysis create group of products that have a wide range of chemical properties. To better understand these properties, oxidation products can be sub grouped into classes of molecules that have similar characteristics. Oxidation products with significantly lower volatility than the precursor VOC but still largely remain in the gas phase, only entering the particle by a small amount of equilibrium partitioning are known as semivolatile organic compounds (SVOCs). Molecules with volatilities low enough to irreversibly condense onto the particle would fall into either the low volatility organic compound (LVOC) or extremely low volatility organic compound (ELVOC) groups which are distinguished by the particle size where condensation begins to occur. ELVOC can condensationally grow particles as small as 2 nm in diameter, while LVOC can usually grow particles only larger than about 10 nm in diameter. ELVOC and LVOC molecules that are generally produced by a peroxy radical rearranges to produce an alkyl radical that subsequently reacts with O<sub>2</sub> to produce another peroxy radical in the molecule, and the process repeats until the molecule becomes highly oxidized (HOM)<sup>28-30</sup>. Because the autooxidation process quickly decreases the volatility of the molecule, HOM is frequently used synonymously with ELVOC and will be used throughout this dissertation to describe all molecules that irreversibly condense onto Aitken mode particles.

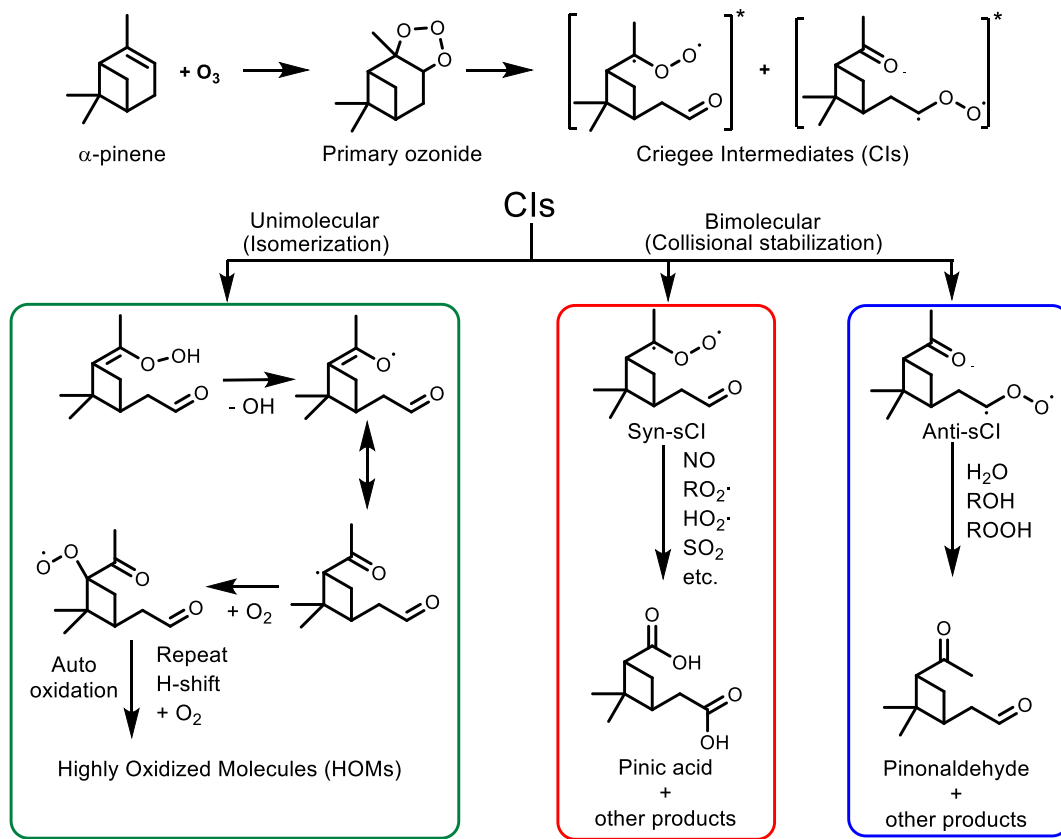


Figure 1-5. Simplified reaction scheme showing various pathways of  $\alpha$ -pinene ozonolysis. Adapted from references 21-24

While partitioning of SVOCs alone results in little growth compared to irreversible condensation, chemistry occurring in the particle phase has been shown as another potential growth mechanism<sup>31-35</sup>. Here SVOCs that have already partitioned into the particle phase react with other species present in the particle such as other SVOCs or HOMs creating additional nonvolatile material. This chemistry acts as a sink for the SVOCs and results in additional partitioning effectively driving more SVOCs into the particle phase. Chapter 4 details experiments investigating particle phase chemistry.

## 1.6 Studying Particle Growth in the Laboratory

The complexity of particle growth through the Aitken mode size range makes studying the growth processes occurring in this size range difficult and has recently become an important area of work. Custom built reactors with known reaction times have been used to simulate various atmospheric conditions and measure particle growth in the laboratory<sup>27,28,36-39</sup>. These studies typically use either chambers or flow tube reactors to study particle growth by oxidizing VOCs and measuring resulting products and particles. Both types of reactors have various pros and cons for analyzing particle growth. For example, chamber reactors have large volumes and long reaction times allowing the mixing ratios of reactants to be low, near atmospheric conditions. However, the long reaction time increases the effects of wall loss as molecules adsorb and desorb onto the walls with additional chemistry potentially occurring on the wall. Additionally, it can be difficult to determine time dependent changes during a chamber experiments as the instrumentation being used must have the time resolution to measure changes. One of these chambers is the Cosmic Leaving Outdoor Droplets (CLOUD) which was designed to measure NPF and the growth of freshly nucleated particles by various organic oxidation products using a variety of instrumentation<sup>37,38</sup>.

Conversely, flow tube reactors have shorter reaction time as there is little recirculation within the reactor. Instead, air moves linearly from the inlet towards the outlet. Reactant mixing ratios must be increased in flow tube reactors in order to simulate atmospheric processes over the shorter reaction times. Additionally, wall loss effects are usually smaller due reaction times being shorter than the time it takes for gasses to diffuse to the outer walls of the reactor. The time dependence of measurements is less important for flow tube reactors as a constant flow that has

experienced the same reaction time is always exiting the reactor. As long as conditions in the reactor are stable, then measurements can take as long as the instrumentation requires.

Ideally, working with reactant mixing ratios at ambient levels is always preferable to ensure reactions occur as they do in the atmosphere. However, the increased mixing ratios used in flow tube reactors are not expected to affect the chemical processes associated with particle growth. As long as the products being formed primarily go through the unimolecular pathway shown in Figure 1-5 increasing reactant concentrations will simply increase the reaction rate and not affect the composition of products. This idea will be confirmed experimentally throughout this work by two measurements. First, ozone mixing ratio will be varied to determine if particle growth shows a linear relationship with increasing reactant concentration. Again, this is expected as long as the reaction proceeds through a unimolecular pathway. Second, molecular composition measurements are done to ensure the organic molecules condensing onto particles are monomers. If dimers are present in the spectra it would suggest a bimolecular pathway and could indicate a deviation from atmospherically relevant reactions. Table 1-2 compares reactant mixing ratios used in experiments throughout this dissertation to those found in the ambient environment. Overall, mixing ratios are similar, especially for ozone, while  $\alpha$ -pinene is elevated above ambient to account for the shorter reaction time.

Component	Ambient mixing ratio	Experimental mixing ratio
ozone	30-100 ppbv	0-300 ppbv
$\alpha$ -pinene	100-600 pptv	11 ppbv

Table 1-2 Comparison of reactant mixing ratios used for flow tube reactor experiments in this dissertation compared to ambient mixing ratios. Ambient mixing ratios taken from reference 20.

## 1.7 Scope of This Dissertation

The work presented in this dissertation details the characterization and use of a flow tube reactor to effectively study particle growth by simulating atmospheric conditions and measuring the corresponding amount of growth. This is done to gain a better understanding of particle growth in the Aitken mode with the goal of improving predictions of CCN concentrations. Improving these predictions will help to lower the uncertainty of aerosol effects within climate models to improve the overall understanding of climate change. The measured particle growth combined with compositional measurements of particles exiting the reactor and kinetic modeling allow for the elucidation of various processes dictating the growth of ultrafine particles in the atmosphere. Chapter 2 discusses experimental methodology used throughout the work. Chapter 3 discusses the characterization of the flow tube reactor and use to study particle growth under dry conditions. Chapter 4 discusses improvements to the system in order to study particle growth at high relative humidity and seed particles containing aerosol liquid water. Finally, chapter 5 summarizes the overall findings of the work and discusses potential future work building upon what is discussed here.

## REFERENCES

- (1) Hinds, W. C. *Aerosol Technol. Prop. Behav. Meas. airborne Part. 2nd ed. New York John Wiley Sons* **1999**, 42–74
- (2) Seinfeld, J. H.; Pandis, S. N. *Atmospheric Chemistry and Physics: From Air Pollution to Climate Change*; Wiley, **2012**.
- (3) Kulmala, M.; Vehkamäki, H.; Petäjä, T.; Dal Maso, M.; Lauri, A.; Kerminen, V. M.; Birmili, W.; McMurry, P. H. *J. Aerosol Sci.* **2004**, *35* (2), 143–176.
- (4) Slezakova, K.; Morais, S.; do Carmo Pereira, M. Atmospheric Nanoparticles and Their Impacts on Public Health. *In Current Topics in Public Health; InTech*, **2013**.
- (5) Seinfeld, J. H.; Bretherton, C.; Carslaw, K. S.; Coe, H.; DeMott, P. J.; Dunlea, E. J.; Feingold, G.; Ghan, S.; Guenther, A. B.; Kahn, R.; Kraucunas, I.; Kreidenweis, S. M.; Molina, M. J.; Nenes, A.; Penner, J. E.; Prather, K. A.; Ramanathan, V.; Ramaswamy, V.; Rasch, P. J.; Ravishankara, A. R.; Rosenfeld, D.; Stephens, G.; Wood, R. *Proc. Natl. Acad. Sci. U. S. A.* **2016**, *113* (21), 5781–5790.
- (6) Stevens, B.; Feingold, G. *Nature* **2009**, *461* (7264), 607–613.
- (7) Meehl, G. A.; Stocker, T. F.; Collins, W. D.; Friedlingstein, P.; Gaye, T.; Gregory, J. M.; Kitoh, A.; Knutti, R.; Murphy, J. M.; Noda, A. **2007**.
- (8) Fanourgakis, G. S.; Kanakidou, M.; Nenes, A.; Bauer, S. E.; Bergman, T.; Carslaw, K. S.; Grini, A.; Hamilton, D. S.; Johnson, J. S.; Karydis, V. A.; Kirkevåg, A.; Kodros, J. K.; Lohmann, U.; Luo, G.; Makkonen, R.; Matsui, H.; Neubauer, D.; Pierce, J. R.; Schmale, J.; Stier, P.; Tsigaridis, K.; Van Noije, T.; Wang, H.; Watson-Parris, D.; Westervelt, D. M.; Yang, Y.; Yoshioka, M.; Daskalakis, N.; Decesari, S.; Gysel-Beer, M.; Kalivitis, N.; Liu, X.; Mahowald, N. M.; Myriokefalitakis, S.; Schrödner, R.; Sfakianaki, M.; Tsimpidi, A. P.; Wu, M.; Yu, F. *Atmos. Chem. Phys.* **2019**, *19* (13), 8591–8617

- (9) Liu, X.; Easter, R. C.; Ghan, S. J.; Zaveri, R.; Rasch, P.; Shi, X.; Lamarque, J. F.; Gettelman, A.; Morrison, H.; Vitt, F.; Conley, A.; Park, S.; Neale, R.; Hannay, C.; Ekman, A. M. L.; Hess, P.; Mahowald, N.; Collins, W.; Iacono, M. J.; Bretherton, C. S.; Flanner, M. G.; Mitchell, D. *Geosci. Model Dev.* **2012**, *5* (3), 709–739.
- (10) Tsigaridis, K.; Daskalakis, N.; Kanakidou, M.; Adams, P. J.; Artaxo, P.; Bahadur, R.; Balkanski, Y.; Bauer, S. E.; Bellouin, N.; Benedetti, A.; Bergman, T.; Berntsen, T. K.; Beukes, J. P.; Bian, H.; Carslaw, K. S.; Chin, M.; Curci, G.; Diehl, T.; Easter, R. C.; Ghan, S. J.; Gong, S. L.; Hodzic, A.; Hoyle, C. R.; Iversen, T.; Jathar, S.; Jimenez, J. L.; Kaiser, J. W.; Kirkevåg, A.; Koch, D.; Kokkola, H.; H Lee, Y.; Lin, G.; Liu, X.; Luo, G.; Ma, X.; Mann, G. W.; Mihalopoulos, N.; Morcrette, J. J.; Müller, J. F.; Myhre, G.; Myriokefalitakis, S.; Ng, N. L.; O’donnell, D.; Penner, J. E.; Pozzoli, L.; Pringle, K. J.; Russell, L. M.; Schulz, M.; Sciare, J.; Seland; Shindell, D. T.; Sillman, S.; Skeie, R. B.; Spracklen, D.; Stavrou, T.; Steenrod, S. D.; Takemura, T.; Tiitta, P.; Tilmes, S.; Tost, H.; Van Noije, T.; Van Zyl, P. G.; Von Salzen, K.; Yu, F.; Wang, Z.; Wang, Z.; Zaveri, R. A.; Zhang, H.; Zhang, K.; Zhang, Q.; Zhang, X. *Atmos. Chem. Phys.* **2014**, *14* (19), 10845–10895.
- (11) McFiggans, G.; Artaxo, P.; Baltensperger, U.; Coe, H.; Facchini, M. C.; Feingold, G.; Fuzzi, S.; Gysel, M.; Laaksonen, A.; Lohmann, U.; Mentel, T. F.; Murphy, D. M.; O’Dowd, C. D.; Snider, J. R.; Weingartner, E. *Atmos. Chem. Phys.* **2006**, *6* (9), 2593–2649.
- (12) Wang, J.; Lee, Y. N.; Daum, P. H.; Jayne, J.; Alexander, M. L. *Atmos. Chem. Phys.* **2008**, *8* (21), 6325–6339.
- (13) Kammermann, L.; Gysel, M.; Weingartner, E.; Herich, H.; Cziczo, D. J.; Holst, T.; Svenningsson, B.; Arneth, A.; Baltensperger, U. *J. Geophys. Res. Atmos.* **2010**, *115* (D4).
- (14) Zhang, R.; Khalizov, A.; Wang, L.; Hu, M.; Xu, W. *Chem. Rev.* **2012**, *112* (3), 1957–2011.
- (15) Shrivastava, M.; Lou, S.; Zelenyuk, A.; Easter, R. C.; Corley, R. A.; Thrall, B. D.; Rasch, P. J.; Fast, J. D.; Massey Simonich, S. L.; Shen, H.; Tao, S. *Proc. Natl. Acad. Sci.* **2017**, *114* (6), 1246 LP-1251.
- (16) Robinson, A. L.; Donahue, N. M.; Shrivastava, M. K.; Weitkamp, E. A.; Sage, A. M.; Grieshop, A. P.; Lane, T. E.; Pierce, J. R.; Pandis, S. N. *Science* **2007**, *315* (5816), 1259–1262.

- (17) Donahue, N. M.; Henry, K. M.; Mentel, T. F.; Kiendler-Scharr, A.; Spindler, C.; Bohn, B.; Brauers, T.; Dorn, H. P.; Fuchs, H.; Tillmann, R.; Wahner, A.; Saathoff, H.; Naumann, K. H.; Möhler, O.; Leisner, T.; Müller, L.; Reinnig, M. C.; Hoffmann, T.; Salo, K.; Hallquist, M.; Frosch, M.; Bilde, M.; Tritscher, T.; Barmet, P.; Praplan, A. P.; DeCarlo, P. F.; Dommen, J.; Prévôt, A. S. H.; Baltensperger, U. *Proc. Natl. Acad. Sci. U. S. A.* **2012**, *109* (34), 13503–13508.
- (18) Guenther, A.; Hewitt, C. N.; Erickson, D.; Fall, R.; Geron, C.; Graedel, T.; Harley, P.; Klinger, L.; Lerdau, M.; McKay, W. A.; Pierce, T.; Scholes, B.; Steinbrecher, R.; Tallamraju, R.; Taylor, J.; Zimmerman, P. *J. Geophys. Res.* **1995**, *100* (D5), 8873. <https://doi.org/10.1029/94JD02950>.
- (19) Sindelarova, K.; Granier, C.; Bouarar, I.; Guenther, A.; Tilmes, S.; Stavrakou, T.; Müller, J.-F.; Kuhn, U.; Stefani, P.; Knorr, W. *Atmos. Chem. Phys.* **2014**, *14* (17), 9317–9341.
- (20) Finlayson-Pitts, B. J.; Pitts Jr, J. N. *Chemistry of the Upper and Lower Atmosphere: Theory, Experiments, and Applications*; Elsevier, **1999**.
- (21) Camredon, M.; Hamilton, J. F.; Alam, M. S.; Wyche, K. P.; Carr, T.; White, I. R.; Monks, P. S.; Rickard, A. R.; Bloss, W. *J. Atmos. Chem. Phys.* **2010**, *10* (6), 2893–2917.
- (22) Kahnt, A.; Vermeylen, R.; Iinuma, Y.; Safi Shalamzari, M.; Maenhaut, W.; Claeys, M. *Atmos. Chem. Phys.* **2018**, *18* (11), 8453–8467.
- (23) Newland, M. J.; Rickard, A. R.; Sherwen, T.; Evans, M. J.; Vereecken, L.; Muñoz, A.; Ródenas, M.; Bloss, W. *J. Atmos. Chem. Phys.* **2018**, *18* (8), 6095–6120.
- (24) Li, X.; Chee, S.; Hao, J.; Abbatt, J. P. D.; Jiang, J.; Smith, J. N. *Atmos. Chem. Phys.* **2019**, *19* (3), 1555–1570.
- (25) Holland, F.; Hofzumahaus, A.; Schäfer, J.; Kraus, A.; Pätz, H. W. *J. Geophys. Res. D Atmos.* **2003**, *108* (4), 2–1.

- (26) Jimenez, J. L.; Canagaratna, M. R.; Donahue, N. M.; Prevot, A. S. H.; Zhang, Q.; Kroll, J. H.; DeCarlo, P. F.; Allan, J. D.; Coe, H.; Ng, N. L.; Aiken, A. C.; Docherty, K. S.; Ulbrich, I. M.; Grieshop, A. P.; Robinson, A. L.; Duplissy, J.; Smith, J. D.; Wilson, K. R.; Lanz, V. A.; Hueglin, C.; Sun, Y. L.; Tian, J.; Laaksonen, A.; Raatikainen, T.; Rautiainen, J.; Vaattovaara, P.; Ehn, M.; Kulmala, M.; Tomlinson, J. M.; Collins, D. R.; Cubison, M. J.; Dunlea, E. J.; Huffman, J. A.; Onasch, T. B.; Alfarra, M. R.; Williams, P. I.; Bower, K.; Kondo, Y.; Schneider, J.; Drewnick, F.; Borrmann, S.; Weimer, S.; Demerjian, K.; Salcedo, D.; Cottrell, L.; Griffin, R.; Takami, A.; Miyoshi, T.; Hatakeyama, S.; Shimojo, A.; Sun, J. Y.; Zhang, Y. M.; Dzepina, K.; Kimmel, J. R.; Sueper, D.; Jayne, J. T.; Herndon, S. C.; Trimborn, A. M.; Williams, L. R.; Wood, E. C.; Middlebrook, A. M.; Kolb, C. E.; Baltensperger, U.; Worsnop, D. R. *Science* **2009**, *326* (5959), 1525–1529.
- (27) Pöschl, U.; Martin, S. T.; Sinha, B.; Chen, Q.; Gunthe, S. S.; Huffman, J. A.; Borrmann, S.; Farmer, D. K.; Garland, R. M.; Helas, G.; Jimenez, J. L.; King, S. M.; Manzi, A.; Mikhailov, E.; Pauliquevis, T.; Petters, M. D.; Prenni, A. J.; Roldin, P.; Rose, D.; Schneider, J.; Su, H.; Zorn, S. R.; Artaxo, P.; Andreae, M. O. *Science* **2010**, *329* (5998), 1513–1516.
- (28) Jokinen, T.; Berndt, T.; Makkonen, R.; Kerminen, V. M.; Junninen, H.; Paasonen, P.; Stratmann, F.; Herrmann, H.; Guenther, A. B.; Worsnop, D. R.; Kulmala, M.; Ehn, M.; Sipilä, M. *Proc. Natl. Acad. Sci.* **2015**, *112* (23), 7123–7128.
- (29) Ehn, M.; Thornton, J. A.; Kleist, E.; Sipilä, M.; Junninen, H.; Pullinen, I.; Springer, M.; Rubach, F.; Tillmann, R.; Lee, B.; Lopez-Hilfiker, F.; Andres, S.; Acir, I. H.; Rissanen, M.; Jokinen, T.; Schobesberger, S.; Kangasluoma, J.; Kontkanen, J.; Nieminen, T.; Kurtén, T.; Nielsen, L. B.; Jørgensen, S.; Kjaergaard, H. G.; Canagaratna, M.; Maso, M. D.; Berndt, T.; Petäjä, T.; Wahner, A.; Kerminen, V. M.; Kulmala, M.; Worsnop, D. R.; Wildt, J.; Mentel, T. F. *Nature* **2014**, *506* (7489), 476–479.
- (30) Rissanen, M. P.; Kurtén, T.; Sipilä, M.; Thornton, J. A.; Kangasluoma, J.; Sarnela, N.; Junninen, H.; Jørgensen, S.; Schallhart, S.; Kajos, M. K.; Taipale, R.; Springer, M.; Mentel, T. F.; Ruuskanen, T.; Petäjä, T.; Worsnop, D. R.; Kjaergaard, H. G.; Ehn, M. *J. Am. Chem. Soc.* **2014**, *136* (44), 15596–15606.
- (31) Crouse, J. D.; Nielsen, L. B.; Jørgensen, S.; Kjaergaard, H. G.; Wennberg, P. *O. J. Phys. Chem. Lett.* **2013**, *4* (20), 3513–3520.
- (32) Apsokardu, M. J.; Johnston, M. V. *Atmos. Chem. Phys.* **2018**, *18*, 1895–1907.

- (33) Surratt, J. D.; Murphy, S. M.; Kroll, J. H.; Ng, N. L.; Hildebrandt, L.; Sorooshian, A.; Szmigielski, R.; Vermeylen, R.; Maenhaut, W.; Claeys, M.; Flagan, R. C.; Seinfeld, J. H. *J. Phys. Chem. A* **2006**, *110* (31), 9665–9690.
- (34) Szmigielski, R.; Surratt, J. D.; Vermeylen, R.; Szmigielska, K.; Kroll, J. H.; Ng, N. L.; Murphy, S. M.; Sorooshian, A.; Seinfeld, J. H.; Claeys, M. *J. Mass Spectrom.* **2007**, *42* (1), 101–116.
- (35) Lin, Y. H.; Zhang, H.; Pye, H. O. T.; Zhang, Z.; Marth, W. J.; Park, S.; Arashiro, M.; Cui, T.; Budisulistiorini, S. H.; Sexton, K. G.; Vizuete, W.; Xie, Y.; Luecken, D. J.; Piletic, I. R.; Edney, E. O.; Bartolotti, L. J.; Gold, A.; Surratt, J. D. *Proc. Natl. Acad. Sci. U. S. A.* **2013**, *110* (17), 6718–6723.
- (36) D'Ambro, E. L.; Lee, B. H.; Liu, J.; Shilling, J. E.; Gaston, C. J.; Lopez-Hilfiker, F. D.; Schobesberger, S.; Zaveri, R. A.; Mohr, C.; Lutz, A.; Zhang, Z.; Gold, A.; Surratt, J. D.; Rivera-Rios, J. C.; Keutsch, F. N.; Thornton, J. A. *Atmos. Chem. Phys.* **2017**, *17* (1), 159–174.
- (37) Kirkby, J.; Duplissy, J.; Sengupta, K.; Frege, C.; Gordon, H.; Williamson, C.; Heinritzi, M.; Simon, M.; Yan, C.; Almeida, J.; Trostl, J.; Nieminen, T.; Ortega, I. K.; Wagner, R.; Adamov, A.; Amorim, A.; Bernhammer, A. K.; Bianchi, F.; Breitenlechner, M.; Brilke, S.; Chen, X.; Craven, J.; Dias, A.; Ehrhart, S.; Flagan, R. C.; Franchin, A.; Fuchs, C.; Guida, R.; Hakala, J.; Hoyle, C. R.; Jokinen, T.; Junninen, H.; Kangasluoma, J.; Kim, J.; Krapf, M.; Kurten, A.; Laaksonen, A.; Lehtipalo, K.; Makhmutov, V.; Mathot, S.; Molteni, U.; Onnela, A.; Perakyla, O.; Piel, F.; Petaja, T.; Praplan, A. P.; Pringle, K.; Rap, A.; Richards, N. A. D.; Riipinen, I.; Rissanen, M. P.; Rondo, L.; Sarnela, N.; Schobesberger, S.; Scott, C. E.; Seinfeld, J. H.; Sipila, M.; Steiner, G.; Stozhkov, Y.; Stratmann, F.; Tomé, A.; Virtanen, A.; Vogel, A. L.; Wagner, A. C.; Wagner, P. E.; Weingartner, E.; Wimmer, D.; Winkler, P. M.; Ye, P.; Zhang, X.; Hansel, A.; Dommen, J.; Donahue, N. M.; Worsnop, D. R.; Baltensperger, U.; Kulmala, M.; Carslaw, K. S.; Curtius, J. *Nature* **2016**, *533* (7604), 521–526.
- (38) Sarnela, N.; Jokinen, T.; Duplissy, J.; Yan, C.; Nieminen, T.; Ehn, M.; Schobesberger, S.; Heinritzi, M.; Ehrhart, S.; Lehtipalo, K.; Tröstl, J.; Simon, M.; Kürten, A.; Leiminger, M.; Lawler, M. J.; Rissanen, M. P.; Bianchi, F.; Praplan, A. P.; Hakala, J.; Amorim, A.; Gonin, M.; Hansel, A.; Kirkby, J.; Dommen, J.; Curtius, J.; Smith, J. N.; Petäjä, T.; Worsnop, D. R.; Kulmala, M.; Donahue, N. M.; Sipilä, M. *Atmos. Chem. Phys.* **2018**, *18* (4), 2363–2380.
- (39) Huang, Y.; Coggon, M. M.; Zhao, R.; Lignell, H.; Bauer, M. U.; Flagan, R. C.; Seinfeld, J. H. *Atmos. Meas. Tech.* **2017**, *10* (3), 839–867.

## Chapter 2

### EXPERIMENTAL METHODOLOGY

A variety of instrumentation was utilized for the work presented in this thesis. This chapter outlines the instrumentation and methodology associated with measuring and understanding particle growth.

#### 2.1 Scanning Mobility Particle Sizer

A major factor in characterizing aerosols and studying growth is being able to reliably measure the particle size distribution. This was done using a scanning mobility particle sizer (SMPS)<sup>1</sup>. The instrument used in our lab was specifically designed to measure size distributions in the ultrafine size range.

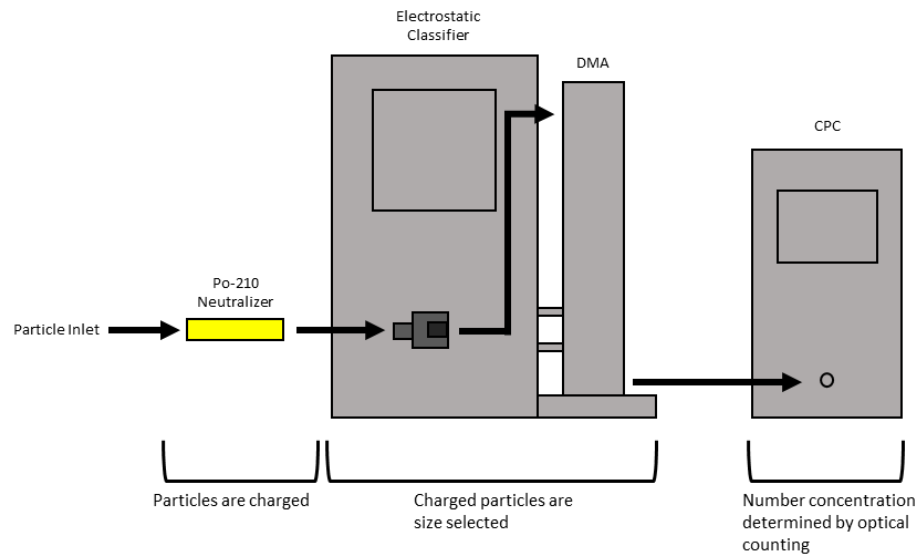


Figure 2-1. Schematic of the scanning mobility particle sizer (SMPS).

The SMPS is made up of two independent instruments, the differential mobility analyzer (DMA) and condensation particle counter (CPC). To measure size distributions particles are first charged by passing them through a Po-210 neutralizer in order to establish a known charge distribution of particles. The polydispersed aerosol flow then enters the DMA where it is exposed to a negatively charged rod in the center of the DMA chamber. Particles enter on the outside at the top of the DMA and are continuously pushed down by the flow. Positively charged particles are attracted to the negatively charged rod. This causes particles to move towards the center with the velocity related to the mobility of the particles causing them to separate based on size. A small slit at the bottom of the DMA chamber causes only a monodispersed distribution of particles to exit the DMA with the size related to the magnitude of the charge applied to the rod. A schematic of the DMA is shown in Figure 2-2 demonstrating the size selection process. These size selected particles then exit the DMA and are transferred into the CPC. Once inside the CPC, particles are exposed to a region that is supersaturated with water vapor. This causes condensation of water onto the particles increasing their diameter so they can be optically detected at the end of the CPC. The combination of a DMA and CPC effectively determines the number concentration of particles with a single mobility diameter. By changing the voltage applied to the rod of the DMA scanning through the measured range of mobility diameter and subsequently measuring the number concentration with the CPC, a full size distribution of particles can be measured. Additionally, as will be discussed in more detail later, the DMA and CPC do not always need to be paired together to work as an SMPS. Depending on the experimental set up it may be beneficial to only use the DMA in order to size select a monodispersed distribution of

particles from a polydispersed distribution. There also may be situations where an entire size distribution is not needed, and a CPC can be used independently to measure the total number concentration of particles present.

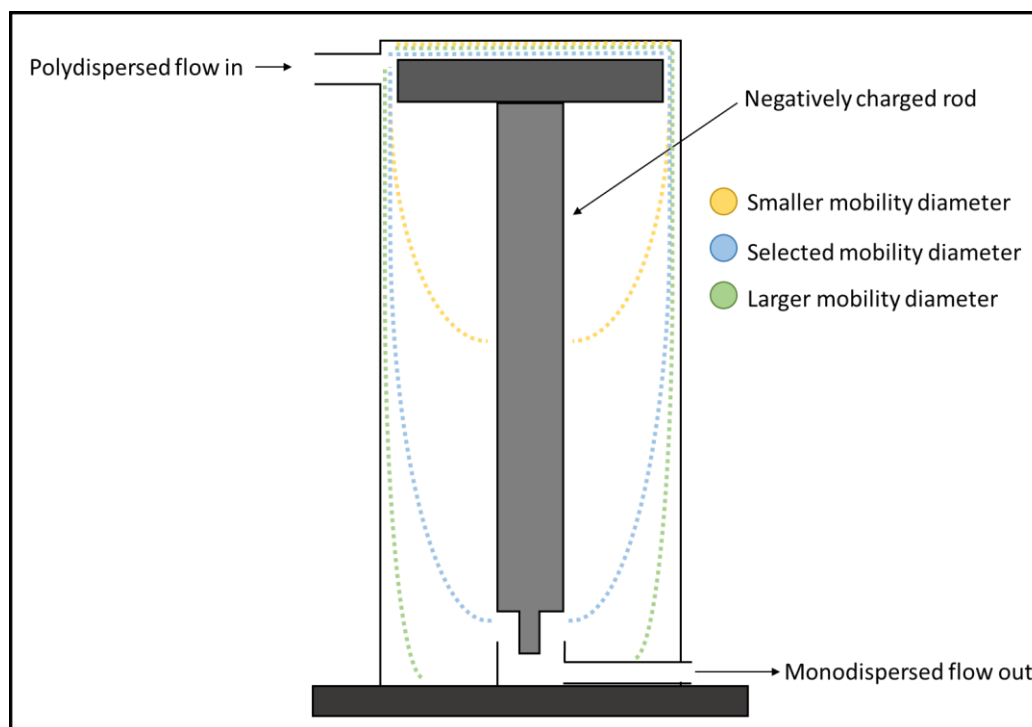


Figure 2-2. Schematic of a differential mobility analyzer (DMA) demonstrating how positively charged particles are size selected based on mobility diameter.

## 2.2 Flow Tube Reactor

This work utilizes a custom built flow tube reactor shown in Figure 2-3 as a way to simulate atmospheric conditions, expose seed particles to those conditions over a known residence time, and measure the resulting growth of the seed particles. The flow tube is composed primarily of a quartz tube 152 cm in length and 20 cm in diameter. Stainless steel funnels are pressed onto either end to decrease the diameter

to 1.3 cm resulting in a total volume of 52.4 L. A large effort was put into ensuring a predictable and reproducible residence time and this process will be further discussed in later chapters; ultimately, a total flow of 6.1 L/min was found to have the best results and produced a residence time of approximately four minutes. The flow tube reactor is operated by introducing a monodispersed aerosol by size selecting using a DMA, and exposing the particles to known concentrations of the organic precursor ( $\alpha$ -pinene) and the oxidant (ozone). The subsequent change in particle size is determined by measuring particles exiting the reactor with the SMPS and comparing to the initial distribution before exposure. Figure 2-3 shows a cartoon exemplifying seed particles growing as they pass through the reactor.

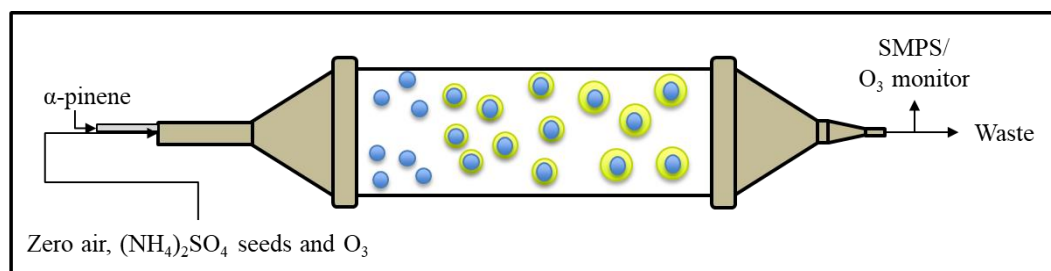


Figure 2-3. Cartoon showing the general layout of the flow tube reactor and how particles grow as they pass through the tube. Blue circles represent size selected ammonium sulfate and the green represents organics condensing onto the particle phase growing the seeds.

Operating the reactor this way is interesting in that it creates a tandem DMA system as the first is used to size select a polydispersed aerosol into a monodispersed distribution centered on a desired particle size while the second DMA is used for measuring the size distribution exiting the reactor. It is therefore extremely important

to understand the way particles are charged throughout the system since the DMA and analysis software rely heavily on known charge state distributions of particles.

Charging of particles can be done two different ways as shown in Figure 2-4. First, particles are charged before the size selection DMA in order to establish a normal distribution centered around a neutral charge. The DMA then size selects positively charged particles at the desired mobility diameter. Since only charged particles are size selected, all seed particles entering the flow tube are positively charged. Due to the normal charge distribution created by the neutralizer a majority of particles are +1 in charge; however, some seeds are +2 and must have a larger physical diameter to have the same mobility diameter. Once the charged particles exit the flow tube for detection by SMPS, the particles can either go through a second neutralizer to reestablish a normal charge distribution or the already charged particles can be detected without passing through the second neutralizer. There are benefits for both analysis setups. For example, bypassing the second neutralizer means only seed particles exiting the flow tube are charged and will be detected, making it easier to see changes in seed diameter if nucleation of new particles is also occurring within the reactor. However, because all particles are charged instead of only a small fraction as assumed by the SMPS software, this method does not give accurate number concentrations. Therefore, unless otherwise noted a second neutralizer was used before measurements. This configuration was useful in that it gave a more accurate number concentration and allowed for the detection of any particles nucleating in the reactor during experiments. As will be discussed later, an accurate number concentration was important for the kinetic modeling of the system as it is a large factor in calculating the condensation sink of particles during an experiment. It was

also helpful to see any nucleation that was occurring as that would also contribute to the condensation sink. However, nucleation was avoided as much as possible as the primary interest in the experiments discussed in this dissertation was the growth of seed particles; any nucleation acts as another sink for gas-phase molecules further complicating the growth occurring within the system.

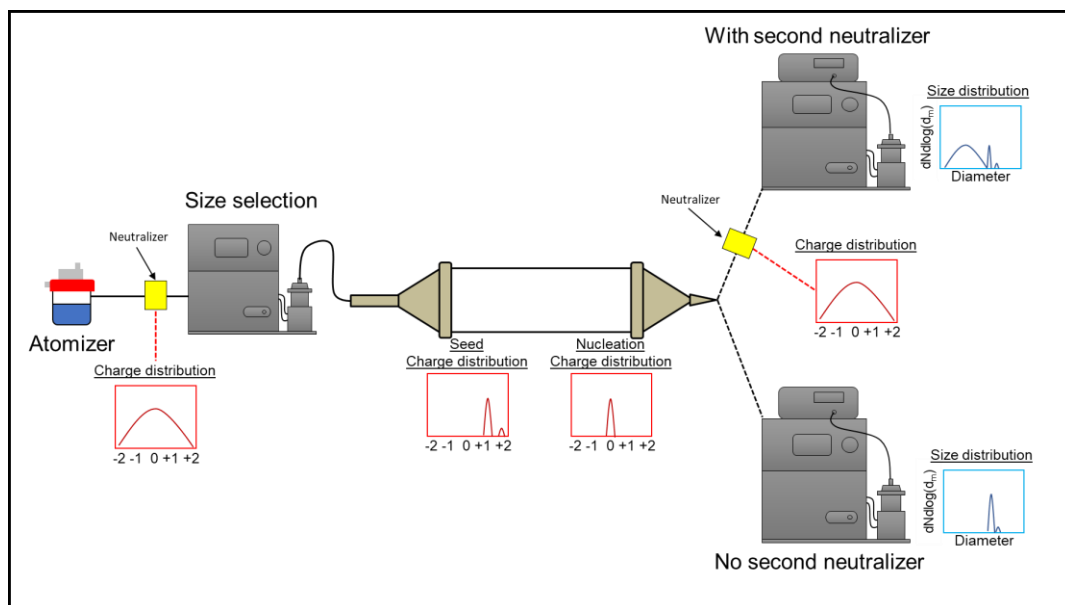


Figure 2-4. Cartoon of particle charge states distribution and the effect of a second radioactive neutralizer before the measurement SMPS on the measured particle size distribution.

### 2.3 Condensation Growth Chamber

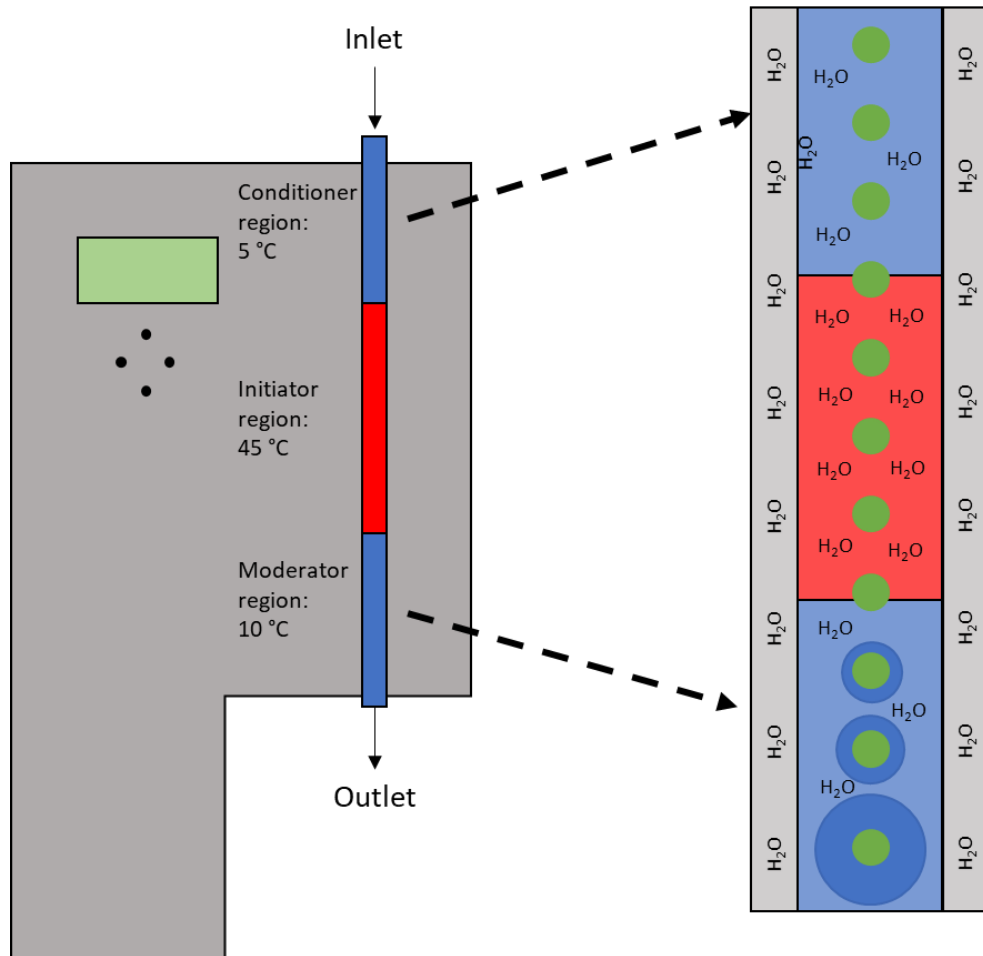


Figure 2-5. Schematic of the condensation growth chamber (CGC) and demonstrating how the three different temperature regions create a supersaturation of water vapor causing condensation onto particles.

As will be discussed in chapter 4, experiments using the flow tube reactor were done to better understand particle growth under different relative humidity conditions. This work required some additions to the experimental setup. First, a water bubbler was added to the make up flow with a needle valve bypass allowing for fine

adjustment of the relative humidity within the reactor. Second, the condensation growth chamber (CGC) was added after the seed particles are size selected<sup>2</sup>. The CGC is used to add water onto the dry seed particles and study the effects of aerosol liquid water. Overall the CGC operates similarly to a CPC as the particles are exposed to a supersaturated concentration of water vapor to promote condensation of water onto the seed particles. This is done by passing the particles through three different regions. First, the particles are cooled in a cold conditioner region held at 5 °C. They are then sent into a warm initiator region held at 45 °C, promoting evaporation of water vapor from the saturated wick that surrounds the growth chamber into the gas-phase. Finally, the particles move into the cool moderator region at 20 °C. This causes the gas-phase to be supersaturated with water vapor resulting in condensation onto the particles as they exit the instrument and creating the wet particles that can then be sent into the flow tube reactor to be studied. A schematic of the CGC is shown in Figure 2-5.

#### **2.4 Composition Measurements**

This work used two methods to analyze the composition of aerosol particles exiting the flow tube. Both methods utilize mass spectrometry but give different information about the particles. First, the nanoaerosol mass spectrometer (NAMS) is a custom-built instrument that is capable of analyzing single particles in the size range of 40-100 nm and gives quantitative elemental information of the aerosol<sup>3</sup>. Second, a Q-Exactive Orbitrap high resolution electrospray ionization mass spectrometer (HR-ESI-MS) was used to measure the molecular composition of collected particles.

NAMS in the configuration used in this work has been described previously<sup>3</sup>. Briefly, aerosol flows through a transfer line from the reactor exit to the NAMS inlet.

Aerosol flow is determined by a flow limiting orifice at the inlet. After passing through the orifice, particles flow through a series of aerodynamic lenses designed to focus them into a narrow beam that enters the ion source region through a series of differentially pumped regions. A high powered Nd:YAG laser is fired into the source region perpendicular to the aerosol beam. The laser is focused into the center of the source region where it crosses the particle beam. If a particle is in the same location as the focused laser spot when the laser fires, it will be ionized by laser induced plasma ionization (LIPI) breaking down the particle into positively charged atomic ions. The ions are then extracted into a time of flight (TOF) mass analyzer where the elemental ions are detected. The measurements made using NAMS give quantitative elemental information for particles. The information from NAMS can be used to elucidate mole fractions of organic and inorganic materials within the particle and calculate O/C ratios for the organic material, this process is explained in Table 2-1.

Elemental Mole Fraction	Apportioned as (NH <sub>4</sub> ) <sub>2</sub> SO <sub>4</sub>	Apportioned as carbonaceous matter
C	-	C
O	4*S	O-4S
N	2*S	N-2*S
S	S	-

Table 2-1 explanation of mole fraction apportionment for NAMS data.

Molecular composition measurements were done offline using a Q-Exactive Orbitrap high resolution electrospray mass spectrometry (HR-ESI-MS)<sup>4,5</sup>. Particles exiting the flow tube reactor were collected on a quartz microfiber filter until approximately 5 µg of material was collected. The organic material present on the

filter was then extracted by sonicating the filter in acetonitrile. The resulting extract was then concentrated using vacuum evaporation to a final concentration of 0.1  $\mu\text{g}/\mu\text{L}$ . This final solution was then analyzed using HR-ESI-MS. Unlike analysis using NAMS, electrospray ionization in conjunction with high resolution analysis with the Orbitrap is capable of providing molecular information of the organic fraction of the aerosol. While the analysis done by the Orbitrap is not quantitative, it can be very useful to determine the characteristics of molecules that are condensing onto the seed particles.

## REFERENCES

- (1) Ham, S.; Lee, N.; Eom, I.; Lee, B.; Tsai, P. J.; Lee, K.; Yoon, C. *Saf. Health Work* **2016**, 7 (4), 381–388.
- (2) Horan, A. J.; Apsokardu, M. J.; Johnston, M. V. *Anal. Chem.* **2017**, 89 (2), 1059–1062.
- (3) Horan, A. J.; Krasnomowitz, J. M.; Johnston, M. V. *Aerosol Sci. Technol.* **2017**, 51 (December), 1135–1143.
- (4) Tu, P.; Hall, W. A.; Johnston, M. V. *Anal. Chem.* **2016**, 88 (8), 4495–4501.
- (5) Tu, P.; Johnston, M. V. *Atmos. Chem. Phys.* **2017**, 17 (12), 7593–7603.

## Chapter 3

### **GROWTH OF AITKEN MODE AMMONIUM SULFATE PARTICLES BY $\alpha$ -PINENE OZONOLYSIS**

This chapter discusses the characterization and use of a flow tube reactor to study the growth of ammonium sulfate seed particles by  $\alpha$ -pinene ozonolysis under dry conditions. This work has been previously published under the following reference:

Justin M. Krasnomowitz, Michael J. Apsokardu, Christopher M. Stangl, Lee Tiszenkel, Qi Ouyang, Shanhu Lee & Murray V. Johnston (2019) Growth of Aitken mode ammonium sulfate particles by  $\alpha$ -pinene ozonolysis, *Aerosol Science and Technology*, 53:4, 406-418, DOI: 10.1080/02786826.2019.1568381

#### **3.1 Atmospheric Effects of Aitken Mode Particles**

Aitken mode particles span a size range of about 10-100 nm in diameter and can represent the largest number concentration of particles in ambient air<sup>1</sup>. Particles in this mode have potential to impact climate as they grow in size and are able to be activated as cloud condensation nuclei (CCN)<sup>2,3</sup>. In particular, the fraction of particles that are activated as CCN increase substantially with increasing particle diameter in the 50-100 nm size range<sup>3,4</sup>. For this reason, a thorough understanding of the chemical processes behind Aitken mode particle growth is needed so that growth rates in the atmosphere can be accurately predicted along with their climate impact. The goal of this work is to study the mechanism and quantify the amount of growth of ammonium sulfate seed particles in the Aitken mode size range by  $\alpha$ -pinene ozonolysis.

A substantial portion of ambient particle growth occurs by formation of secondary organic aerosol (SOA), and atmospheric models have a difficult time accurately predicting its contribution to aerosol mass loading<sup>5,6</sup>. Oxidation of biogenic volatile organic compounds (BVOCs) leads to the formation of products over a wide range of volatilities<sup>5,7</sup>. One such BVOC,  $\alpha$ -pinene, accounts for half of total monoterpene emissions<sup>8</sup> and is the precursor studied in this work. Reaction of BVOCs with ozone or OH produce highly oxidized products in the gas phase that are nonvolatile enough to nucleate and grow particles<sup>9-12</sup>. Most of these products are formed through an autoxidation mechanism<sup>13-16</sup>.

Determining particle growth rates from BVOC oxidation requires knowledge of the yield of molecular products that are nonvolatile enough to grow particles at their condensation rates. The effective saturation vapor pressure increases with increasing radius-of-curvature of the gas-particle interface (i.e. Kelvin effect). This effect becomes substantial for particles in the low nanometer size range, meaning that some compounds which grow larger Aitken mode particles at the condensation rate may not efficiently grow smaller nucleation mode particles. The definitions of terms in the literature used to describe nonvolatile oxidation products have evolved over time<sup>13,17,18</sup>. Tröstl et al. (2016)<sup>18</sup> proposed that highly oxidized molecules (HOMs) be defined as the full range of gas-phase species detected by nitrate ion ( $\text{NO}_3^-$ ) chemical ionization in an atmospheric pressure interface time-of-flight mass spectrometer (CI-API-TOF), whereas extremely low volatility organic compounds (ELVOCs) are the subset of detected species that are expected to have low enough vapor pressures to nucleate and condensationally grow particles in the low nanometer size range<sup>13</sup>. To make this distinction, Tröstl et al. (2016)<sup>18</sup> used molecular formulas obtained with

accurate mass measurements to calculate the corresponding saturation vapor pressures ( $C^*$  in units of  $\text{g}/\text{m}^3$ ), based on the volatility basis set (VBS)<sup>19</sup>.

Yields for HOM formation from  $\alpha$ -pinene ozonolysis were first reported by Ehn et al. (2014)<sup>13</sup> based on gas phase measurements of  $\alpha$ -pinene oxidation products by  $\text{NO}_3^-$  CI-APi-TOF. They reported a molar yield of 7% per precursor molecule that reacted with ozone, corresponding to a mass yield of 14% based on the assigned ion molecular formulas. These measurements were performed at 289K and 63% RH using a flow-through chamber having a residence time of ~45 min. Uncertainties were estimated to be 50% of the reported values. Using similar gas phase measurements, Jokinen et al. (2015)<sup>14</sup> reported a HOM yield for  $\alpha$ -pinene ozonolysis of 3.4% with an uncertainty of 1.7 to 6.8% for experiments performed at 293K and 25% RH using a fast flow tube reactor with a 40 s residence time. Since then, other studies using  $\text{NO}_3^-$  CI-APi-TOF have reported HOM yields in the 3-6% range<sup>20,21</sup>. While all of these reported yields are based on gas phase measurements with  $\text{NO}_3^-$  chemical ionization, they do differ slightly in the subset of detected ions used to calculate the yield and the experimental conditions studied, which may contribute to the range of values reported. Table 3-1 summarizes these measurements and the experimental conditions under which they were performed.

Three factors can affect the prediction of HOM yields from gas phase measurements. First, the definition of HOMs is based on a specific set of ions detected with chemical ionization, which may or may not include all relevant molecular species. Second, particle size-dependent phenomena such as the Kelvin effect on molecular volatility must be inferred from molecular formulas when considering which subset of detected ions to include in the yield calculation. Third,

they do not take into account the possibility of heterogeneous chemical reactions that may add to the particle growth rate<sup>22</sup>. Measured particle growth rates tend to be underestimated by CI-APi-TOF measurements, e.g. see Figure 2c and Figure 3 of Ehn et al. (2014)<sup>13</sup> and Figure 1d of Tröstl et al. (2016)<sup>18</sup>, suggesting that there may be a systematic error associated with gas phase measurements.

In the work presented here, we measure changes in the diameter of seed particles in the 40-80 nm size range when they are exposed to the products of  $\alpha$ -pinene ozonolysis in a flow tube reactor. Measured particle growth is combined with a kinetic model to confirm a condensational growth mechanism and determine the molar yield of condensable organic molecules for particles in this size range. For readability and consistency with the literature, we refer to the yield measured here as a “HOM” yield. However, the yield we obtain from particle size measurements is not exactly the same parameter as that obtained from gas phase measurements. The relationship between the two will be discussed.

### **3.2 Flow Tube Reactor to Study Particle Growth**

The flow tube reactor and experimental setup used in this work are shown in Figure 3-1. The reactor consists of a quartz tube 150 cm long and 20 cm i.d. with stainless steel funnels extending from both ends. These funnels are 18 cm long and taper down to a final i.d. of 5 cm. The total volume of the reactor assembly is 52 L.

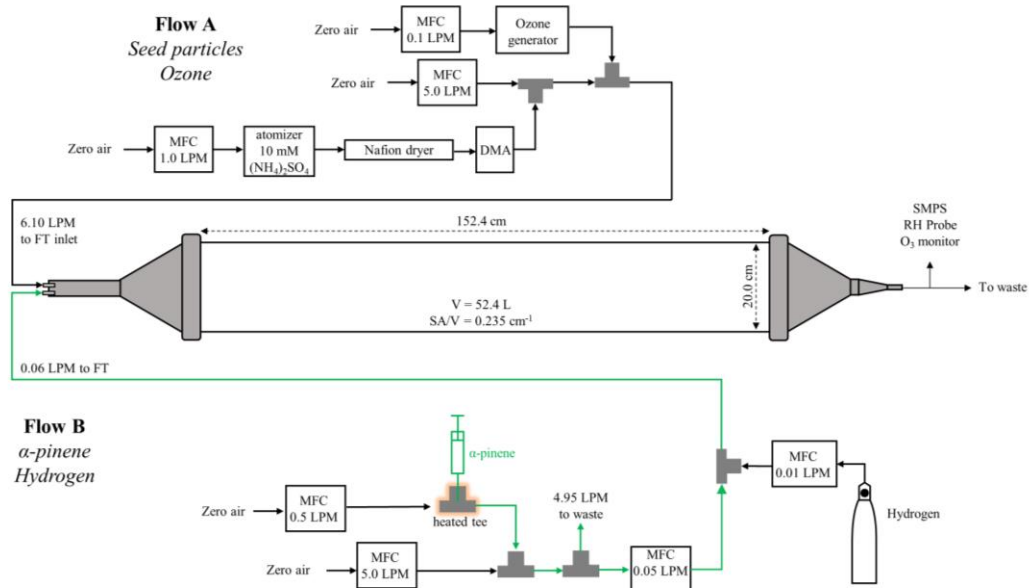


Figure 3-1. Experimental setup and flow tube reactor. Flow A contains seed particles and ozone while Flow B contains  $\alpha$ -pinene vapor and hydrogen gas.

The optimum air flow rate through the reactor was determined experimentally by injecting 30 s plugs of 60 nm dia. ammonium sulfate particles through the flow tube and measuring the particle number concentration at the exit as a function of time with a condensation particle counter (3788 CPC, TSI Inc., Shoreview, Minnesota). The goal was to experimentally determine the air flow conditions that produced the smallest distribution of particle residence times in the flow reactor. From these experiments, it was determined that a 6 L/min major air flow rate (Flow A in Figure 3-1) produced a narrow range of residence times while at the same time minimizing the impact of air recirculation in the tube. Figure 3-2 shows the residence time distribution of particles using these flows. The average distribution was determined from 5 individual plug injections and the shaded region of the figure shows one standard deviation. The peak of the distribution was  $232 \pm 15$  s, and the full width at

half maximum was 81 s. A small recirculation peak was observed at slightly more than twice the average residence time, but recirculation consistently represented less than 10% of the total distribution.

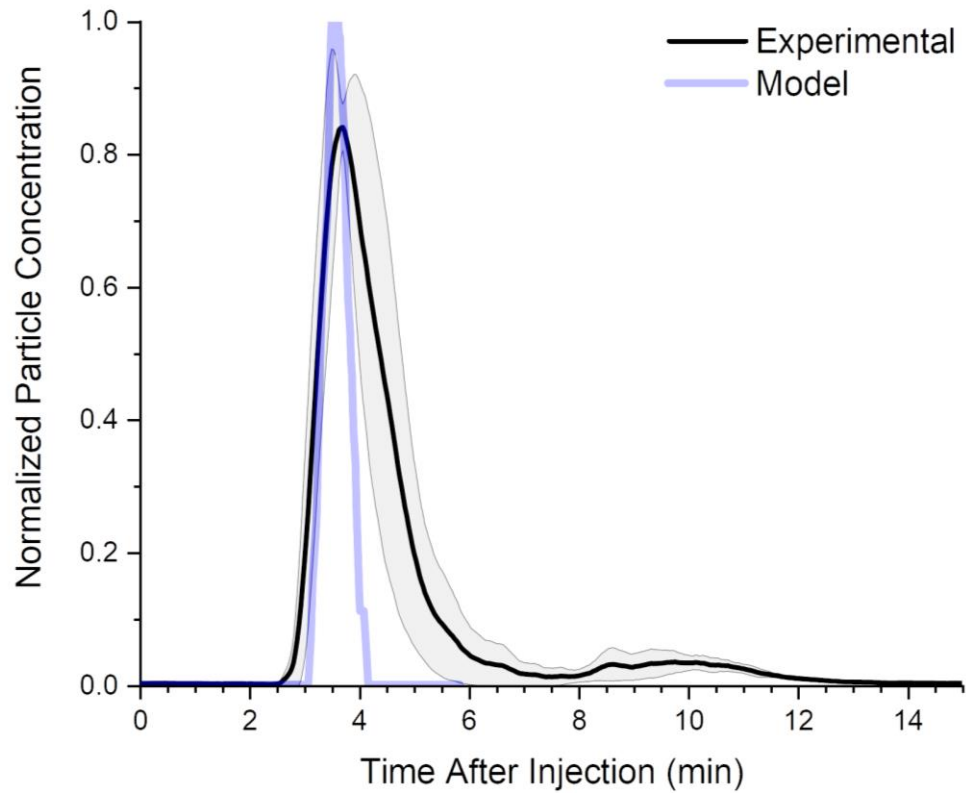


Figure 3-2. Residence time distribution of particles exiting flow tube. Dark line shows average distribution of five trials. The gray shaded region represents one standard deviation. The blue line represents the modeled residence time using the particle tracing module in COMSOL.

### 3.3 Simulations of Flow Within the Flow Tube Reactor

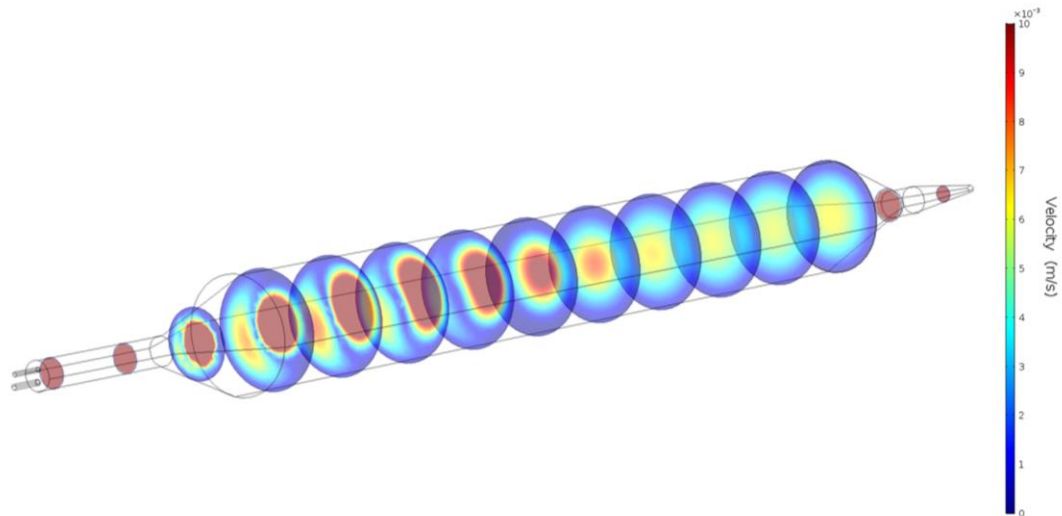


Figure 3-3. Calculated velocity through the flow tube shown as vertical slices along the length of the reactor.

The flow tube reactor used in this work was recreated in COMSOL Multiphysics 5.3a (Stockholm, Sweden, <http://www.comsol.com>) to perform computational fluid dynamics (CFD) calculations to characterize the flow throughout the reactor and compare with experimental measurements. The flow tube geometry was recreated in COMSOL as a 3-D model, and COMSOL's finite element method was used to solve for flows throughout. The geometry was meshed using a normal sized free tetrahedral mesh consisting of  $2 \times 10^5$  elements with an average quality of 0.66. The element quality is a measure of cell distortion with a value of 1 indicating perfect element shape. The model was tested using finer mesh densities to ensure reproducible results and no mesh dependence was observed. Once meshed, a stationary laminar flow model was solved using the inlet flows used in the growth

experiments; 6.1 L/min in Flow A and 0.06 L/min in Flow B and the flow of the outlet was assumed to be at atmospheric pressure. The evolution of the flow profile is shown in Figure 3-3 by velocity slices down the length of the tube. A laminar flow profile develops quickly in the initial mixing tube before expansion. Once the flow reaches the reactor and begins to expand, a recirculation zone appears in the area the main flow has not occupied. This recirculation persists to about half way into the tube, where a laminar profile is re-established throughout the entire width of the tube and maintained the rest of the way including the reduction in diameter to the outlet. Similar recirculation regions have been observed in other CFD studies of flow tube reactors<sup>23</sup>.

The particle tracing module within COMSOL was coupled to the CFD model to calculate the distribution of particle residence times in the flow tube. For these calculations, 300 particles with an 80 nm diameter were released over a 30 s period from the Flow A inlet as a density function from the center, and the times at which they exited the assembly were traced. The calculated and measured residence times show excellent agreement as shown in Figure 3-2. Since no particles in the simulation entered the recirculation region, the small recirculation peak in the experimental data was not replicated in the simulation. Gas-phase species, however, distribute evenly across the different regions of the flow tube, and if the system is given enough time to reach steady state, the gas phase mixing ratio becomes independent of location in the flow tube. As discussed in Section 3.6, the calculated equilibration time matches the measurement.

### 3.4 Particle Growth Experiments

For the experiments described here, the major flow (Flow A in Figure 3-1) contained seed particles and ozone, while the minor flow (Flow B in Figure 3-1) contained  $\alpha$ -pinene and hydrogen gas (99.999% Keen Gas, Newark, DE). Ammonium sulfate seed particles were generated by atomizing (TOPAS ATM226, Dresden, Germany) a solution of ammonium sulfate (99.9995%, Sigma-Aldrich Co., St. Louis, MO). The resulting polydisperse aerosol was sent through a Nafion dryer (MD-700, Perma Pure, Lakewood, NJ) to decrease the relative humidity (RH) of the surrounding air to 10%, which is substantially below the efflorescence RH of ammonium sulfate ( $35\pm 2\%$  at 298 K)<sup>24</sup>. The dry particles were then size-selected with a model 3080 classifier and model 3085 differential mobility analyzer (DMA) both from TSI Inc. The flow of monodisperse particles was mixed with ozone and sent into the flow tube. Ozone was generated from an ozone monitor (model 42C, Thermo Fischer Scientific Inc., Waltham, MA), and the mixing ratio was adjusted by changing the lamp intensity. All flows were maintained by mass flow controllers (MFC, Dakota Instruments Inc., Orangeburg, NY). The flow tube temperature for these experiments was 297 K.

Liquid  $\alpha$ -pinene (Sigma-Aldrich Co.) was injected at a rate of 0.05  $\mu\text{L}/\text{min}$  into a gently heated air flow of 50 mL/min using a 100  $\mu\text{L}$  syringe (Hamilton Company, Reno, NV) and a syringe pump (New Era Pump Systems Inc., Farmingdale, NY). This air flow was mixed with a larger flow of 5 L/min to dilute the vapor, and then 50 mL/min of the diluted air flow was sent into the reactor. For the experiments described here, the mixing ratio of  $\alpha$ -pinene in the flow tube was 11 ppbv. A small flow of 10 mL/min of hydrogen gas was mixed with the  $\alpha$ -pinene flow before entering the tube. The hydrogen was added to act as an OH scavenger<sup>25</sup> and had a final

concentration of 0.1 % by volume. The addition of an OH scavenger is necessary as the hydroxyl radical is produced by  $\alpha$ -pinene ozonolysis with a reported yield of 85%<sup>26</sup> and could complicate the interpretation of results by reacting with additional  $\alpha$ -pinene molecules. While the reported HOM yield from OH oxidation is almost an order of magnitude lower than that of ozone oxidation<sup>14</sup>, it is important to scavenge the OH to ensure that the measured HOM yield is specifically for the ozonolysis reaction.

Aerosol exiting the flow tube was monitored with a scanning mobility particle sizer (SMPS; TSI Inc.), an ozone monitor (Model 49i, Thermo Fisher Scientific Inc.) and an RH probe (Traceable, Thermo Fisher Scientific Inc.). The SMPS used here consisted of a 3081 DMA and 3788 CPC to scan the particle distribution between 10-400 nm mobility diameter every 2 minutes.

The experiments described here were conducted by first introducing seed particles along with ozone at its lowest mixing ratio of approximately 30 ppbv. The addition of ozone alone did not cause any change in the particle size distribution. Once the system stabilized,  $\alpha$ -pinene was introduced, giving a mixing ratio of 11 ppbv in the flow tube. The system was allowed to stabilize until consistent (<10% variation) ozone mixing ratio, particle size distribution and number concentration were obtained for at least 15 min. After stabilization, the lamp intensity and corresponding ozone mixing ratio were systematically incremented. In total, five ozone mixing ratios were investigated, which spanned the range 30-250 ppbv.

Molecular composition measurements by high-resolution electrospray ionization mass spectrometry (HR-ESI-MS) were performed using a Thermo Q-Exactive Orbitrap mass spectrometer to characterize the organic material condensing

onto the particles. For these measurements particles were collected onto a quartz microfiber filter (GF/D, Whatman, Maidstone, UK) at the exit of the flow tube using the highest ozone mixing ratio (250 ppbv) and middle seed particle diameter (60 nm). The organic material was then extracted using acetonitrile (Optima grade, Fisher Scientific, Hampton, NH) and concentrated under vacuum to a final concentration of approximately 0.1  $\mu\text{g}/\mu\text{L}$ . This extract was then analyzed using direct infusion on the Orbitrap operated in negative mode. Data processing and formula assignment of the resulting mass spectra was then performed as described in Tu et al. (2016)<sup>27</sup>.

### 3.5 Kinetic Modeling of Particle Growth

The amount of seed particle growth obtained for each ozone increment was evaluated with respect to the formation of HOMs produced by  $\alpha$ -pinene ozonolysis. Modeling the formation of HOMs was done recursively by updating reactant and product concentrations each second for the duration of the flow tube residence time. Once the gas phase concentration is calculated, it can then be used to predict the diameter change of a particle, assuming that condensation is a collision-limited process, using Eq. 3-1 adapted from Apsokardu and Johnston (2018)<sup>22</sup>:

$$(3-1) \quad \frac{\partial d}{\partial t} = \frac{c}{2} \gamma [HOM]_t \beta_d V_{HOM}$$

where  $c$  is the mean thermal velocity,  $\gamma$  is the uptake coefficient (assumed to be 1 in this work),  $[HOM]_t$  is the time-dependent gas-phase HOM mixing ratio,  $\beta_d$  is the mass flux correction factor and  $V_{HOM}$  is the molecular volume. For these calculations, HOMs were assumed to have an average molecular weight of 200 g/mol and a density of 1.2 g/cm<sup>3</sup>. The predicted diameter change can then be fit to the experimental data by adjusting the HOM yield and thus the HOM mixing ratio.

Multiple processes occurring within the tube are accounted for in the model. First is the oxidation of  $\alpha$ -pinene by ozone, based on the respective mixing ratios and a second order rate constant ( $k_{II}$ ) of  $8.4 \times 10^{-17} \text{ cm}^3 \text{ molec}^{-1} \text{ s}^{-1}$ <sup>28</sup>. Second is the formation of HOMs from the ozonolysis reaction, which will be discussed in detail in Section 3.8. Third is wall loss of HOMs, modeled as a diffusion limited process based on Hanson and Eisele (2000)<sup>29</sup> and accounting for entry effects discussed in Knopf et al. (2015)<sup>30</sup>:

$$(3-2) \quad k_{WL} = N_{Shw}^{eff} \frac{D}{r^2} 2$$

where  $k_{WL}$  is the wall loss rate constant,  $N_{Shw}^{eff}$  is the effective Sherwood number,  $r$  is the radius of the flow tube,  $D$  is the gas phase diffusion coefficient, and it is assumed that HOMs are nonvolatile enough that the sticking probability is 1. The Sherwood number was varied to account for entry effects in the beginning of the flow tube. However, this did not have a significant effect on HOM mixing ratio in the flow tube since only a small amount of HOMs are produced in this region. Modeling wall loss in this way gives an average  $k_{WL} = 2.0 \times 10^{-3} \text{ s}^{-1}$  assuming a constant flow tube radius of 10 cm.

In addition to the constant radius calculation above, wall loss was also approximated by varying the effective diameter in the various stages of the flow tube assembly. For this calculation, particle residence time in the initial mixing tube was 3 s, and the radius for wall loss during this time period was taken as the 2.375 cm radius of the tube. During expansion in the funnel and first part of the flow tube, the effective radius increased from 2.375 cm to 10 cm at the point where laminar flow was fully established across the width of the flow tube. The particle residence time in this expanding region was 60 s, and it was assumed that the effective diameter for wall

loss increased linearly with time in this region. The radius was then held constant at 10 cm for the remaining portion of the flow tube, which covered a period of 124 s. Finally, the radius was assumed to decrease linearly from 10 cm back to 2.375 cm over the final 38 s spent in the outlet funnel. Modeling wall loss in this way gave a time averaged  $k_{WL} = 6.4 \times 10^{-3} \text{ s}^{-1}$ . As discussed later, the difference between these two methods of calculating wall loss did not give an appreciable difference in the calculated molar yield of HOMs.

The final process accounted for in the model was loss of HOM to the condensation sink (CS). The condensation sink was calculated for each size distribution according to Eq. 3-3 adapted from Dal Maso et al. (2002)<sup>31</sup>.

$$(3-3) \quad k_{CS} = 2\pi D \sum \beta_{ai} d_{pi} N_i$$

where  $k_{CS}$  is the first order rate constant for loss to the condensation sink,  $d_{pi}$  is the particle diameter and  $N_i$  is the number concentration at the diameter. However, the value of the condensation sink is not constant throughout the flow tube as the size distribution begins as the seed distribution and evolves over the residence time of the tube into what is measured at the end. For this reason, we begin with the condensation sink as the value calculated from the seed distribution and increase it as a function of  $t^2$  as discussed by Ezhova et al. (2018)<sup>32</sup>. The difference this can cause in CS value over the course of an experiment is shown in Figure 3-4. Because the condensation sink increases at most by a factor of two in these experiments, the assumed time dependence does not have a significant impact on the calculations. However, the condensation sink is very different for the three size-selected aerosols studied in this work, so it is imperative to consider its effect on particle growth. Therefore, it is

likely the size dependence observed in the growth experiment can be entirely explained by the change in CS for different initial seed diameters.

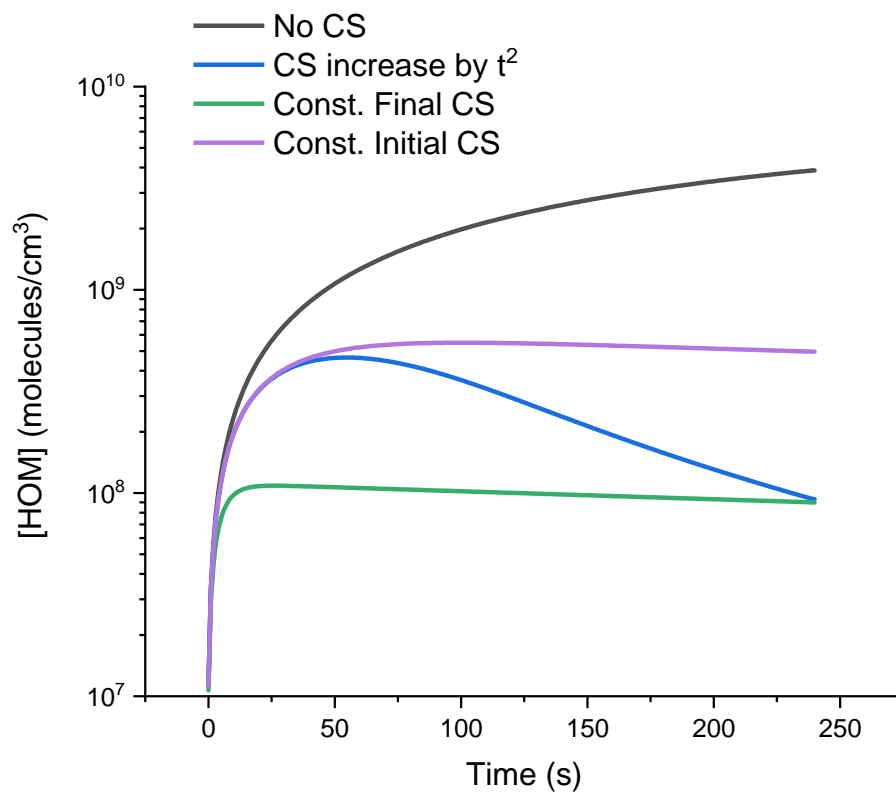


Figure 3-4. HOM mixing ratio over time under different CS conditions.

Taking the discussed processes into account, HOM production can be summarized by Eq. 3-4:

$$(3-4) [HOM]_{t+\Delta t} = [HOM]_t + k_{II}[\alpha P]_t[O_3]_t y \Delta t - k_{WL}[HOM]_t \Delta t - k_{CS}[HOM]_t \Delta t$$

where  $[HOM]_t$ ,  $[\alpha P]_t$  and  $[O_3]_t$  are the respective mixing ratios at time  $t$ ,  $\Delta t$  is the time increment,  $k_{II}$  is the second order rate constant, and  $y$  is the molar yield of HOM for  $\alpha$ -pinene ozonolysis.

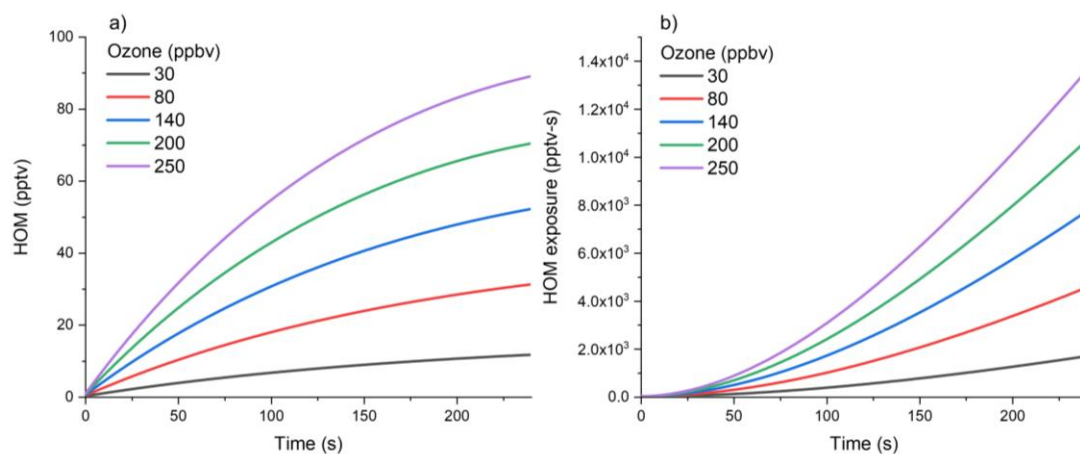


Figure 3-5. Calculated mixing ratio (a) and exposure (b) of HOMs for each ozone concentration over the residence time of the flow tube. These plots used a molar yield of 12.5% for  $\alpha$ -pinene ozonolysis with wall loss modeled as a constant diameter and condensation sink (seed particles of 40 nm) for the experiment shown in Figure 3-5.

Figure 3-5 gives examples of this calculation for the  $\alpha$ -pinene and ozone mixing ratios used in the experiment with 40 nm dia. seed particles. Figure 3-5a shows the HOM mixing ratio and Figure 3-5b shows the HOM exposure (pptv-s), both as a function of time in the flow tube. Because HOM mixing ratio builds up slowly at the beginning of the flow tube, the incompletely developed laminar flow profile (Figure 3-3) exerts a relatively small effect on HOM mixing ratio and exposure at the outlet. These calculations assume a HOM yield of 12.5% and use the constant tube

radius method of determining wall loss. HOM exposure is obtained by integrating the HOM mixing ratios as shown in Eq. 3-5:

$$(3-5) \quad E_t = \int_{t=0}^t [HOM]_t dt$$

where  $E_t$  is total exposure at time  $t$  in the flow tube. At the flow tube exit, the HOM mixing ratio and exposure increase approximately linearly with ozone mixing ratio under the conditions used in the experiment.

In the work that follows, the calculated particle diameter at the flow tube exit is determined by integrating Eq. 3-1 over time using the time-dependent HOM mixing ratio determined from Eq. 3-4.

### **3.6 Particle Growth Measurements**

Seed particle growth by  $\alpha$ -pinene ozonolysis was studied as a function of particle diameter and ozonolysis reaction rate. The reaction rate was systematically varied through successive increments of the ozone mixing ratio. The seed particles were composed of ammonium sulfate at low RH (10%), rendering them nominally unreactive with respect to particle-phase chemical processes.

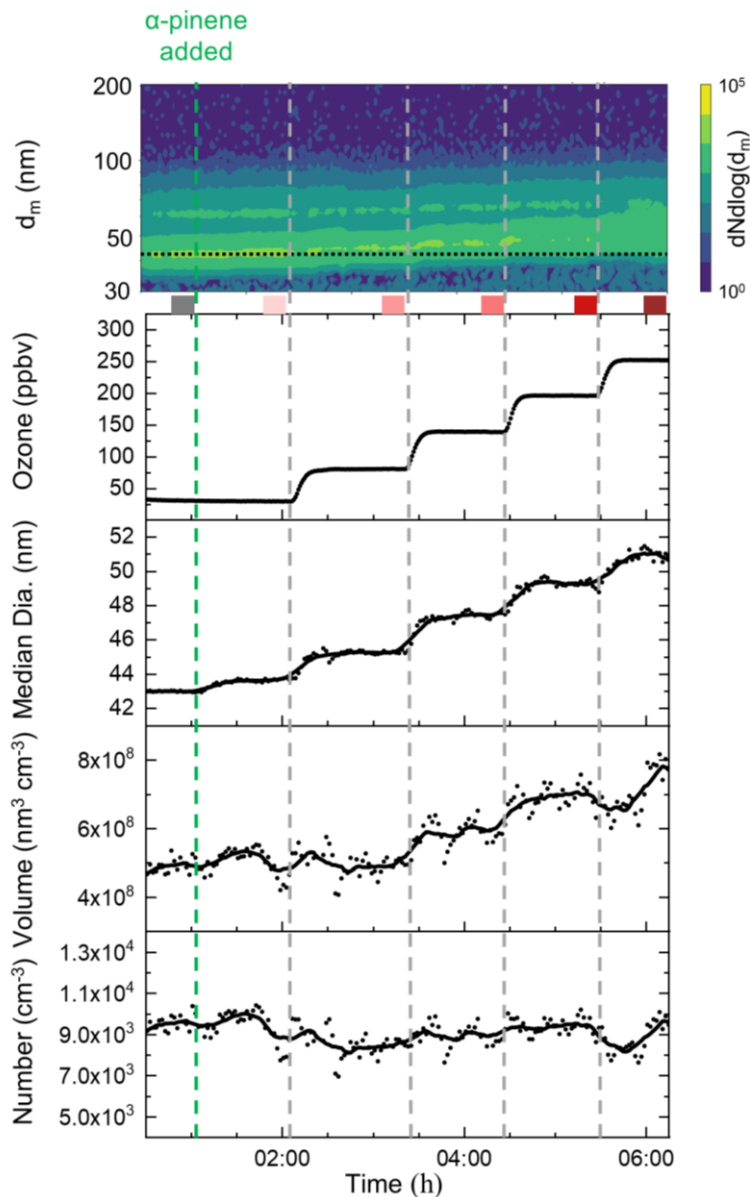


Figure 3-6. Growth experiment of 40 nm ammonium sulfate seed particles. At the top is a contour plot of aerosol size distribution measured by SMPS, followed by ozone mixing ratio, median particle diameter, volume and particle number concentration exiting the flow tube. The green vertical line indicates when  $\alpha$ -pinene vapor injection began. Gray vertical lines indicate when increments of the ozone mixing ratio were made. Dots represent raw data and the black lines are ten-point moving averages. Bars below the contour plot indicate the time where data were averaged for further analysis.

One such experiment is shown in Figure 3-6 starting with 40 nm dia. seed particles. At the start of the experiment, seed particles and ozone were sent through the reactor and a stable flow was achieved. At the time point indicated by the vertical dashed green line,  $\alpha$ -pinene vapor was introduced, which caused the seed particles to grow as indicated by increases in the median diameter (third panel) and volume (fourth panel) of the aerosol. After the size distribution stabilized, the ozone mixing ratio was incremented up to the next value. The median diameter and volume increased again, and after the new size distribution stabilized, this process was repeated. In all, four ozone increments were performed, and their time points are shown as vertical dashed gray lines in Figure 3-6. The time between ozone increments was approximately one hour as it took the reactor close to 30 minutes to reach steady-state and then particle size distributions were averaged over the remaining time period. The experimentally observed equilibration time period for gas phase reactants matched the CFD calculated time period, providing an additional consistency check between measured and calculated flow properties.

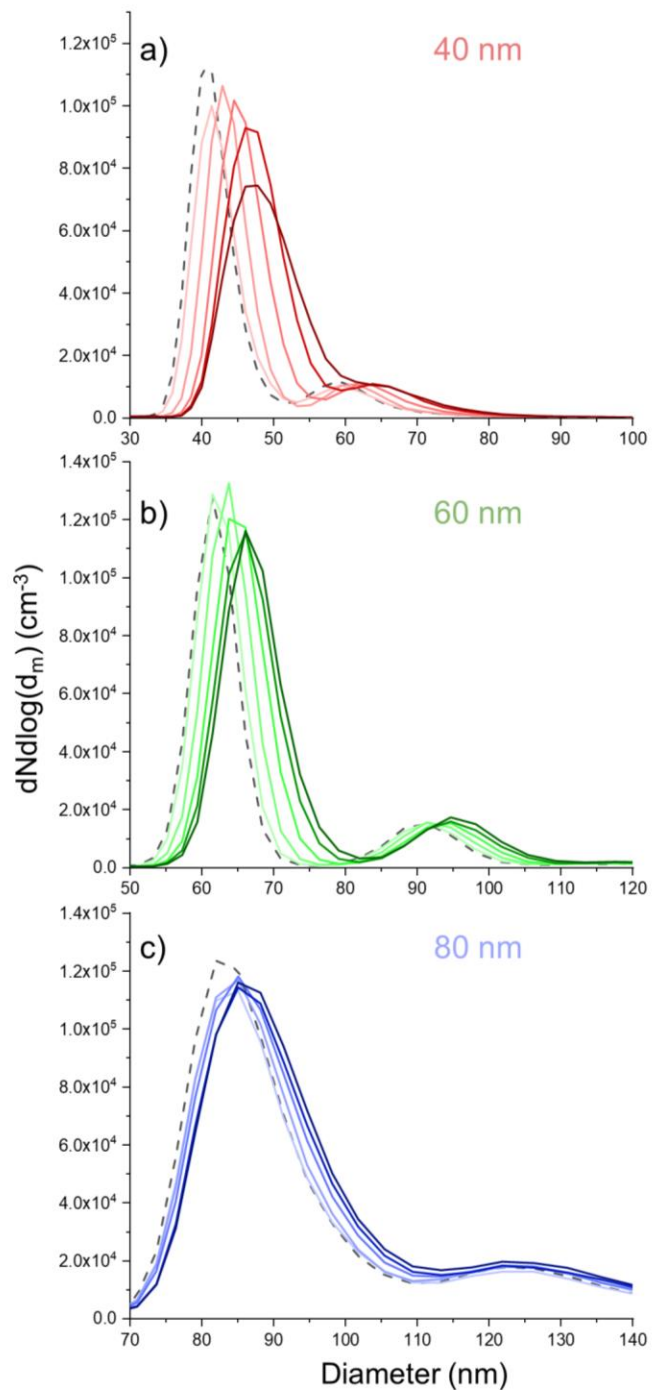


Figure 3-7. Average size distribution for each ozone mixing ratio in experiments with 40, 60 and 80 nm dia. seed particles. Approximate ozone mixing ratios are 30, 80, 140, 200 and 250 ppbv.

An interesting feature of Figure 3-6 is the much smaller fluctuation of the median diameter than the aerosol volume. We attribute the variation in the aerosol volume measurement mainly to fluctuation of the aerosol output by the atomizer. Superimposed on this fluctuation may be an additional contribution from the measurement uncertainty of the SMPS. Since neither of these variations affects particle residence time in the reactor, the median diameter of the aerosol is a more precise indicator of particle growth. While equations exist to fit the entire size distribution and normalize variations in residence times such as those outlined in Kuwata and Martin (2012)<sup>33</sup>, they could not be directly used in this work because of the nonuniform HOM mixing ratio throughout the tube. Instead, median diameter is used as an indicator for particle growth, because the precision and reproducibility of the measurement are better.

Particle growth is also indicated by changes in the average size distribution for each ozone increment. Particle size distributions for the experiment in Figure 3-6 are shown in Figure 3-7a. The time periods over which size distributions were averaged are shown as horizontal bars just above the ozone plot in Figure 3-6. With each ozone increment, the distribution shifts to a larger particle size and broadens. This broadening and its characteristic tail to the high diameter side of the distribution are attributed to the shape of the residence time distribution in Figure 3-2. In addition, there is a second peak observed, caused by doubly charged seed particles that passed through the DMA used for size selection and subsequently lost a charge prior to analysis by SMPS at the flow tube exit.

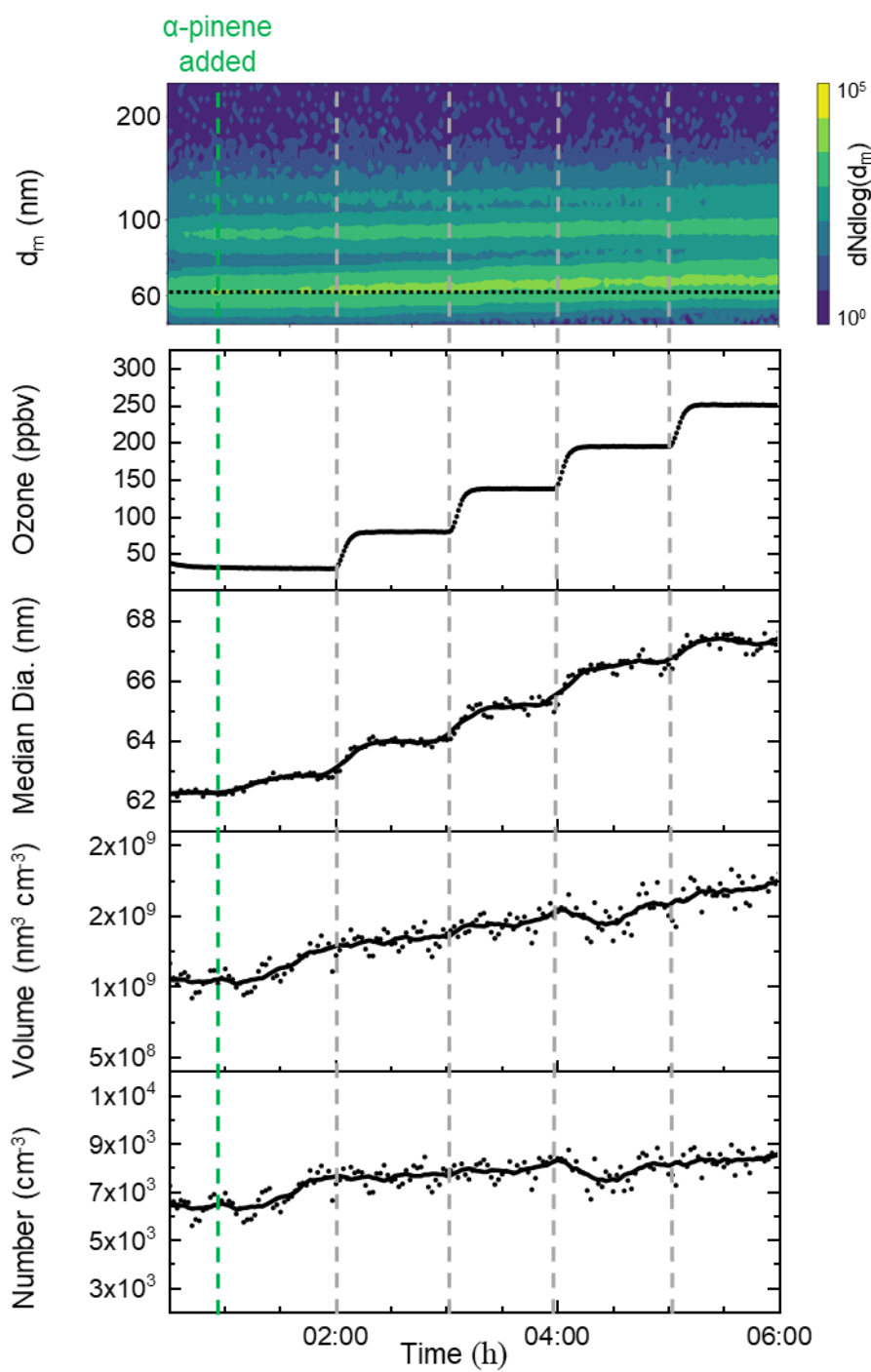


Figure 3-8. Growth experiment using 60 nm ammonium sulfate seed particles.

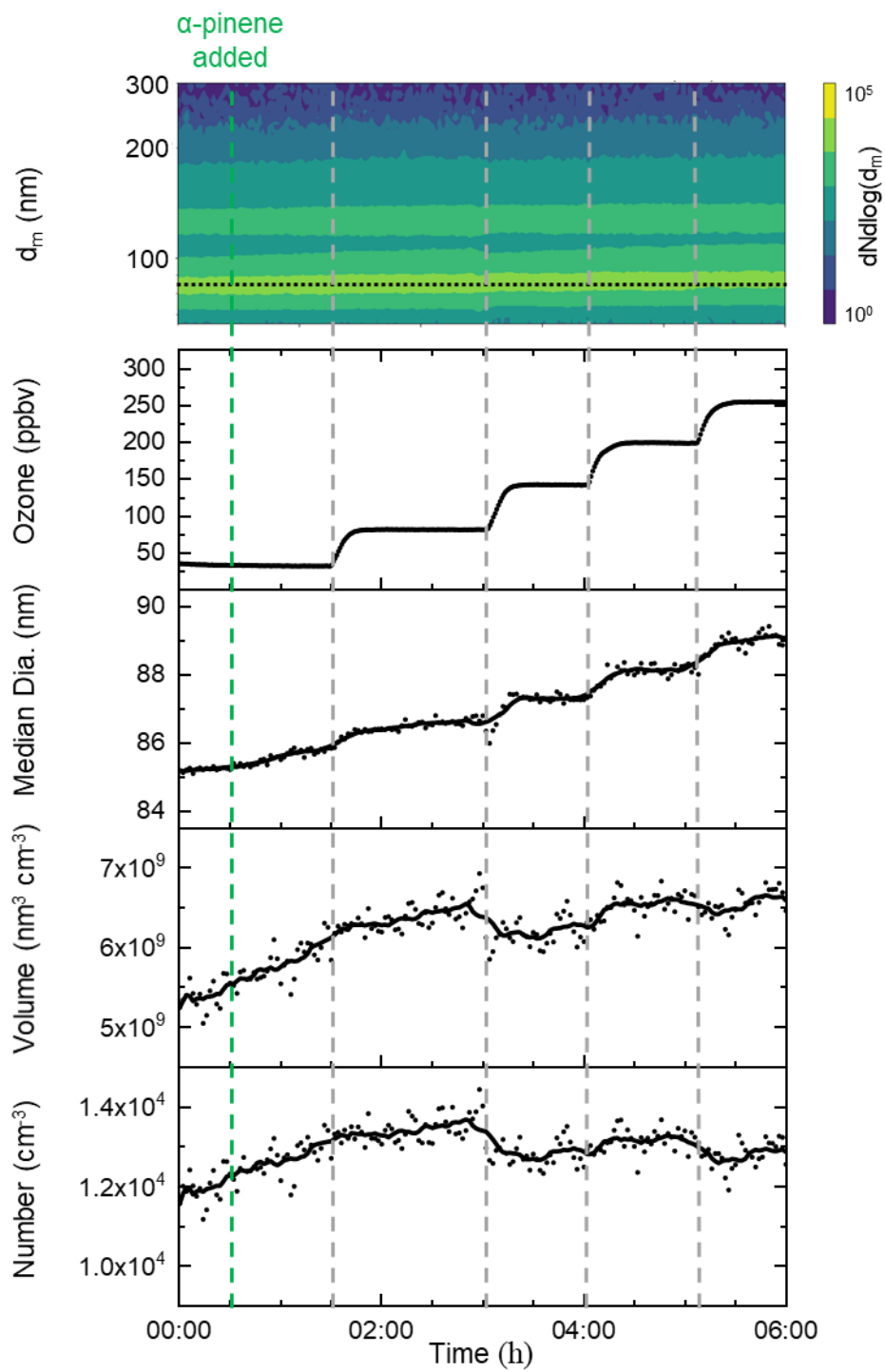


Figure 3-9. Growth experiment using 80 nm ammonium sulfate seed particles.

The experiment in Figure 3-6 was repeated for 60 and 80 nm dia. seed particles. Plots for these experiments are shown in Figures 3-8 and 3-9, respectively, and the size distributions are shown in Figures 3-7b and 3-7c. For each seed particle size, the distribution shifts to a larger particle diameter and broadens as the ozone mixing ratio increases. The linear scale for particle diameter is shifted among the plots in Figure 3-7 to align the seed particle size distributions vertically, which illustrates a key observation in these experiments. The diameter growth of larger diameter seed particles is less than that observed for smaller diameter seed particles. This phenomenon and other details of particle growth are discussed below.

### **3.7 Mechanism of Particle Growth**

The experimental results in Figures 3-6 to 3-9 are summarized in Figure 3-10, where the change in median diameter (difference between median diameter with and without  $\alpha$ -pinene ozonolysis) is plotted vs. ozone mixing ratio. In all, data from six separate experiments are shown, two repeat experiments for each of the three seed particle sizes. The replicate trials at each initial seed diameter show good agreement, and the diameter growth for each seed size is linear with increasing ozone mixing ratio.

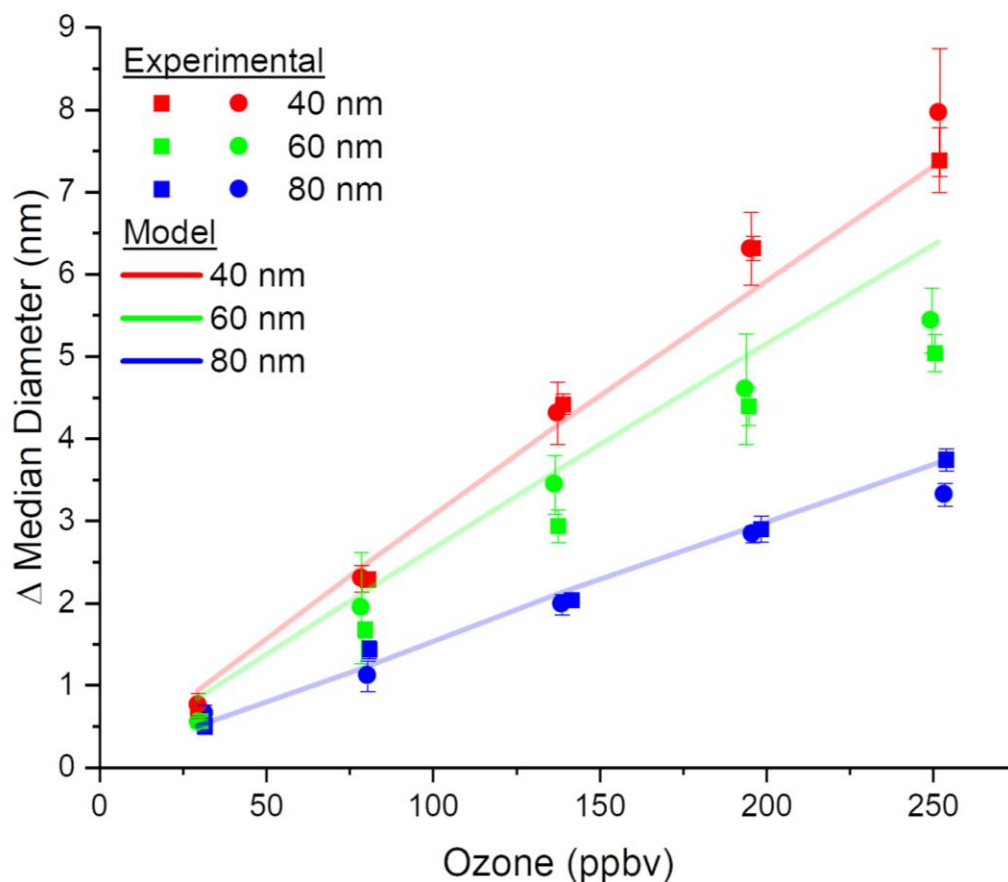


Figure 3-10. Seed particle growth (increase in median diameter) vs ozone mixing ratio. Squares and circles represent duplicate experiments with error bars representing one standard deviation. The lines represent predicted particle growth using modeling as described in section 2.4 with a molar yield of 12.5% for formation of HOMs from  $\alpha$ -pinene ozonolysis.

Apsokardu and Johnston (2018)<sup>22</sup> have discussed the particle size dependence of growth rates for different growth mechanisms. The growth rate is, to a first approximation, independent of particle diameter for growth processes limited by the condensation rate of gas phase precursors. Examples include condensation of nonvolatile compounds whose evaporation rates are negligible, and uptake of

semivolatile compounds that react so quickly in the particle phase to give a nonvolatile product that their uptake is limited by the condensation rate. In contrast, uptake of semivolatile compounds by reaction in the particle phase at a rate slower than the collision-limited condensation rate would exhibit an increasing growth rate with increasing particle size. For the growth experiments performed here, dry ammonium sulfate seed particles are expected to be inert with respect to particle-phase chemistry. Therefore, growth is expected to be independent of seed particle diameter assuming that the condensation sink remains constant. However, the condensation sink is very different for the 40, 60, and 80 nm seed particle diameter experiments. As discussed below, it is condensation sink associated with the different seed particles, rather than particle diameter itself, that leads to the differences among the plots in Figure 3-10. Additionally, as discussed in Chapter 1, the observed linear growth supports the argument that particle growth is dominated by a unimolecular reaction pathway and the increased mixing ratio used in the reactor are only speeding up the reaction rate not altering the products being formed.

The modeling approach described in section 3.5 was used to calculate expected diameter increases for comparison with the experimental data in Figure 3-10. The only parameter in the calculation that is different for the three particle sizes is the condensation sink for the aerosol in each experiment. All other parameters are fixed, except for the molar yield of HOM for the ozonolysis reaction ( $y$  in Eq. 4), which is adjusted to fit the calculated data to the experimental data. The solid lines in Figure 3-10 show the best-fit calculated diameter changes assuming a HOM molar yield of 12.5% and wall loss based on a constant 10 cm radius. The method used to calculate wall loss only slightly affects the HOM yield derived from the modeling. If, instead,

wall loss is calculated using the varying radius approach, the molar yield needed to fit the data is 13.5%. For either method of calculating wall loss, changing the HOM molar yield by as little as  $\pm 0.5\%$  caused the solid lines to deviate significantly from the experimental data. Taking all of these observations into account, we report the molar yield of HOM to be  $13 \pm 1\%$ .

The electrospray ionization mass spectrum of particles that were collected from the 250 ppbv ozone experiment with 60 nm seed particles is shown in Figure 3-11. The mass spectrum is dominated by  $C_xH_yO_z$  species having  $x \leq 10$ , i.e. monomers. Molecular formulas assigned from Figure 3-11 do not closely match formulas assigned from chemical ionization measurements of HOMs. This difference has been noted in previous studies and is attributed to decomposition of gas-phase HOMs once they enter the particle phase<sup>27,34-36</sup>. While a correspondence of Figure 3-11 with gas-phase HOM measurements is not expected, Figure 3-11 does provide insight for the discussion below. First, dimer signal intensities are very low. Since most dimer species are thought to be formed directly in the particle phase as discussed by Shiraiwa et al. (2014)<sup>37</sup>, it is unlikely that oligomerization in the particle phase contributed significantly to particle growth in these experiments. Second, there is no evidence of organosulfate formation, ruling out this pathway as a significant contributor to particle growth under these conditions. Finally, the spectra being dominated by monomers is evidence of HOM formation and products condense onto the particle reacting through the unimolecular pathway shown in Figure 1-5.

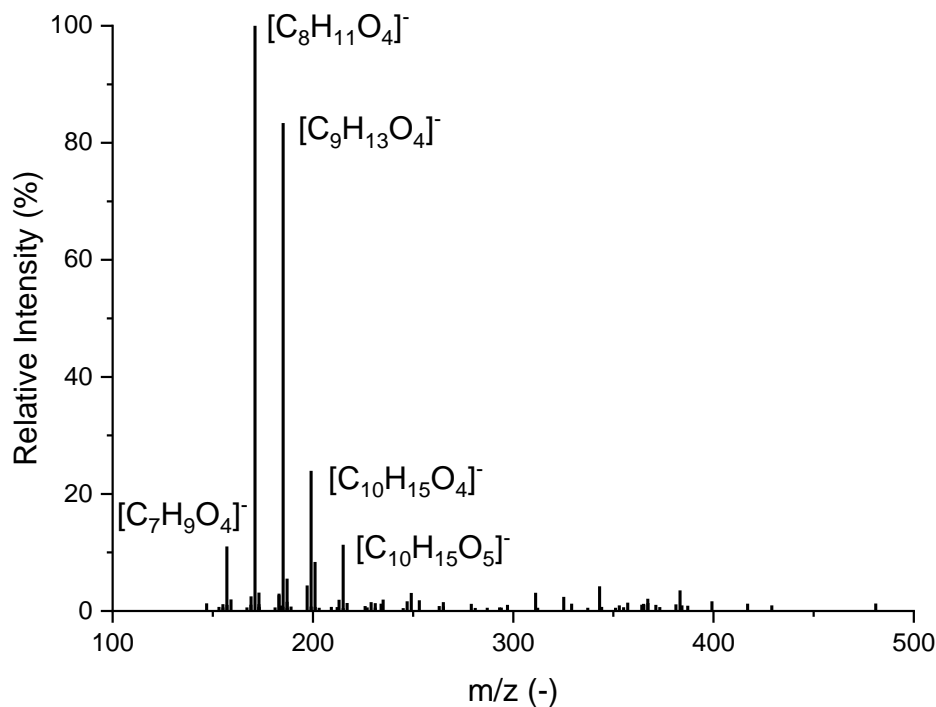


Figure 3-11. Molecular composition of particle-phase organics upon exit of the flow tube

The nano aerosol mass spectrometer (NAMS) a custom built online single particle mass spectrometer was also used to measure the quantitative elemental composition of particles exiting the flow tube. 80 nm seed particles were continuously exposed to the highest studied ozone mixing ratio (~250 ppbv) and sent direct to NAMS for analysis. The resulting mass spectrum, an average of 60 individual particle hits is shown in Figure 3-12. All expected elements are present in the measured particles including N, O and S from the ammonium sulfate seed particles. The presence of C provides additional evidence that oxidation products are condensing and

responsible for the measured particle growth. Quantitative analysis of the measured particles also provides an organic O/C ratio of  $\sim 0.6$  indicating the products that are condensing have been significantly oxidized resulting in volatilities low enough to irreversibly condense.

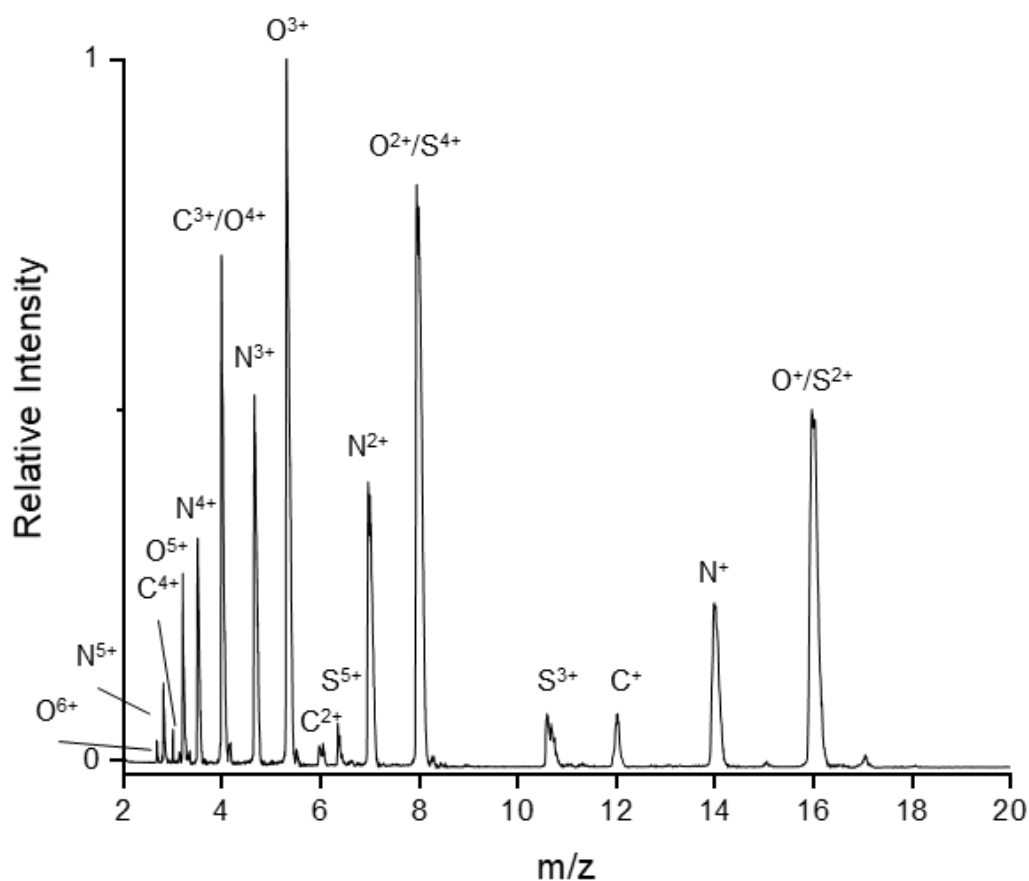


Figure 3-12. Average NAMS spectra from 60 individual particle hits. 80 nm ammonium sulfate seed particles were exposed to oxidation products formed from 11 ppbv  $\alpha$ -pinene and  $\sim 250$  ppbv ozone in the flow tube reactor.

Study	Experimental Conditions	Molar Yield (%)	Measurement Approach
Ehn et al. (2014)	2 ppbv $\alpha$ P, 170 ppbv O <sub>3</sub> 289 K, 63% RH	7 (+/- 3.5)	Determined from signal intensities of gas-phase species detected by NO <sub>3</sub> <sup>-</sup> CI-APi-TOF; measurements under predict growth of 5-50 nm particles; reaction performed in a high volume chamber
Jokinen et al. (2015)	0.1-175 ppbv $\alpha$ P, 23 ppbv O <sub>3</sub> 293 K, 25% RH	3.4 (+3.4/-1.7)	Determined from signal intensities of gas-phase species detected by NO <sub>3</sub> <sup>-</sup> CI-APi-TOF; reaction performed in a flow tube
Kirkby et al. (2016)	333 pptv $\alpha$ P, 33 ppbv O <sub>3</sub> 278 K, 38% RH	2.9 (+5.2/-1.3)	Determined from signal intensities of gas-phase species detected by NO <sub>3</sub> <sup>-</sup> CI-APi-TOF; reaction performed in a high volume chamber
Sarnela et al. (2018)	333 pptv $\alpha$ P, 33 ppbv O <sub>3</sub> 278 K, 38% RH	3.5-6.5	Determined from signal intensities of gas-phase species detected by NO <sub>3</sub> <sup>-</sup> CI-APi-TOF; reaction performed in a high volume chamber
Krasnomowitz et al. (this work)	11 ppbv $\alpha$ P, 30-250 ppbv O <sub>3</sub> 297 K, 10% RH	13 (+/- 1)	Determined from a kinetic model fit of measured diameter growth of 40-80 nm dia. seed particles; reaction performed in a flow tube

Table 3-1. Molar Yield of Condensable Molecules From  $\alpha$ -Pinene Ozonolysis

### 3.8 Comparison of Yields Based on Gas vs. Particle Phase Measurements

Table 3-1 compares the molar yield of condensable organic molecules obtained from particle growth measurements in this work to molar yields of highly oxidized molecules (HOMs) from previous gas-phase measurements with  $\text{NO}_3^-$  chemical ionization. Our reported yield (13%) is somewhat higher than the yields determined from gas-phase measurements (3-7%). Three factors that may contribute to this difference.

First is the character of gas-phase measurements. HOM yields are based on a specific set of ions detected with  $\text{NO}_3^-$  chemical ionization, the assumptions being that all relevant species are detected by this method and the ionization yield (fraction of molecules entering the mass spectrometer source region that are ionized) is fixed and known. However, if some species are not detected, then the actual HOM yield will be greater than the measured yield. We note that measured particle growth tends to be underestimated by chemical ionization measurements<sup>13,18</sup>, which suggests that some relevant species may not be detected.

Second is the character of particle-phase measurements. HOMs are thought to be highly reactive molecules that can decompose quickly in the particle phase<sup>34</sup>. If decomposition leads to formation of a more volatile product, then evaporation of the product will decrease the particle size and give a smaller apparent growth rate than predicted by HOM condensation alone. In the current experiment, the short residence time of particles in the flow tube minimizes this effect. Alternatively, it is possible that heterogeneous chemical reactions, i.e. reactions that occur within the condensed phase or at the interface between phases, could assist particle growth if they transform relatively volatile molecules that strike the particle surface into nonvolatile products

that stay in the particle phase. In this case, particle growth would be greater than that predicted by condensation of HOMs alone since a wider range of molecular species contribute to growth. The molecular composition measurements in this work rule out particle phase chemistry associated with oligomer and organosulfate formation. However, it is possible that other types of reactions may occur, particularly those occurring at an interface. If we assume a core-shell morphology for particles exiting the flow tube, i.e. a liquid secondary organic layer surrounding a solid inorganic core, then the thickness of the organic layer of particles exiting the flow tube is at most a few nanometers and the surface-to-volume ratio is high. Therefore, surface chemistry could have a rather large impact on particle growth.

Third is the impact of experimental conditions. An important difference between the gas-phase studies in Table 3-1 and ours is relative humidity (RH). If formation of the stabilized Criegee Intermediate (sCI) is a step in the formation of HOMs, then it is possible for RH to have a direct effect on measured HOM yield as water has been shown to react with sCI<sup>38,39</sup> reducing the HOMs produced and lowering the yield with increasing RH. Therefore, the higher yield reported in our work could be due in part to the lower RH. Another important difference is particle size. Most of the gas-phase experiments in Table 3-1 were focused on growth of particles on the order of a few nanometers. In this size range, the Kelvin effect exerts a huge impact on molecular volatility, and the range of molecules that can lead to particle growth is much smaller than for Aitken mode particles where the Kelvin effect is insignificant. We note that the molar yields determined by Jokinen et al. (2015)<sup>14</sup> and Kirkby et al. (2016)<sup>20</sup> excluded HOMs thought to be unimportant for growth of small nanoparticles, and their yields are much smaller than ours. The Ehn et al.

(2014)<sup>13</sup> study did include a measurement of Aitken mode particle growth, and their yield is closest to ours. Future studies will focus on higher RH and different seed particle compositions to elucidate their roles in particle growth.

### **3.9 Conclusions**

We have investigated the growth of size-selected ammonium sulfate seed particles in the 40-80 nm range by  $\alpha$ -pinene ozonolysis under dry conditions. The increase in seed particle diameter was consistent with a collision-limited condensational growth mechanism, and the magnitude of the increase allowed the molar yield of condensable organic molecules from  $\alpha$ -pinene ozonolysis to be determined. The reported HOM yield,  $13\pm 1\%$ , is somewhat higher than reported yields of HOMs measured in the gas phase with  $\text{NO}_3^-$  chemical ionization mass spectrometry. Potential reasons for this difference were discussed including factors inherent to gas phase measurements, particle phase measurements, and the experimental conditions of the various studies.

## REFERENCES

- (1) Komppula, M.; Lihavainen, H.; Hatakka, J.; Paatero, J.; Aalto, P.; Kulmala, M.; Viisanen, Y. *J. Geophys. Res. Atmos.* **2003**, *108* (D9), 4295.
- (2) Lihavainen, H.; Kerminen, V.-M.; Komppula, M.; Hatakka, J.; AAltonen, V. *J. Geophys. Res.* **2003**, *108* (D24), 4782.
- (3) Komppula, M.; Lihavainen, H.; Kerminen, V. M.; Kulmala, M.; Viisanen, Y. *J. Geophys. Res. D Atmos.* **2005**, *110* (6), 1–10.
- (4) Dusek, U.; Frank, G. P.; Hildebrandt, L.; Curtius, J.; Schneider, J.; Walter, S.; Chand, D.; Drewnick, F.; Hings, S.; Jung, D.; Borrmann, S.; Andreae, M. O. *Science* **2006**, *312* (5778), 1375–1378.
- (5) Donahue, N. M.; Kroll, J. H.; Pandis, S. N.; Robinson, A. L. *Atmos. Chem. Phys.* **2012**, *12* (2), 615–634.
- (6) Hallquist, M.; Wenger, J. C.; Baltensperger, U.; Rudich, Y.; Simpson, D.; Claeys, M.; Dommen, J.; Donahue, N. M.; George, C.; Goldstein, a. H.; Hamilton, J. F.; Herrmann, H.; Hoffmann, T.; Iinuma, Y.; Jang, M.; Jenkin, M. E.; Jimenez, J. L.; Kiendler-Scharr, a.; Maenhaut, W.; McFiggans, G.; Mentel, T. F.; Monod, a.; Prévôt, a. S. H.; Seinfeld, J. H.; Surratt, J. D.; Szmigielski, R.; Wildt, J. *Atmos. Chem. Phys.* **2009**, *9* (14), 5155–5236.

- (7) Jimenez, J. L.; Canagaratna, M. R.; Donahue, N. M.; Prevot, A. S. H.; Zhang, Q.; Kroll, J. H.; DeCarlo, P. F.; Allan, J. D.; Coe, H.; Ng, N. L.; Aiken, A. C.; Docherty, K. S.; Ulbrich, I. M.; Grieshop, A. P.; Robinson, A. L.; Duplissy, J.; Smith, J. D.; Wilson, K. R.; Lanz, V. A.; Hueglin, C.; Sun, Y. L.; Tian, J.; Laaksonen, A.; Raatikainen, T.; Rautiainen, J.; Vaattovaara, P.; Ehn, M.; Kulmala, M.; Tomlinson, J. M.; Collins, D. R.; Cubison, M. J.; Dunlea, J.; Huffman, J. A.; Onasch, T. B.; Alfarra, M. R.; Williams, P. I.; Bower, K.; Kondo, Y.; Schneider, J.; Drewnick, F.; Borrmann, S.; Weimer, S.; Demerjian, K.; Salcedo, D.; Cottrell, L.; Griffin, R.; Takami, A.; Miyoshi, T.; Hatakeyama, S.; Shimono, A.; Sun, J. Y.; Zhang, Y. M.; Dzepina, K.; Kimmel, J. R.; Sueper, D.; Jayne, J. T.; Herndon, S. C.; Trimborn, A. M.; Williams, L. R.; Wood, E. C.; Middlebrook, A. M.; Kolb, C. E.; Baltensperger, U.; Worsnop, D. R.; Dunlea, E. J.; Huffman, J. A.; Onasch, T. B.; Alfarra, M. R.; Williams, P. I.; Bower, K.; Kondo, Y.; Schneider, J.; Drewnick, F.; Borrmann, S.; Weimer, S.; Demerjian, K.; Salcedo, D.; Cottrell, L.; Griffin, R.; Takami, A.; Miyoshi, T.; Hatakeyama, S.; Shimono, A.; Sun, J. Y.; Zhang, Y. M.; Dzepina, K.; Kimmel, J. R.; Sueper, D.; Jayne, J. T.; Herndon, S. C.; Trimborn, A. M.; Williams, L. R.; Wood, E. C.; Middlebrook, A. M.; Kolb, C. E.; Baltensperger, U.; Worsnop, D. R.; Dunlea, E. J.; Huffman, J. A.; Onasch, T. B.; Alfarra, M. R.; Williams, P. I.; Bower, K.; Kondo, Y.; Schneider, J.; Drewnick, F.; Borrmann, S.; Weimer, S.; Demerjian, K.; Salcedo, D.; Cottrell, L.; Griffin, R.; Takami, A.; Miyoshi, T.; Hatakeyama, S.; Shimono, A.; Sun, J. Y.; Zhang, Y. M.; Dzepina, K.; Kimmel, J. R.; Sueper, D.; Jayne, J. T.; Herndon, S. C.; Trimborn, A. M.; Williams, L. R.; Wood, E. C.; Middlebrook, A. M.; Kolb, C. E.; Baltensperger, U.; Worsnop, D. R.; Dunlea, E. J.; Huffman, J. A.; Onasch, T. B.; Alfarra, M. R.; Williams, P. I.; Bower, K.; Kondo, Y.; Schneider, J.; Drewnick, F.; Borrmann, S.; Weimer, S.; Demerjian, K.; Salcedo, D.; Cottrell, L.; Griffin, R.; Takami, A.; Miyoshi, T.; Hatakeyama, S.; Shimono, A.; Sun, J. Y.; Zhang, Y. M.; Dzepina, K.; Kimmel, J. R.; Sueper, D.; Jayne, J. T.; Herndon, S. C.; Trimborn, A. M.; Williams, L. R.; Wood, E. C.; Middlebrook, A. M.; Kolb, C. E.; Baltensperger, U.; Worsnop, D. R. *Science* **2009**, *326* (5959), 1525–1529.
- (8) Pathak, R. K.; Stanier, C. O.; Donahue, N. M.; Pandis, S. N. *J. Geophys. Res. Atmos.* **2007**, *112*, D03201.
- (9) Ehn, M.; Kleist, E.; Junninen, H.; Petäjä, T.; Lönn, G.; Schobesberger, S.; Dal Maso, M.; Trimborn, A.; Kulmala, M.; Worsnop, D. R.; Wahner, A.; Wildt, J.; Mentel, T. F. *Atmos. Chem. Phys.* **2012**, *12* (11), 5113–5127.

- (10) Kulmala, M.; Kontkanen, J.; Junninen, H.; Lehtipalo, K.; Manninen, H. E.; Nieminen, T.; Petäjä, T.; Sipilä, M.; Schobesberger, S.; Rantala, P.; Franchin, A.; Jokinen, T.; Järvinen, E.; Äijälä, M.; Kangasluoma, J.; Hakala, J.; Aalto, P. P.; Paasonen, P.; Mikkilä, J.; Vanhanen, J.; Aalto, J.; Hakola, H.; Makkonen, U.; Ruuskanen, T.; III, R. L. M.; Duplissy, J.; Vehkamäki, H.; Bäck, J.; Kortelainen, A.; Riipinen, I.; Kurtén, T.; Johnston, M. V.; Smith, J. N.; Ehn, M.; Mentel, T. F.; Lehtinen, K. E. J.; Laaksonen, A.; Kerminen, V.-M.; Worsnop, D. R. *Science* **2013**, *339* (6122), 943–947.
- (11) Paasonen, P.; Asmi, A.; Petäjä, T.; Kajos, M. K.; Äijälä, M.; Junninen, H.; Holst, T.; Abbatt, J. P. D.; Arneth, A.; Birmili, W.; Van Der Gon, H. D.; Hamed, A.; Hoffer, A.; Laakso, L.; Laaksonen, A.; Richard Leitch, W.; Plass-Dülmer, C.; Pryor, S. C.; Räisänen, P.; Swietlicki, E.; Wiedensohler, A.; Worsnop, D. R.; Kerminen, V. M.; Kulmala, M. *Nat. Geosci.* **2013**, *6* (6), 438–442.
- (12) Riipinen, I.; Pierce, J. R.; Yli-Juuti, T.; Nieminen, T.; Häkkinen, S.; Ehn, M.; Junninen, H.; Lehtipalo, K.; Petäjä, T.; Slowik, J.; Chang, R.; Shantz, N. C.; Abbatt, J.; Leitch, W. R.; Kerminen, V. M.; Worsnop, D. R.; Pandis, S. N.; Donahue, N. M.; Kulmala, M. *Atmos. Chem. Phys.* **2011**, *11* (8), 3865–3878.
- (13) Ehn, M.; Thornton, J. A.; Kleist, E.; Sipilä, M.; Junninen, H.; Pullinen, I.; Springer, M.; Rubach, F.; Tillmann, R.; Lee, B.; Lopez-Hilfiker, F.; Andres, S.; Acir, I. H.; Rissanen, M.; Jokinen, T.; Schobesberger, S.; Kangasluoma, J.; Kontkanen, J.; Nieminen, T.; Kurtén, T.; Nielsen, L. B.; Jørgensen, S.; Kjaergaard, H. G.; Canagaratna, M.; Maso, M. D.; Berndt, T.; Petäjä, T.; Wahner, A.; Kerminen, V. M.; Kulmala, M.; Worsnop, D. R.; Wildt, J.; Mentel, T. F. *Nature* **2014**, *506* (7489), 476–479.
- (14) Jokinen, T.; Berndt, T.; Makkonen, R.; Kerminen, V. M.; Junninen, H.; Paasonen, P.; Stratmann, F.; Herrmann, H.; Guenther, A. B.; Worsnop, D. R.; Kulmala, M.; Ehn, M.; Sipilä, M. *Proc. Natl. Acad. Sci.* **2015**, *112* (23), 7123–7128.
- (15) Rissanen, M. P.; Kurtén, T.; Sipilä, M.; Thornton, J. A.; Kangasluoma, J.; Sarnela, N.; Junninen, H.; Jørgensen, S.; Schallhart, S.; Kajos, M. K.; Taipale, R.; Springer, M.; Mentel, T. F.; Ruuskanen, T.; Petäjä, T.; Worsnop, D. R.; Kjaergaard, H. G.; Ehn, M. *J. Am. Chem. Soc.* **2014**, *136* (44), 15596–15606.
- (16) Crouse, J. D.; Nielsen, L. B.; Jørgensen, S.; Kjaergaard, H. G.; Wennberg, P. O. *J. Phys. Chem. Lett.* **2013**, *4* (20), 3513–3520.

- (17) Riccobono, F.; Schobesberger, S.; Scott, C. E.; Dommen, J.; Ortega, I. K.; Rondo, L.; Almeida, J.; Amorim, A.; Bianchi, F.; Breitenlechner, M.; David, A.; Downard, A.; Dunne, E. M.; Duplissy, J.; Ehrhart, S.; Flagan, R. C.; Franchin, A.; Hansel, A.; Junninen, H.; Kajos, M.; Keskinen, H.; Kupc, A.; Kurten, A.; Kvashin, A. N.; Laaksonen, A.; Lehtipalo, K.; Makhmutov, V.; Mathot, S.; Nieminen, T.; Onnela, A.; Petaja, T.; Praplan, A. P.; Santos, F. D.; Schallhart, S.; Seinfeld, J. H.; Sipila, M.; Spracklen, D. V.; Stozhkov, Y.; Stratmann, F.; Tome, A.; Tsagkogeorgas, G.; Vaattovaara, P.; Viisanen, Y.; Virtala, A.; Wagner, P. E.; Weingartner, E.; Wex, H.; Wimmer, D.; Carslaw, K. S.; Curtius, J.; Donahue, N. M.; Kirkby, J.; Kulmala, M.; Worsnop, D. R.; Baltensperger, U.; Kürten, A.; Kvashin, A. N.; Laaksonen, A.; Lehtipalo, K.; Makhmutov, V.; Mathot, S.; Nieminen, T.; Onnela, A.; Petäjä, T.; Praplan, A. P.; Santos, F. D.; Schallhart, S.; Seinfeld, J. H.; Sipilä, M.; Spracklen, D. V.; Stozhkov, Y.; Stratmann, F.; Tomé, A.; Tsagkogeorgas, G.; Vaattovaara, P.; Viisanen, Y.; Virtala, A.; Wagner, P. E.; Weingartner, E.; Wex, H.; Wimmer, D.; Carslaw, K. S.; Curtius, J.; Donahue, N. M.; Kirkby, J.; Kulmala, M.; Worsnop, D. R.; Baltensperger, U. *Science* **2014**, *344* (6185), 717–721.
- (18) Tröstl, J.; Chuang, W. K.; Gordon, H.; Heinritzi, M.; Yan, C.; Molteni, U.; Ahlm, L.; Frege, C.; Bianchi, F.; Wagner, R.; Simon, M.; Lehtipalo, K.; Williamson, C.; Craven, J. S.; Duplissy, J.; Adamov, A.; Almeida, J.; Bernhammer, A. K.; Breitenlechner, M.; Brilke, S.; Dias, A.; Ehrhart, S.; Flagan, R. C.; Franchin, A.; Fuchs, C.; Guida, R.; Gysel, M.; Hansel, A.; Hoyle, C. R.; Jokinen, T.; Junninen, H.; Kangasluoma, J.; Keskinen, H.; Kim, J.; Krapf, M.; Kürten, A.; Laaksonen, A.; Lawler, M.; Leiminger, M.; Mathot, S.; Möhler, O.; Nieminen, T.; Onnela, A.; Petäjä, T.; Piel, F. M.; Miettinen, P.; Rissanen, M. P.; Rondo, L.; Sarnela, N.; Schobesberger, S.; Sengupta, K.; Sipilä, M.; Smith, J. N.; Steiner, G.; Tomé, A.; Virtanen, A.; Wagner, A. C.; Weingartner, E.; Wimmer, D.; Winkler, P. M.; Ye, P.; Carslaw, K. S.; Curtius, J.; Dommen, J.; Kirkby, J.; Kulmala, M.; Riipinen, I.; Worsnop, D. R.; Donahue, N. M.; Baltensperger, U. *Nature* **2016**, *533* (7604), 527–531.
- (19) Donahue, N. M.; Epstein, S. A.; Pandis, S. N.; Robinson, A. L. *Atmos. Chem. Phys.* **2011**, *11* (7), 3303–3318.

- (20) Kirkby, J.; Duplissy, J.; Sengupta, K.; Frege, C.; Gordon, H.; Williamson, C.; Heinritzi, M.; Simon, M.; Yan, C.; Almeida, J.; Trostl, J.; Nieminen, T.; Ortega, I. K.; Wagner, R.; Adamov, A.; Amorim, A.; Bernhammer, A. K.; Bianchi, F.; Breitenlechner, M.; Brilke, S.; Chen, X.; Craven, J.; Dias, A.; Ehrhart, S.; Flagan, R. C.; Franchin, A.; Fuchs, C.; Guida, R.; Hakala, J.; Hoyle, C. R.; Jokinen, T.; Junninen, H.; Kangasluoma, J.; Kim, J.; Krapf, M.; Kurten, A.; Laaksonen, A.; Lehtipalo, K.; Makhmutov, V.; Mathot, S.; Molteni, U.; Onnela, A.; Perakyla, O.; Piel, F.; Petaja, T.; Praplan, A. P.; Pringle, K.; Rap, A.; Richards, N. A. D.; Riipinen, I.; Rissanen, M. P.; Rondo, L.; Sarnela, N.; Schobesberger, S.; Scott, C. E.; Seinfeld, J. H.; Sipila, M.; Steiner, G.; Stozhkov, Y.; Stratmann, F.; Tomé, A.; Virtanen, A.; Vogel, A. L.; Wagner, A. C.; Wagner, P. E.; Weingartner, E.; Wimmer, D.; Winkler, P. M.; Ye, P.; Zhang, X.; Hansel, A.; Dommen, J.; Donahue, N. M.; Worsnop, D. R.; Baltensperger, U.; Kulmala, M.; Carslaw, K. S.; Curtius, J. *Nature* **2016**, *533* (7604), 521–526.
- (21) Sarnela, N.; Jokinen, T.; Duplissy, J.; Yan, C.; Nieminen, T.; Ehn, M.; Schobesberger, S.; Heinritzi, M.; Ehrhart, S.; Lehtipalo, K.; Tröstl, J.; Simon, M.; Kürten, A.; Leiminger, M.; Lawler, M. J.; Rissanen, M. P.; Bianchi, F.; Praplan, A. P.; Hakala, J.; Amorim, A.; Gonin, M.; Hansel, A.; Kirkby, J.; Dommen, J.; Curtius, J.; Smith, J. N.; Petäjä, T.; Worsnop, D. R.; Kulmala, M.; Donahue, N. M.; Sipilä, M. *Atmos. Chem. Phys.* **2018**, *18* (4), 2363–2380.
- (22) Apsokardu, M. J.; Johnston, M. V. *Atmos. Chem. Phys.* **2018**, *18*, 1895–1907.
- (23) Huang, Y.; Coggon, M. M.; Zhao, R.; Lignell, H.; Bauer, M. U.; Flagan, R. C.; Seinfeld, J. H. *Atmos. Meas. Tech.* **2017**, *10* (3), 839–867.
- (24) Ciobanu, V. G.; Marcolli, C.; Krieger, U. K.; Zuend, A.; Peter, T. *J. Phys. Chem. A* **2010**, *114*, 9486–9495.
- (25) Sarnela, N.; Jokinen, T.; Duplissy, J.; Yan, C.; Nieminen, T.; Ehn, M.; Schobesberger, S.; Heinritzi, M.; Ehrhart, S.; Lehtipalo, K.; Tröstl, J.; Simon, M.; Kürten, A.; Leiminger, M.; Lawler, M. J.; Rissanen, M. P.; Bianchi, F.; Praplan, A. P.; Hakala, J.; Amorim, A.; Gonin, M.; Hansel, A.; Kirkby, J.; Dommen, J.; Curtius, J.; Smith, J. N.; Petäjä, T.; Worsnop, D. R.; Kulmala, M.; Donahue, N. M.; Sipilä, M. *Atmos. Chem. Phys.* **2018**, *18* (4), 2363–2380.
- (26) Calvert, J. G. *The Mechanisms of Atmospheric Oxidation of the Alkenes*; Oxford University Press: Oxford, New York, 2008.
- (27) Tu, P.; Hall, W. A.; Johnston, M. V. *Anal. Chem.* **2016**, *88* (8), 4495–4501.
- (28) Khamaganov, V. G.; Hites, R. A. *J. Phys. Chem. A* **2001**, *105* (5), 815–822.

- (29) Hanson, D. R.; Eisele, F. J. *J. Phys. Chem. A* **2000**, *104* (8), 1715–1719.
- (30) Knopf, D. A.; Pöschl, U.; Shiraiwa, M. *Anal. Chem.* **2015**, *87* (7), 3746–3754.
- (31) Dal Maso, M.; Kulmala, M.; Lehtinen, K. E. J.; Mäkelä, J. M.; Aalto, P.; O'Dowd, C. D. *J. Geophys. Res. Atmos.* **2002**, *107* (D19), PAR-2.
- (32) Ezhova, E.; Kerminen, V. M.; Lehtinen, K. E. J.; Kulmala, M. *Atmos. Chem. Phys.* **2018**, *18* (4), 2431–2442.
- (33) Kuwata, M.; Martin, S. T. *Aerosol Sci. Technol.* **2012**, *46* (8), 937–949.
- (34) Krapf, M.; El Haddad, I.; Bruns, E. A.; Molteni, U.; Daellenbach, K. R.; Prévôt, A. S. H.; Baltensperger, U.; Dommen, J. *Chem* **2016**, *1* (4), 603–616.
- (35) Zhang, X.; Lambe, A. T.; Upshur, M. A.; Brooks, W. A.; Gray Bé, A.; Thomson, R. J.; Geiger, F. M.; Surratt, J. D.; Zhang, Z.; Gold, A.; Graf, S.; Cubison, M. J.; Groessl, M.; Jayne, J. T.; Worsnop, D. R.; Canagaratna, M. R. *Environ. Sci. Technol.* **2017**, *51* (11), 5932–5940.
- (36) Mutzel, A.; Poulain, L.; Berndt, T.; Iinuma, Y.; Rodigast, M.; Böge, O.; Richters, S.; Spindler, G.; Sipilä, M.; Jokinen, T.; Kulmala, M.; Herrmann, H. *Environ. Sci. Technol.* **2015**, *49* (13), 7754–7761.
- (37) Shiraiwa, M.; Berkemeier, T.; Schilling-Fahnestock, K. A.; Seinfeld, J. H.; Pöschl, U. *Atmos. Chem. Phys.* **2014**, *14* (16), 8323–8341.
- (38) Berndt, T.; Jokinen, T.; Sipilä, M.; Mauldin, R. L.; Herrmann, H.; Stratmann, F.; Junninen, H.; Kulmala, M. *Atmos. Environ.* **2014**, *89*, 603–612.
- (39) Newland, M. J.; Rickard, A. R.; Sherwen, T.; Evans, M. J.; Vereecken, L.; Muñoz, A.; Ródenas, M.; Bloss, W. J. *Atmos. Chem. Phys.* **2018**, *18* (8), 6095–6120.

## Chapter 4

### EFFECT OF REALTIVE HUMIDITY ON AITKEN MODE PARTICLE GROWTH

#### 4.1 Growth of Particles Under High Relative Humidity Conditions

Aitken mode particles (10-100 nm in diameter) represent the largest number fraction of particles found in the ambient environment <sup>1</sup>. Understanding the processes contributing to the growth of these particles is paramount to better predict formation of cloud condensation nuclei (CCN) <sup>2-4</sup>. Organic molecules formed through gas phase oxidation of organic precursors such as  $\alpha$ -pinene with low volatility have been shown to contribute to particle growth in this size range <sup>5-8</sup>. Auto-oxidation involving the addition of multiple O<sub>2</sub> molecules per precursor molecule is thought to produce highly oxidized molecules (HOMs) which grow nanoparticles by condensation limited processes <sup>9-11</sup>. Though there is some ambiguity in the literature, HOMs were originally defined as gas phase products of precursor oxidation that are detected by NO<sub>3</sub><sup>-</sup> chemical ionization mass spectrometry, though many authors have subsequently used the term to represent all molecules that condensationally grow particles. This definition makes HOM synonymous with the more general term that we use in our work, nonvolatile organic compounds (NVOCs), which includes the possibility that some of the molecules growing particles at the condensation rate are not detected by chemical ionization. In this regard, HOMs are only a subset of total NVOC.

New particle formation (NPF) events are less frequently observed under high relative humidity (RH) conditions making it difficult to study ambient particle growth

under these conditions<sup>12-15</sup>. Li et al. (2019)<sup>16</sup> have studied the effect RH has on gas-phase HOM formation using chemical ionization mass spectrometry. This work showed that HOM formation occurs through a pathway that is independent of RH, indicating that this pathway does not go through stabilized Criegee Intermediates (sCIs) that are able to react with water, and suggests that particle growth should be independent of RH. However, Faust et al. (2017)<sup>17</sup> have shown that liquid-like particles at high RH give higher secondary organic aerosol (SOA) mass yields than dry particles at low RH. Taken together, these two studies suggest the potential for particle-phase chemistry to occur in the liquid-like particles, which opens up an additional growth mechanism independent of NVOC condensation. Specifically, Faust et al. (2017)<sup>17</sup> report a significant enhancement in the SOA produced from oxidation of  $\alpha$ -pinene, toluene and acetylene when aerosol liquid water (ALW) is present. Three main processes were advanced as possible sources of the enhancement. First, the increased ability of hydrophilic molecules to dissolve in aqueous particles caused a decrease in the Henry's Law constant when compared to dry solid particles. Second, particle-phase reactions could irreversibly drive uptake of SVOCs by formation of nonvolatile products. And third, phase separation may have created interfaces for different reactions to potentially occur. Understanding these different processes is necessary to better understand the role that ALW plays in particle growth.

Phase separation has become an important area of study as it can have large effects on the growth of particles as discussed earlier. The size dependence of phase separation has been discussed<sup>18-20</sup> and interestingly has been found to occur with increasing frequency as the particle size increases above about 50 nm, while smaller

particles are generally homogeneous. This possibility is especially applicable to the work presented here and will be further discussed in section 4.4.

Recently we have shown that NVOCs produced by  $\alpha$ -pinene oxidation under dry conditions can grow dry ammonium sulfate seed particles<sup>21,22</sup>. This growth and its seed particle size dependence were explained using a condensation growth model with a yield of 13%. While Li et al. (2019)<sup>16</sup> have shown that gas-phase HOMs do not change with RH, here we work to see the effect of RH and ALW on the corresponding particle growth to elucidate potential growth mechanisms occurring in the particle-phase. This is done by measuring the growth of size-selected ammonium sulfate seed particles by  $\alpha$ -pinene ozonolysis under three different reactor conditions: solid seed particles at an RH below efflorescence (RH = 10%), solid seed particles at an RH between efflorescence and deliquescence (RH = 60%), and liquid-like seeds at an RH between efflorescence and deliquescence (RH 60%). The results show a clear enhancement in growth of seed particles containing ALW, and the effect is greatest for those with initial (dry) diameters less than or equal to 40 nm. As discussed later in this chapter, modeling growth as a function of particle seed diameter allows us to fit the observed growth enhancement to a condensational growth model with a modified yield of condensable molecules.

## **4.2 Experimental Modifications For High Relative Humidity Experiments**

This work utilizes a flow tube reactor shown in Figure 4-1 that has previously been described<sup>21-23</sup>. Briefly, the flow tube is constructed using a quartz tube with stainless steel funnels on either end and is operated under conditions where the residence time is reproducibly on the order of 4 minutes. There are two inlet flows. Flow A contains size selected ammonium sulfate seed particles, ozone, make-up air

and water vapor when needed. Flow B contains the organic precursor,  $\alpha$ -pinene is used in this work, and  $H_2$  which acts as an OH scavenger so that ozonolysis can be studied independently. Two changes to the previous experimental setups were necessary for these experiments. First, a water bubbler with a bypass needle valve was added to the make-up air flow allowing for fine adjustment of the RH within the reactor. For low RH experiments, the valve was completely open to bypass the bubbler. For higher RH experiments the valve can be adjusted so that the flow tube equilibrates to the desired value of 60% that was used in this work. Second, a condensation growth chamber (CGC, custom made by Aerosol Dynamics Inc., Berkeley CA) was added after the size selection differential mobility analyzer (DMA). The CGC was operated under similar conditions to those described in Horan, Apsokardu, and Johnston (2017)<sup>24</sup> to produce aqueous droplets from the solid particles. The CGC is made up of three regions, a cold conditioner region (5 °C) warm initiator region (45 °C) and cool moderator region (20 °C). The combination of these three regions along with a water saturated wick throughout creates a supersaturation of water vapor forcing condensation of water onto the particles as they pass through the instrument. This process creates the liquid-like particles to be sent into the flow tube allowing for studying the effect of ALW on particle growth. Figure 4-2 illustrates how both wet and dry seed particles can exist in the reactor at the same relative humidity. Dry particles will not pick up water at 60% RH because they never reach the deliquescence relative humidity (DRH) of 80%, whereas seeds that pass through the CGC never have water completely removed as they do not reach the efflorescence relative humidity (ERH) of 30%.<sup>25</sup>

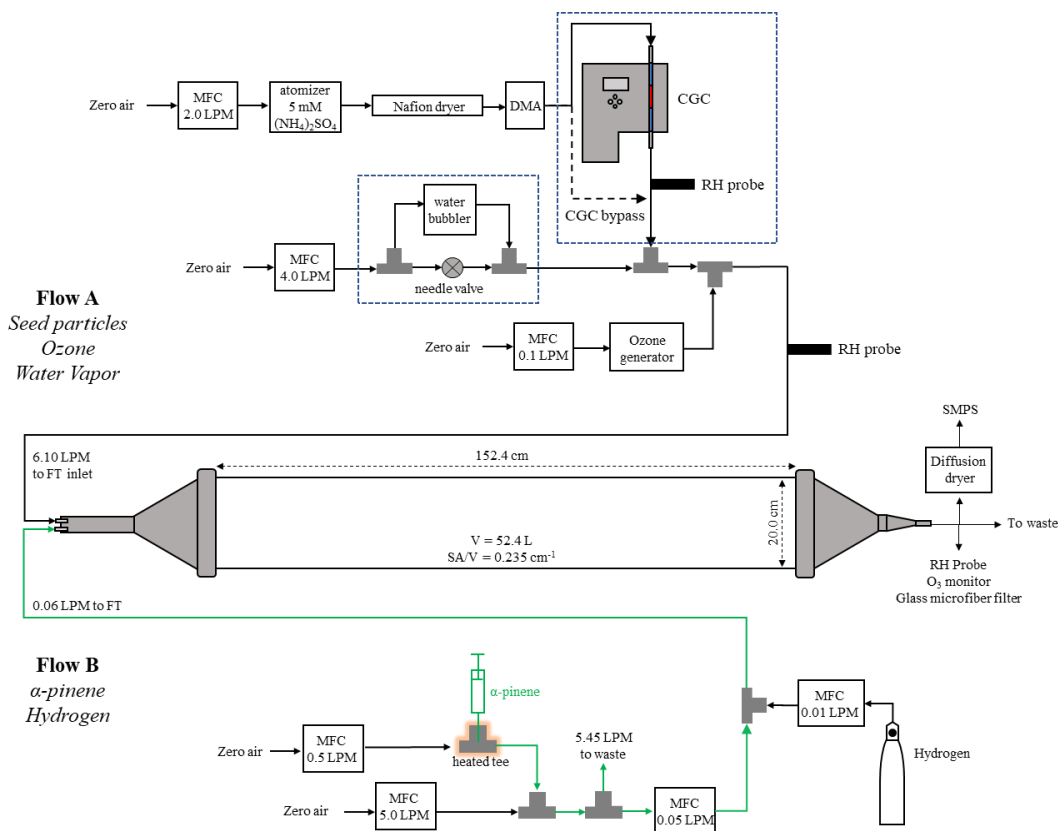


Figure 4-1. Experimental setup for high relative humidity experiments.

Experiments described here were performed like those described in Krasnomowitz et al. (2019)<sup>21</sup> where the flow tube is first allowed to equilibrate in terms of particle number concentration, RH and ozone mixing ratio. Once stable conditions are achieved, monoterpene injection begins and corresponding growth by the  $\alpha$ -pinene ozonolysis products is measured using a scanning mobility particle sizer (SMPS, TSI inc., Shoreview MN). Unless otherwise noted, diffusion dryer tubes were placed before the SMPS to remove any ALW from the particles so that only the dry diameter was measured. The RH was lowered to <20 % for all dry measurements with the SMPS as no further change in the distribution was observed at lower RH. Once

the measured size distribution has stabilized and sufficient data has been collected ozone concentration is incremented (values range from 25-250 ppbv) to produce more ozonolysis products resulting in more particle growth. This process is repeated for five ozone concentrations and data is continuously collected by SMPS, Ozone monitor (49i, Thermo Fischer Scientific Inc., Waltham, MA) and RH probe (Traceable, Thermo Fischer Scientific Inc.).

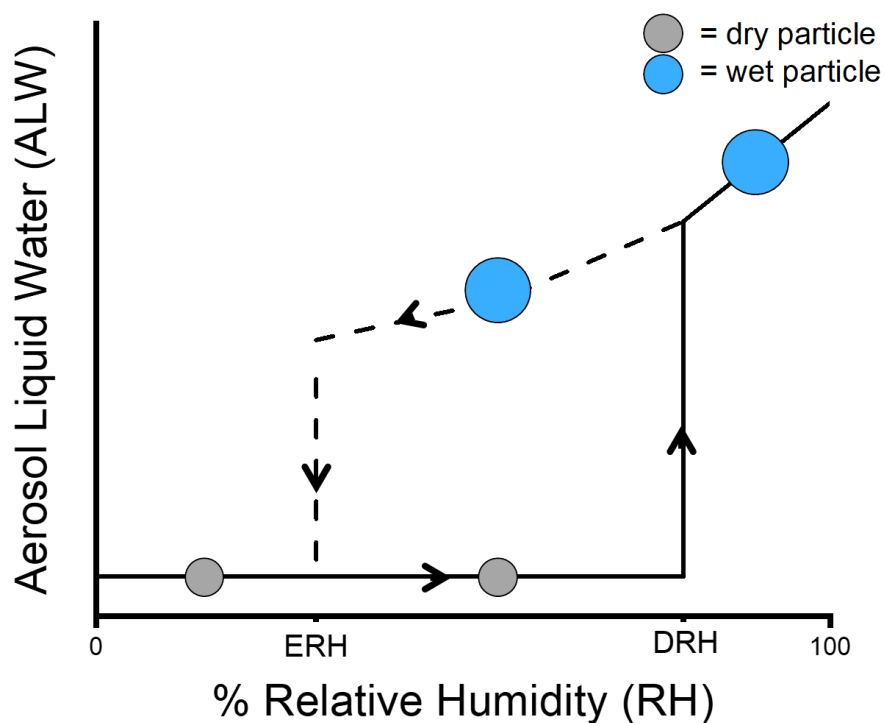


Figure 4-2. Explanation of efflorescence and deliquescence of ammonium sulfate seed particles. ERH denotes the efflorescence relative humidity and DRH denotes the deliquescence relative humidity.

We can confirm that water is being added to the particles by passing them through the CGC by removing the diffusion dryers before the SMPS to measure the wet size distribution. Average wet and dry size distributions for 40 nm (dry) seed particles selected by the DMA are shown in Figure 4-3 for both the seeds without being exposed to oxidation products and after being exposed to the highest ozone mixing ratio used in growth experiments. While the flow tube was being held at a relative humidity of 60% during these measurements, the SMPS during the wet measurement equilibrated only to an RH of 45%. This resulted in a median diameter of 49 nm, increased from the size selected median diameter of 41 nm. The increase from water was also calculated using E-AIM<sup>26-28</sup> and a similar diameter increase was calculated with a 40 nm dry particle increasing to 49 nm aqueous particle at 45% RH. E-AIM predicts an even larger increase to 53 nm when the RH is increased to 60%. These calculations confirm that the amount of water measured by the SMPS is consistent with thermodynamics. However, the difference in RH between the flow tube (65%) and SMPS (45%) for the undried aerosol means that the measured size distribution of wet particles does not accurately describe the condensation sink and particle growth in the flow tube. For this reason, all subsequent size distributions in this chapter are reported for dried aerosol, with the ALW content calculated from the measured RH in the flow tube.

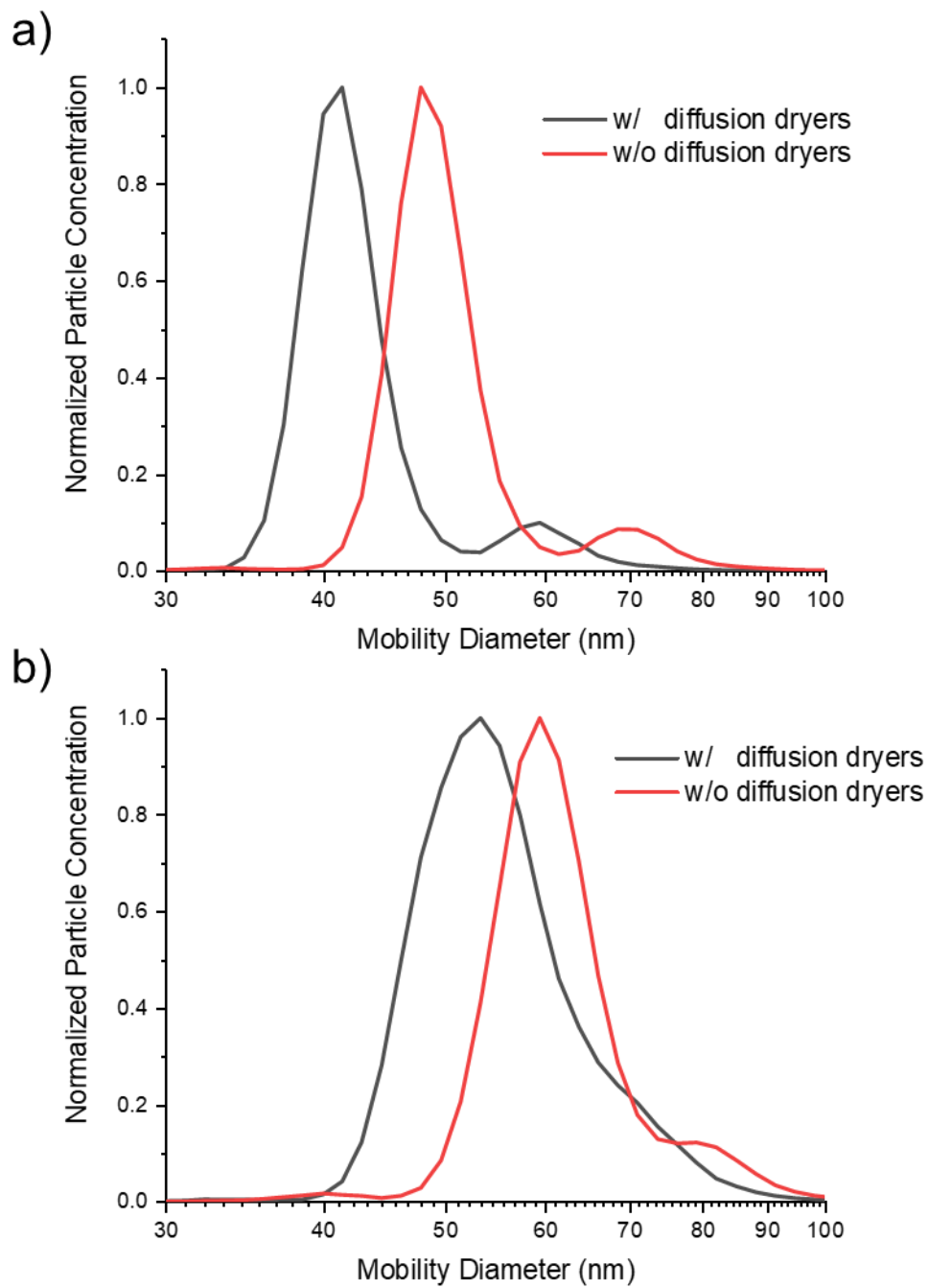


Figure 4-3. Measured change in diameter of a) seeds and b) seeds exposed to ~200 ppbv ozone caused by the removal of diffusion dryer tubes before measurement SMPS allowing for measurement of wet particles

### 4.3 Experimental Measurements of Particle Growth

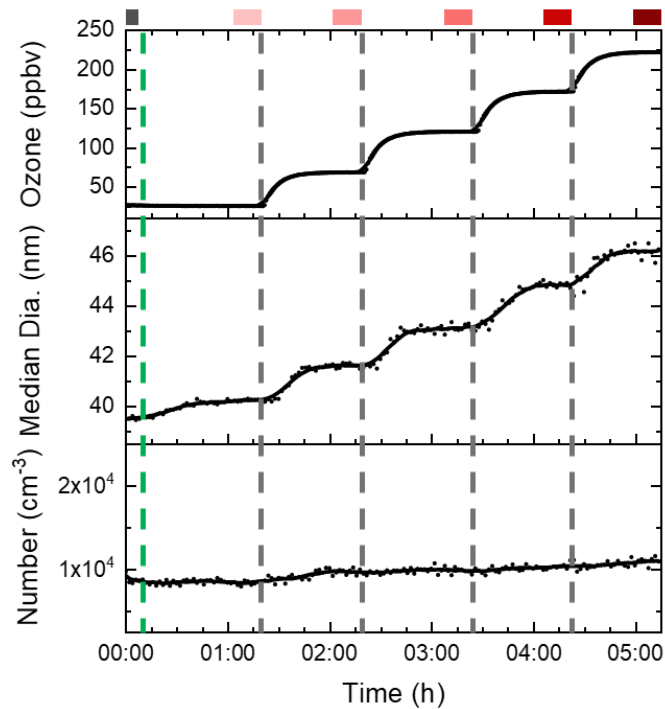


Figure 4-4. Time series over a typical growth experiment. Green line represents when  $\alpha$ -pinene was started with subsequent gray lines representing an increase in ozone concentration. Solid bars at the top represent time period over which data was averaged for analysis. Measured ozone mixing ratio, median diameter and number concentration of the distribution exiting the flow over time are shown. The  $\alpha$ -pinene mixing ratio was 11 ppbv.

Size distributions of particles exiting the flow tube were continuously measured over the course of an experiment. A typical experiment is shown in Figure 4-4 which shows the ozone concentration, dry median diameter and number concentration over the course of the experiment. After  $\alpha$ -pinene injection begins (11

ppbv mixing ratio in the flow tube, similar to the experiments in Chapter 3), each increase in the ozone mixing ratio shifts the size distribution from the initial seed particle distribution to successively larger particle sizes, as can be seen by the corresponding increase in median diameter with increasing ozone mixing ratio. The number concentration remains relatively constant throughout the experiment, confirming that little nucleation occurs. Particle growth is also shown in Figure 4-5a by the average size distributions at each increment in ozone mixing ratio, the colored bars in Figure 4-4 represent the time period over which the size distributions are averaged. Each measured shift to larger diameter is a measurement of the growth caused by exposing the seed particles to the oxidation products formed in the flow tube.

Growth experiments were done under three different conditions: dry particles at low RH (10%), dry particles at high RH (60%) and wet particles at high RH (60%). Average size distributions from the three conditions for 40 nm seed particles are shown in Figure 4-5a-c. Comparing the size distributions, it is clear the seed particles that contain ALW (Figure 4-5c) show larger diameter changes than the dry seed particles (Figure 4-5a and b). This is not due to water remaining on the particles during measurement as the particles are dried below efflorescence (<20% RH) before the SMPS measurement, indicating a growth enhancement when ALW is present.

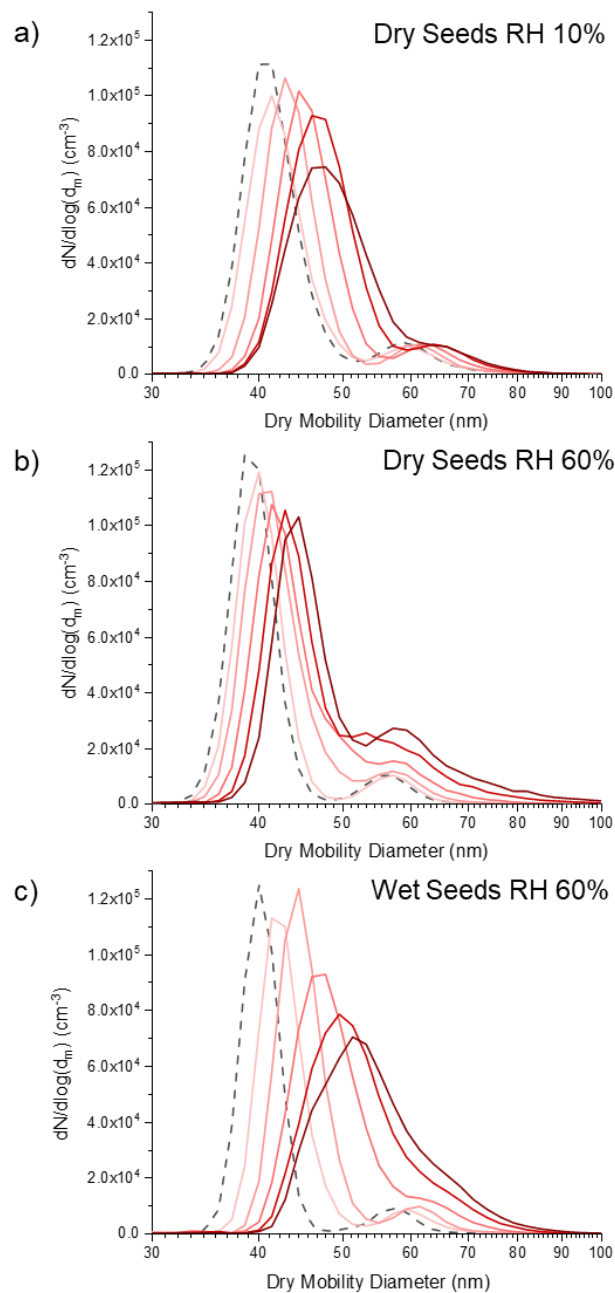


Figure 4-5. Particle growth of size-selected 40 nm particles after exposure to increasing ozone mixing ratio with constant  $\alpha$ -pinene (11 ppbv) under different RH conditions: a) shows dry seed particles at an RH of 10% b) shows dry seed particles at an RH of 60% and c) shows seeds with ALW at an RH of 60%.

Data similar to Figure 4-5 were obtained for a total of five seed particle diameters: 30, 40, 50, 60 and 80 nm. These results are shown for 40 and 60 nm (dry) diameter seed particles in Figure 4-6 and 30, 50 and 80 nm (dry) diameter seed particles in Figure 4-7. Taking the 40 nm diameter data in Figure 4-6a as an example, the median diameter for each of the size distributions in Figure 4-5 was determined, and then the difference in median diameter after vs. before exposure to  $\alpha$ -pinene ozonolysis was plotted as a function of ozone mixing ratio. Overall, a linear relationship is observed between the change in median diameter and the ozone mixing ratio. This linearity, which is observed in all plots in Figures 4-6 and 4-7, is consistent with previous work published by our group, Krasnomowitz et al. (2019)<sup>21</sup> and Stangl et al. (2019)<sup>22</sup>, and as discussed in Chapter 1.6 suggests that the results obtained with above-ambient mixing ratios in these experiments are relevant to ambient conditions.

A common feature of all plots in Figures 4-6 and 4-7 is the similar growth of dry seed particles at 10% and 60% RH. Similar growth independent of relative humidity is expected as HOM production has recently been shown to be independent of RH<sup>16</sup>. As discussed in Chapter 1.5, HOM oxidation is thought to occur by a pathway that is unaffected by the reaction of water vapor with the stabilized Criegee Intermediate (sCI). Therefore, the mixing ratios of HOMs in the gas phase are the same for both relative humidities studied, resulting in the same amount of seed particle growth in the flow tube. Figure 4-8 summarizes the three main reaction channels for  $\alpha$ -pinene ozonolysis. Only the pathway highlighted in blue relies on water, which results in the formation of semivolatile products such as pinonaldehyde. It is likely that even at 10% RH, there is enough water vapor present to saturate this reaction pathway, meaning that the reaction rate of the blue pathway proceeds as fast as it can

and increasing the water mixing ratio (i.e. RH) does not lead to any additional formation of blue pathway products.

When comparing dry seed particle growth to the experiment where aerosol liquid water (ALW) is present in the seeds, a significant enhancement is sometimes observed. For example, compare the dry and wet seed particle growth for 40 nm particles (Figure 4-6a) and 30 nm particles (Figure 4-7a). To confirm these results, an additional experiment was performed at the end of the ALW experiment (with the highest ozone mixing ratio) where the condensation growth chamber (CGC) was bypassed, thus removing ALW from the seed particles. The results of this experiment are shown by the star in Figures 4-6a and 4-7a. In each case, the diameter growth observed fell back to the value obtained previously in the dry particle experiments, confirming that ALW is involved with the observed growth enhancement.

While no difference in particle growth is observed for the other seed particle diameters (Figures 4-6b and 4-7b-c), it is incorrect to conclude that the growth of 50, 60 and 80 nm seed particles is unaffected by ALW. Figures 4-6 and 4-7 plotted on the basis of dry particle diameter. The actual seed particle diameters in the ALW experiments are larger than those in the dry experiments. Since particle size affects the condensation sink in the experiment and therefore the amount of growth observed, modeling must be done to interpret the results.

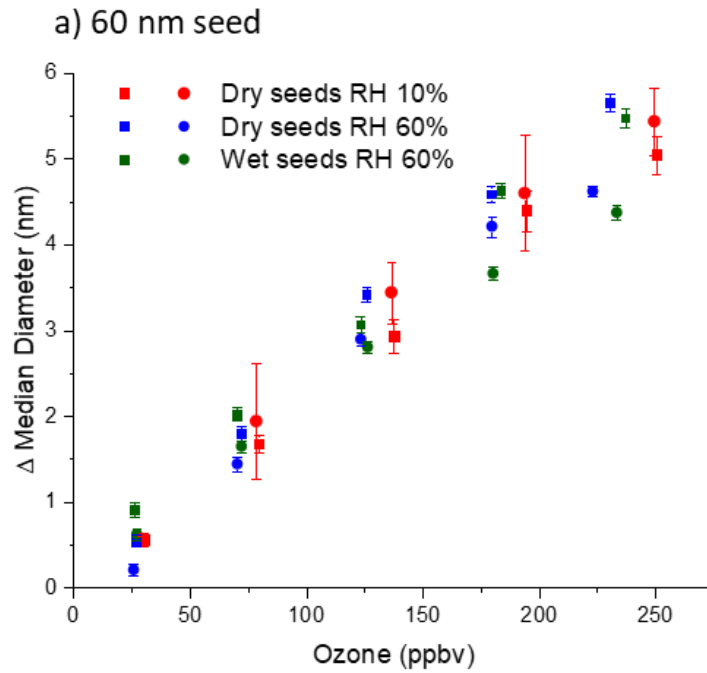
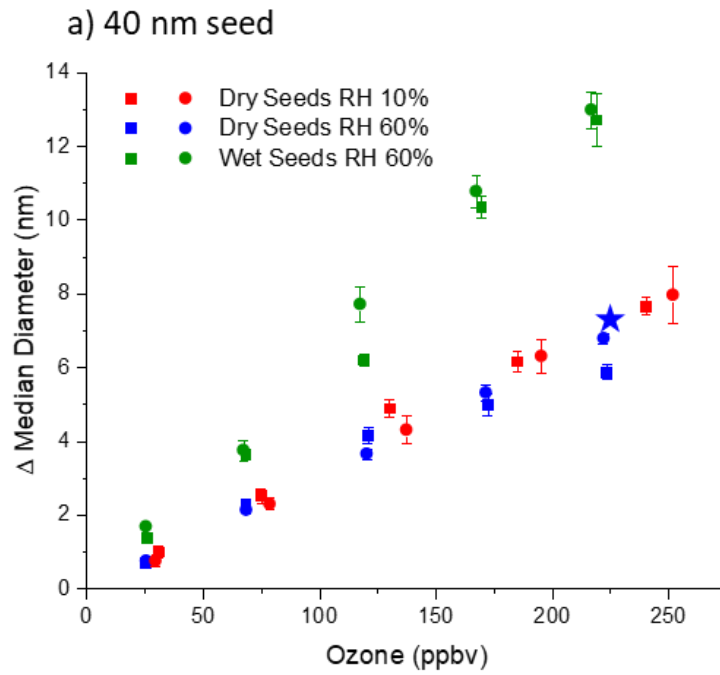


Figure 4-6. Particle growth data for a) 40 nm and b) 60 nm dry diameter ammonium sulfate seed particles. Each plot shows the change in median diameter of the (dry) particle size distribution exiting the flow tube as a function of ozone mixing ratio, for the three different RH conditions.

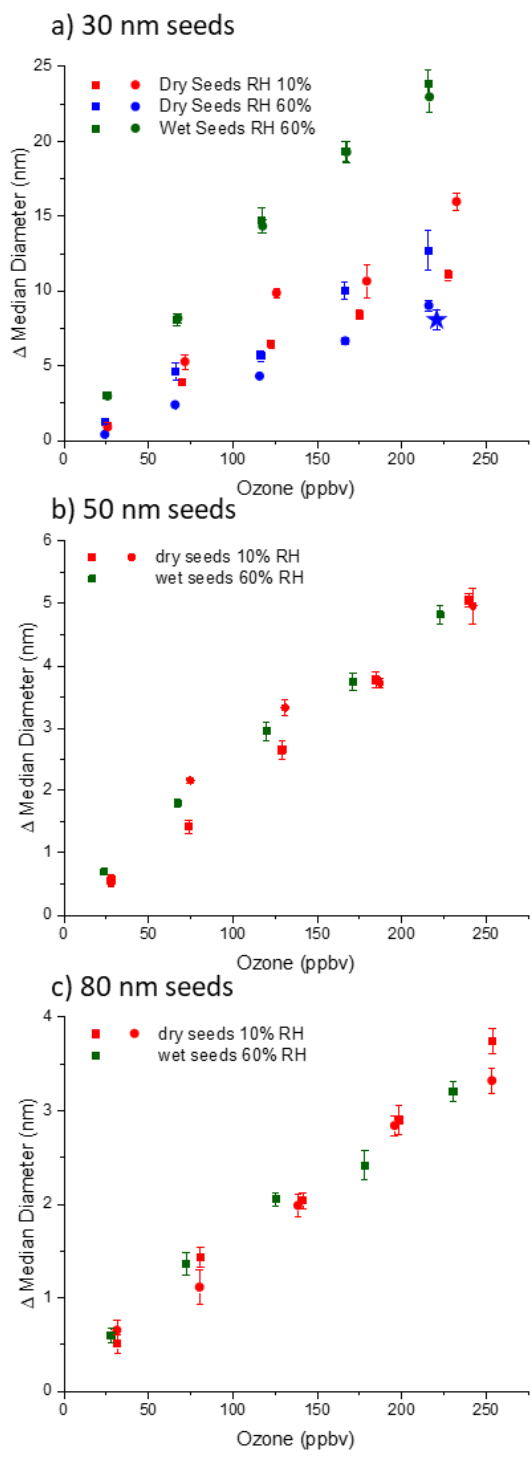


Figure 4-7. Particle growth data for a) 30, b) 50 and c) 80 nm dry ammonium sulfate seed particles.

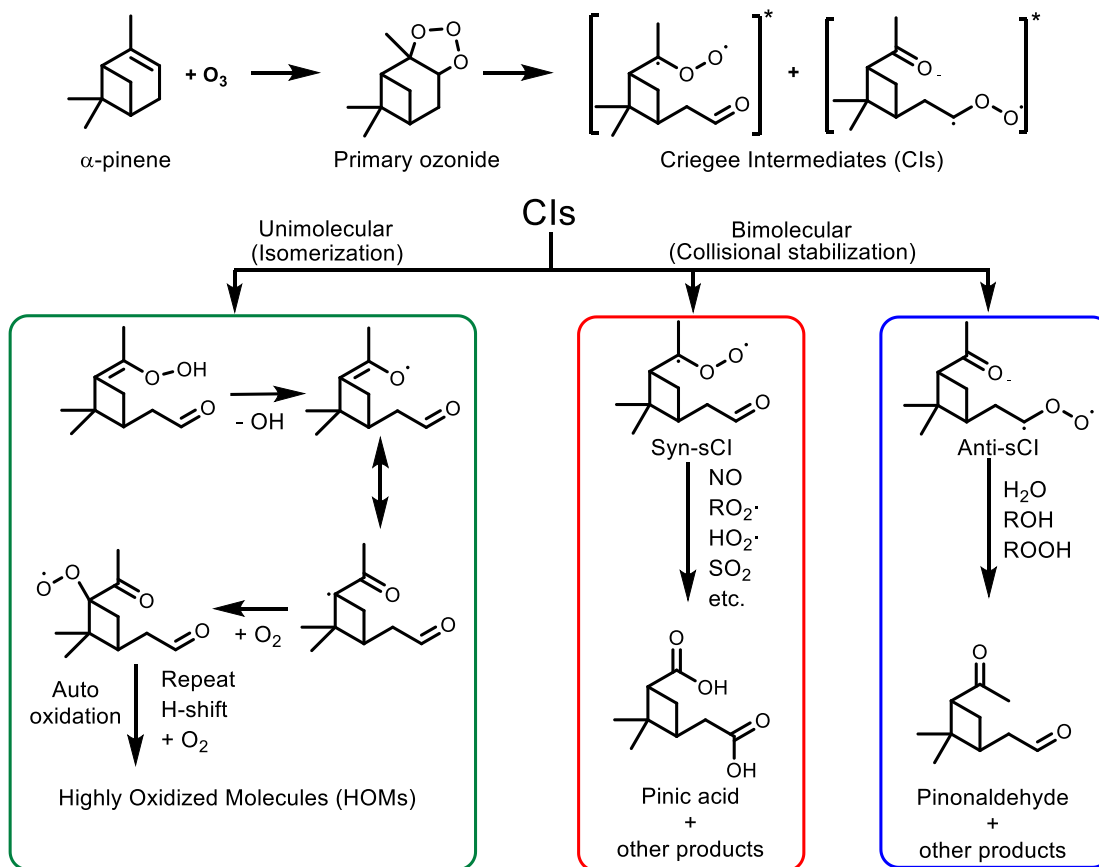


Figure 4-8. Simplified mechanism describing various pathways for gas-phase product formation from  $\alpha$ -pinene ozonolysis. HOM formation occurs by the green route, while water vapor only affects the blue route. This figure is the same as Figure 1-5 and is shown here for the convenience of the reader.

#### 4.4 Kinetic Modeling of Measured Growth Enhancement

Kinetic modeling of particle growth in the flow tube was done in a similar manner to that described in Chapter 3. Briefly, the gas-phase highly oxidized molecules (HOMs) are predicted as a function of time through the flow tube reactor. Multiple processes are accounted for in the modeling summarized in Equation 4-1.

$$(4-1) [HOM]_{t+\Delta t} = [HOM]_t + k_{II}[\alpha P]_t[O_3]_t y \Delta t - k_{WL}[HOM]_t \Delta t - k_{CS}[HOM]_t \Delta t$$

The model works by updating both reactant and product concentration every second over the residence time of the flow tube reactor with the following processes being accounted for: First, the second order reaction between ozone and  $\alpha$ -pinene is used to determine the amount of new HOMs formed over the time step. Second, wall loss of gas-phase HOMs is accounted for and any HOMs lost to the walls are assumed to be irreversibly lost. This accounts for one potential sink for the HOMs other than growing particles. Another sink for HOMs in the gas phase is condensation onto particles. This loss is also accounted for by calculating the condensation sink of the particles in the reactor. This results in time dependent HOM mixing ratios over the residence time of the flow tube similar to those shown in Figure 3-4. These HOM mixing ratios can then be used to calculate a resulting diameter change through the processes described in Apsokardu and Johnston (2018)<sup>29</sup>. In the model the only unknown value is the HOM yield for  $\alpha$ -pinene ozonolysis. As discussed in Chapter 3, the yield of condensable material under dry conditions was determined to be  $13\pm 1\%$  by simultaneously fitting the results of all seed particle diameter experiments. For the experiments described in this chapter, a slightly different approach was used. Here, the yield was determined independently for each seed particle diameter in each experiment. Comparing the yields obtained for different particle diameters in a given experiment, for example the different seed particle size experiments performed at 10% RH experiments, allows the assumption of a condensation growth model to be tested. A condensation growth model would be consistent with a yield that is independent of initial seed particle diameter. On the other hand, a different type of growth model would be indicated if the yield changes with particle diameter, or if the yield at a given seed particle size depends on RH and/or the presence of ALW.

As mentioned before, adding ALW to the seeds before introducing them into the flow tube substantially increases the particle diameter and thus the condensation sink (CS). A higher CS results in a greater loss of gas-phase molecules to the CS, lower mixing ratios of oxidation products in the gas phase, and therefore a smaller increase in particle diameter. The differences in CS in the various experiments complicates direct comparison of the results in Figures 4-6 and 4-7, since the amount of growth observed depends on CS. Furthermore, directly measuring the CS for the wet seed particles is difficult as the SMPS used at the end of the flow tube equilibrates to a lower relative humidity than the flow tube when all dryers are removed.

In order to get a best estimate of the CS for the wet seed experiments and determine the sensitivity of the modeling to the CS, three different calculations were done. First, the CS was determined experimentally by removing the diffusion dryer tubes in front of the SMPS. This allows the relative humidity of the SMPS to increase to a value more similar to that of the flow tube reactor. While the relative humidity of the SMPS did increase significantly and a size shift was measured confirming the presence of aerosol liquid water (e.g. Figure 4-3), the SMPS RH never completely matched that of the reactor stabilizing near 50% while the reactor was held at 60%. Therefore, the CS measured using this method represents the lower limit, and the lowest yield was calculated when using this approach.

Second the Extended-Aerosol Inorganic Model (E-AIM)<sup>27</sup> was used to model the particle volume at 60% RH when ALW was present. This was done by calculating particle volume of the dry seed particles to determine the amount of ammonium sulfate present. The SOA volume was calculated using the difference in dry volume before and after growth in the flow tube, with assumptions of molecular weight and

density of 132 g/mole and 1.43 g/mL respectively to determine moles/m<sup>3</sup> of SOA. E-AIM does not natively support SOA so a proxy must be used to model SOA. This was done by modeling various dicarboxylic acids to determine which agreed best with the SMPS measurements where the RH in the instrument was 50%. Glutaric acid was determined to have the best fit with the experimental data and was therefore used as a proxy. E-AIM simulations were then done assuming an RH of 60% and the increase in volume relative to that measured at 50% RH was apportioned to ALW. The wet particle diameter calculated by this method and used to determine the CS. The CS calculated this way simulates all components present in the particle and at the RH of the reactor causing the CS values and yields to be in between the other two situations studied.

Finally, another set of E-AIM simulations was performed this time assuming the entire particle was made up of ammonium sulfate. Due to the high hygroscopicity of ammonium sulfate these simulations result in the largest uptake in water and thus the largest CS, with the resulting yield representing an upper limit. The three situations discussed represent a sensitivity study to see the effect of condensation sink on the yield needed to explain the measured growth. A comparison of the condensation sink values calculated using the three methods is shown in Figure 4-9.

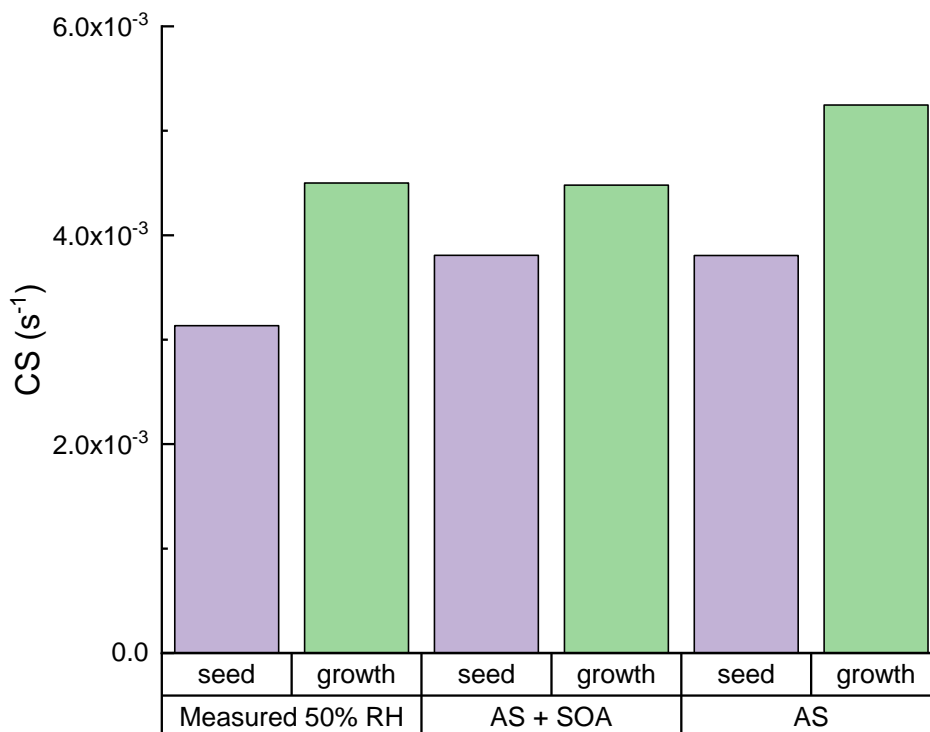


Figure 4-9. Condensation sink values determined by the three methods described in the text for ammonium sulfate seed particles with a dry diameter of 40 nm (purple) and the grown particles after exposure to 11 ppbv  $\alpha$ -pinene and 200 ppbv ozone in the flow tube (green). “Measured 50% RH” represents the lower limit calculation of the condensation sink. “AS” represents the upper limit calculation of the condensation sink. “AS+SOA” represents the best guess calculation of the condensation sink.

The calculated HOM yields for all seed particle diameters in the three experiments are shown in Figure 4-10. In this plot, the error bars for the wet seed particle experiment show the range of yields calculated based on lower and upper limits for the CS for each seed particle diameter. As expected, dry seed particles at

10% and 60% RH show the same HOM yield for all particle diameters studied. This result confirms a condensational growth mechanism where the yield is independent of RH. The wet particles show an enhanced yield for all particle diameters, with the greatest enhancements below 50 nm diameter (dry). The apparent yields for the wet particles do not indicate that the gas phase HOM yield is different from the dry particle experiments, but instead point to a different type of growth mechanism.

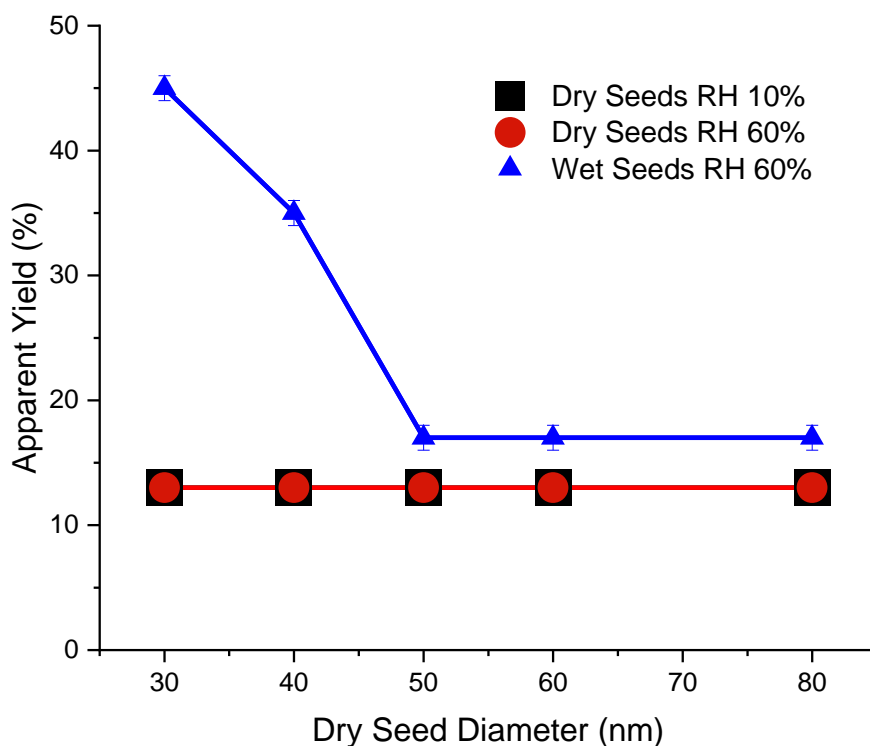


Figure 4-10. Determined percent yield of  $\alpha$ -pinene oxidation products that must contribute to growth to explain the measured change in particle diameter.

## 4.5 Particle Composition Measurements

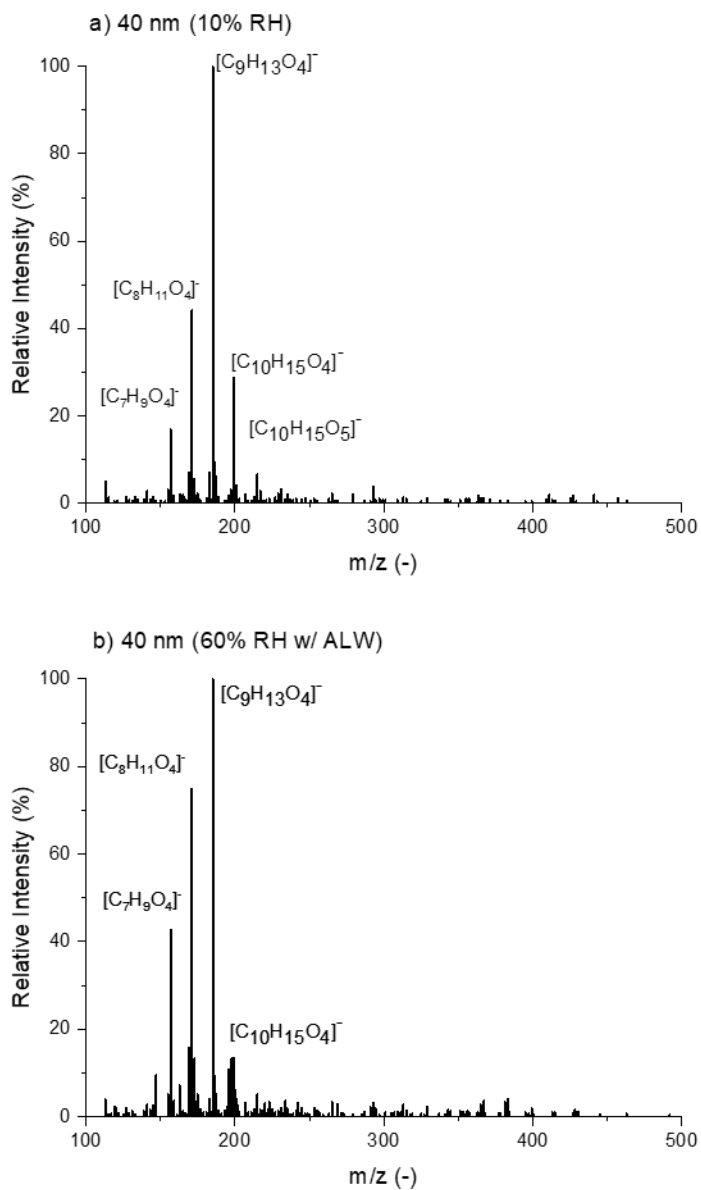


Figure 4-11. Mass spectra of collected particles exiting the flow tube. a) dry conditions (10% RH). b) high relative humidity (60% RH) with ALW.

Molecular composition measurements using HR-ESI-MS were done to determine the molecular species contributing to particle growth. This was done in a similar way to measurements done in Chapter 3 Krasnomowitz et al. (2019)<sup>21</sup>. Particles exiting the flow tube reactor were collected onto a quartz microfiber filter. Organic material was then extracted using acetonitrile and analyzed using a Q-Exactive Orbitrap mass spectrometer. Two measurements were done both with 40 nm initial diameter seed particles. However, the first collection was done under dry conditions (10%) and the second was done at 60% RH with seeds containing ALW. This allowed for determining any potential differences in composition unique to the enhanced growth of particles containing ALW. Mass Spectra from these collections are shown in Figure 4-11.

Overall, the mass spectra from the two experiments are incredibly similar. Both spectra are dominated by monomers, indicating that the condensable material is formed via the unimolecular HOM pathway (green pathway in Figure 4-8) rather than by  $\text{RO}_2$  -  $\text{RO}_2$  chemistry (red pathway in Figure 4-8). As in Chapter 3, the lack of dimers confirms that the elevated precursor mixing ratios used in the flow tube experiment are not leading to reaction pathways that are unimportant under ambient conditions. In this particular experiment, the lack of dimers is also noteworthy because it rules out particle-phase dimerization in the ALW as a mechanism for enhanced particle growth. Instead, the similarity of the two mass spectra in Figure 4-11 suggest that additional  $\alpha$ -pinene is being oxidized in the ALW experiment by a similar mechanism to the green pathway in Figure 4-8, perhaps on the liquid surface of the particle. The higher apparent yields below 50 nm indicate that there is something special about these particles with respect to surface oxidation of  $\alpha$ -pinene. This may

be related to the observation that phase separation between organic and inorganic components is observed only in particles above about 50 nm in diameter<sup>18</sup>.

#### **4.6 Conclusion**

This work examined the growth of ammonium sulfate seed particles by  $\alpha$ -pinene ozonolysis products under high relative humidity conditions and with seed particles containing ALW. Growth of dry particles was found to be independent of relative humidity, as the high RH experiments showed the same measured change in diameter as previously discussed dry experiments. However, a significant growth enhancement was observed when seed particles containing ALW were introduced to the flow tube reactor and exposed to the same conditions. This enhancement was greatest for seeds with diameters below 50 nm where the seeds are more likely to be homogeneous, but an enhancement was found to be present at all sizes when experiments were simulated using a kinetic model. A generalized reaction mechanism was proposed to describe the formation of molecular species that would describe the observed growth.

## REFERENCES

- (1) Komppula, M.; Lihavainen, H.; Hatakka, J.; Paatero, J.; Aalto, P.; Kulmala, M.; Viisanen, Y. *J. Geophys. Res. Atmos.* **2003**, *108* (D9), 4295.
- (2) Dusek, U.; Frank, G. P.; Hildebrandt, L.; Curtius, J.; Schneider, J.; Walter, S.; Chand, D.; Drewnick, F.; Hings, S.; Jung, D.; Borrmann, S.; Andreae, M. O. *Science* **2006**, *312* (5778), 1375–1378.
- (3) Komppula, M.; Lihavainen, H.; Kerminen, V. M.; Kulmala, M.; Viisanen, Y. *J. Geophys. Res. D Atmos.* **2005**, *110* (6), 1–10.
- (4) Lihavainen, H.; Kerminen, V.-M.; Komppula, M.; Hatakka, J.; AAltonen, V. *J. Geophys. Res.* **2003**, *108* (D24), 4782.

- (5) Jimenez, J. L.; Canagaratna, M. R.; Donahue, N. M.; Prevot, A. S. H.; Zhang, Q.; Kroll, J. H.; DeCarlo, P. F.; Allan, J. D.; Coe, H.; Ng, N. L.; Aiken, A. C.; Docherty, K. S.; Ulbrich, I. M.; Grieshop, A. P.; Robinson, A. L.; Duplissy, J.; Smith, J. D.; Wilson, K. R.; Lanz, V. A.; Hueglin, C.; Sun, Y. L.; Tian, J.; Laaksonen, A.; Raatikainen, T.; Rautiainen, J.; Vaattovaara, P.; Ehn, M.; Kulmala, M.; Tomlinson, J. M.; Collins, D. R.; Cubison, M. J.; Dunlea, J.; Huffman, J. A.; Onasch, T. B.; Alfarra, M. R.; Williams, P. I.; Bower, K.; Kondo, Y.; Schneider, J.; Drewnick, F.; Borrmann, S.; Weimer, S.; Demerjian, K.; Salcedo, D.; Cottrell, L.; Griffin, R.; Takami, A.; Miyoshi, T.; Hatakeyama, S.; Shimono, A.; Sun, J. Y.; Zhang, Y. M.; Dzepina, K.; Kimmel, J. R.; Sueper, D.; Jayne, J. T.; Herndon, S. C.; Trimborn, A. M.; Williams, L. R.; Wood, E. C.; Middlebrook, A. M.; Kolb, C. E.; Baltensperger, U.; Worsnop, D. R.; Dunlea, E. J.; Huffman, J. A.; Onasch, T. B.; Alfarra, M. R.; Williams, P. I.; Bower, K.; Kondo, Y.; Schneider, J.; Drewnick, F.; Borrmann, S.; Weimer, S.; Demerjian, K.; Salcedo, D.; Cottrell, L.; Griffin, R.; Takami, A.; Miyoshi, T.; Hatakeyama, S.; Shimono, A.; Sun, J. Y.; Zhang, Y. M.; Dzepina, K.; Kimmel, J. R.; Sueper, D.; Jayne, J. T.; Herndon, S. C.; Trimborn, A. M.; Williams, L. R.; Wood, E. C.; Middlebrook, A. M.; Kolb, C. E.; Baltensperger, U.; Worsnop, D. R.; Dunlea, E. J.; Huffman, J. A.; Onasch, T. B.; Alfarra, M. R.; Williams, P. I.; Bower, K.; Kondo, Y.; Schneider, J.; Drewnick, F.; Borrmann, S.; Weimer, S.; Demerjian, K.; Salcedo, D.; Cottrell, L.; Griffin, R.; Takami, A.; Miyoshi, T.; Hatakeyama, S.; Shimono, A.; Sun, J. Y.; Zhang, Y. M.; Dzepina, K.; Kimmel, J. R.; Sueper, D.; Jayne, J. T.; Herndon, S. C.; Trimborn, A. M.; Williams, L. R.; Wood, E. C.; Middlebrook, A. M.; Kolb, C. E.; Baltensperger, U.; Worsnop, D. R.; Dunlea, E. J.; Huffman, J. A.; Onasch, T. B.; Alfarra, M. R.; Williams, P. I.; Bower, K.; Kondo, Y.; Schneider, J.; Drewnick, F.; Borrmann, S.; Weimer, S.; Demerjian, K.; Salcedo, D.; Cottrell, L.; Griffin, R.; Takami, A.; Miyoshi, T.; Hatakeyama, S.; Shimono, A.; Sun, J. Y.; Zhang, Y. M.; Dzepina, K.; Kimmel, J. R.; Sueper, D.; Jayne, J. T.; Herndon, S. C.; Trimborn, A. M.; Williams, L. R.; Wood, E. C.; Middlebrook, A. M.; Kolb, C. E.; Baltensperger, U.; Worsnop, D. R. *Science* **2009**, 326 (5959), 1525–1529.
- (6) Hallquist, M.; Wenger, J. C.; Baltensperger, U.; Rudich, Y.; Simpson, D.; Claeys, M.; Dommen, J.; Donahue, N. M.; George, C.; Goldstein, a. H.; Hamilton, J. F.; Herrmann, H.; Hoffmann, T.; Iinuma, Y.; Jang, M.; Jenkin, M. E.; Jimenez, J. L.; Kiendler-Scharr, a.; Maenhaut, W.; McFiggans, G.; Mentel, T. F.; Monod, a.; Prévôt, a. S. H.; Seinfeld, J. H.; Surratt, J. D.; Szmigielski, R.; Wildt, J. *Atmos. Chem. Phys.* **2009**, 9 (14), 5155–5236.

- (7) Kulmala, M.; Kontkanen, J.; Junninen, H.; Lehtipalo, K.; Manninen, H. E.; Nieminen, T.; Petäjä, T.; Sipilä, M.; Schobesberger, S.; Rantala, P.; Franchin, A.; Jokinen, T.; Järvinen, E.; Äijälä, M.; Kangasluoma, J.; Hakala, J.; Aalto, P. P.; Paasonen, P.; Mikkilä, J.; Vanhanen, J.; Aalto, J.; Hakola, H.; Makkonen, U.; Ruuskanen, T.; III, R. L. M.; Duplissy, J.; Vehkamäki, H.; Bäck, J.; Kortelainen, A.; Riipinen, I.; Kurtén, T.; Johnston, M. V.; Smith, J. N.; Ehn, M.; Mentel, T. F.; Lehtinen, K. E. J.; Laaksonen, A.; Kerminen, V.-M.; Worsnop, D. R. *Science* **2013**, *339* (6122), 943–947.
- (8) Riipinen, I.; Pierce, J. R.; Yli-Juuti, T.; Nieminen, T.; Häkkinen, S.; Ehn, M.; Junninen, H.; Lehtipalo, K.; Petäjä, T.; Slowik, J.; Chang, R.; Shantz, N. C.; Abbatt, J.; Leaitch, W. R.; Kerminen, V. M.; Worsnop, D. R.; Pandis, S. N.; Donahue, N. M.; Kulmala, M. *Atmos. Chem. Phys.* **2011**, *11* (8), 3865–3878.
- (9) Ehn, M.; Thornton, J. A.; Kleist, E.; Sipilä, M.; Junninen, H.; Pullinen, I.; Springer, M.; Rubach, F.; Tillmann, R.; Lee, B.; Lopez-Hilfiker, F.; Andres, S.; Acir, I. H.; Rissanen, M.; Jokinen, T.; Schobesberger, S.; Kangasluoma, J.; Kontkanen, J.; Nieminen, T.; Kurtén, T.; Nielsen, L. B.; Jørgensen, S.; Kjaergaard, H. G.; Canagaratna, M.; Maso, M. D.; Berndt, T.; Petäjä, T.; Wahner, A.; Kerminen, V. M.; Kulmala, M.; Worsnop, D. R.; Wildt, J.; Mentel, T. F. *Nature* **2014**, *506* (7489), 476–479.
- (10) Jokinen, T.; Sipilä, M.; Richters, S.; Kerminen, V. M.; Paasonen, P.; Stratmann, F.; Worsnop, D.; Kulmala, M.; Ehn, M.; Herrmann, H.; Berndt, T. *Angew. Chemie - Int. Ed.* **2014**, *53* (52), 14596–14600.
- (11) Rissanen, M. P.; Kurtén, T.; Sipilä, M.; Thornton, J. A.; Kangasluoma, J.; Sarnela, N.; Junninen, H.; Jørgensen, S.; Schallhart, S.; Kajos, M. K.; Taipale, R.; Springer, M.; Mentel, T. F.; Ruuskanen, T.; Petäjä, T.; Worsnop, D. R.; Kjaergaard, H. G.; Ehn, M. *J. Am. Chem. Soc.* **2014**, *136* (44), 15596–15606.
- (12) Sihto, S. L.; Kulmala, M.; Kerminen, V. M.; Dal Maso, M.; Petäjä, T.; Riipinen, I.; Korhonen, H.; Arnold, F.; Janson, R.; Boy, M.; Laaksonen, A.; Lehtinen, K. E. J. *Atmos. Chem. Phys.* **2006**, *6* (12), 4079–4091.
- (13) Dada, L.; Paasonen, P.; Nieminen, T.; Buenrostro Mazon, S.; Kontkanen, J.; Peräkylä, O.; Lehtipalo, K.; Hussein, T.; Petäjä, T.; Kerminen, V. M.; Bäck, J.; Kulmala, M. *Atmos. Chem. Phys.* **2017**, *17* (10), 6227–6241.
- (14) Boy, M.; Kulmala, M. *Atmos. Chem. Phys.* **2002**, *2* (1), 1–16.
- (15) Hyvönen, S.; Junninen, H.; Laakso, L.; Dal Maso, M.; Grönholm, T.; Bonn, B.; Keronen, P.; Aalto, P.; Hiltunen, V.; Pohja, T.; Launiainen, S.; Hari, P.; Mannila, H.; Kulmala, M. *Atmos. Chem. Phys.* **2005**, *5* (12), 3345–3356.

- (16) Li, X.; Chee, S.; Hao, J.; Abbatt, J. P. D.; Jiang, J.; Smith, J. N. *Atmos. Chem. Phys.* **2019**, *19* (3), 1555–1570.
- (17) Faust, J. A.; Wong, J. P. S.; Lee, A. K. Y.; Abbatt, J. P. D. *Environ. Sci. Technol.* **2017**, *51* (3), 1405–1413.
- (18) Freedman, M. A. *Chem. Soc. Rev.* **2017**, *46* (24), 7694–7705.
- (19) Veghte, D. P.; Altaf, M. B.; Freedman, M. A. *J. Am. Chem. Soc.* **2013**, *135* (43), 16046–16049.
- (20) Altaf, M. B.; Freedman, M. A. *J. Phys. Chem. Lett.* **2017**, *8* (15), 3613–3618.
- (21) Krasnomowitz, J. M.; Apsokardu, M. J.; Stangl, C. M.; Tiszenkel, L.; Ouyang, Q.; Lee, S.; Johnston, M. V. *Aerosol Sci. Technol.* **2019**, *0* (0), 1–13.
- (22) Stangl, C. M.; Krasnomowitz, J. M.; Apsokardu, M. J.; Tiszenkel, L.; Ouyang, Q.; Lee, S.; Johnston, M. V. *J. Geophys. Res. Atmos.* **2019**, *124* (8), 4800–4811.
- (23) Tiszenkel, L.; Stangl, C.; Krasnomowitz, J.; Ouyang, Q.; Yu, H.; Apsokardu, M. J.; Johnston, M. V.; Lee, S.-H. *Atmos. Chem. Phys. Discuss.* **2019**, 1–21.
- (24) Horan, A. J.; Apsokardu, M. J.; Johnston, M. V. *Anal. Chem.* **2017**, *89* (2), 1059–1062.
- (25) Smith, M. L.; Kuwata, M.; Martin, S. T. *Aerosol Sci. Technol.* **2011**, *45* (2), 244–261.
- (26) Clegg, S. L.; Brimblecombe, P.; Wexler, A. S. *J. Phys. Chem. A* **1998**, *102* (12), 2137–2154.
- (27) Massucci, M.; Clegg, S. L.; Brimblecombe, P. *J. Phys. Chem. A* **2002**, *103* (21), 4209–4226.
- (28) Wexler, A. S.; Clegg, S. L. *J. Geophys. Res.* **2002**, *107* (D14).
- (29) Apsokardu, M. J.; Johnston, M. V. *Atmos. Chem. Phys.* **2018**, *18*, 1895–1907.

## Chapter 5

### CONCLUSIONS AND FUTURE DIRECTIONS

This dissertation describes laboratory investigations aimed to better understand growth of Aitken mode particles when exposed to  $\alpha$ -pinene oxidation products. Experiments were performed with a custom built flow tube reactor to expose seed particles to known concentrations of reactants and measure the corresponding growth. First, work was done under dry conditions to characterize the flow tube reactor. Particle residence times in the flow tube were determined both experimentally and using computational fluid dynamics (CFD). Residence time distributions of seed particles were measured using a condensation particle counter (CPC) while CFD calculations were done using COMSOL Multiphysics. Experimental results agreed well with modeling with both results concluding a particle residence time of approximately 4 minutes. These results allowed for quantitative growth experiments to be conducted by exposing seed particles to a known  $\alpha$ -pinene mixing ratio and incrementing through five different ozone mixing ratios. Increasing the ozone mixing ratio caused additional oxidation of  $\alpha$ -pinene, which increased the amount of low volatility products capable of condensing into the particle phase. Known reaction time and reactant concentrations allowed for the development of a kinetic model to determine the amount of condensable organic material needed to explain the observed particle growth. By eliminating all other variables other than the highly oxidized molecule (HOM) yield, it was possible to determine the yield of condensable molecules from  $\alpha$ -pinene ozonolysis. This value was experimentally determined to be

13±1%, a value that agrees well with other measurements of gas-phase HOM molecules.

In an effort to better simulate atmospheric conditions and determine the effect of relative humidity on particle growth, additional experiments were performed with a slightly modified experimental setup. Here, the make-up flow going into the flow tube reactor was sent through a water bubbler to control the RH in the reactor.

Additionally, a condensation growth chamber (CGC) was added after the seed particles were size-selected. This allowed for aerosol liquid water to be added onto the seed particles and study the growth of wet seeds. Results of these experiments show that RH alone does not have an effect on particle growth. However, when water was added to the seeds in a high RH environment, a growth enhancement was observed, with the enhancement being greatest at smaller seed sizes (below 50 nm). The observed increase in growth along with previously discussed kinetic modeling helped elucidate increased yields of condensable material for wet particles.

While the experimental work described in this dissertation may help improve climate models to better predict particle growth and CCN formation, the studies still represent relatively simple simulations of atmospheric conditions. Therefore, a wide variety of potential future studies exist. It is my hope that the experimental instrumentation and procedures described in this dissertation can be used to study a variety of natural and anthropogenic precursors that can be oxidized to produce condensable material. Such precursors include but are not limited to  $\beta$ -pinene, limonene, isoprene and Decamethylcyclopentasiloxane (D5). Different oxidation pathways besides ozonolysis can also be studied such as oxidation by OH. Additional

pollutants such as NO<sub>x</sub> can also be introduced to determine their corresponding effects on particle growth.

Another interesting follow up experiment would be to change the composition of the seed particles used to study particle growth. Ammonium sulfate seeds were used throughout all of the experiments in this dissertation since ammonium sulfate is atmospherically relevant and would be unreactive when dry. As the focus of experiments shifts and more complex mechanisms for particle growth are investigated, such as particle-phase chemistry, it may be beneficial to change the seed particle composition. One potential set of experiments would be changing the pH of these seed particles by adding additional sulfuric acid to the solution that is used to generate the aerosol. This will cause the seed particles to be more acidic, which may promote dimerization reactions of semivolatile organics that have partitioned into the particle phase, as these reactions have been shown to be acid catalyzed <sup>1</sup>. These results can then be compared to the previously discussed ammonium sulfate experiments to determine if any additional growth occurs due to the acidic conditions. Another potential seed particle composition is to move away from ammonium sulfate completely and instead use seeds made of fresh or aged secondary organic aerosol (SOA). This could be beneficial for a number of reasons. First, having seed particles similar to the material condensing from the gas-phase could make for more homogeneous particles after growth has occurred, which as discussed in Chapter 4, may promote reactions within the particle phase and enhance growth rates. Second, this could provide additional reactants for the particle phase reactions causing an even greater enhancement to be observed.

Additional experiments would also be beneficial to learn more about some of the particles discussed in this dissertation. First, particle morphology measurements would help to confirm the hypothesis that particle phase separations are occurring in the larger seed sizes and resulting in less growth enhancement for the seed particles containing aerosol liquid water (ALW). These measurements have been done previously using cryogenic transmission electron microscopy (cryo-TEM) to image the particles<sup>2-4</sup> and have shown that it is possible to observe phase separations using the technique. These measurements would give more information on the morphology of the particles. It will be possible to see if multiple phases are present within the particle, and if one phase is fully engulfed by the other (one phase surrounding the second) or only semi-engulfed (one phase protruding from the other). It will also be possible to see if particles are spherical or have more complex shapes, for a better understanding on how well the spherical shape assumed by SMPS measurements relate to the real particles.

Since cryo-TEM is an offline technique, particles would need to be sampled exiting the flow tube and then measured. Sampling particles for TEM cannot be done the same way as previously described for molecular composition measurements as the filter used there would cause interference and not allow the particles to be effectively imaged. However, a number of different sampling techniques are possible to deposit particles onto a TEM grid, a more effective substrate for these types of measurements. First particles could be deposited onto grids using a cascade impactor. Second, particles could be collected using an instrument such as the TSI Nanometer Aerosol Sampler which attracts charged particles to the TEM grid by placing the grid on top of a high-voltage electrode. Finally, particles could be collected onto a grid using

thermophoretic sampling<sup>5</sup>. This technique has been shown to be a softer deposition that relies on the pressure difference created by warming and cooling opposite sides of the flow path. The particles are then guided towards a grid where deposition occurs. A number of these sampling techniques should be utilized so an optimized collection method can be created, allowing for high quality morphology measurements by cryo-TEM.

Another useful improvement to the experiments described here would be online molecular composition of particles exiting the flow tube. This would be helpful for a number of reasons. First, the length of experiments would be cut down significantly. Instead of collecting particles for measurement over a period of hours to days, spectra would instead be collected in real time allowing for much faster analysis. An additional advantage to this is the short time period over which the measurements take place. This means molecules have a much shorter time period to decompose giving a more accurate representation of the true particle composition. Additionally, no sample prep is needed for online measurements removing any potential bias added in during that process. A technique to perform these online molecular measurements is currently being developed and optimized<sup>6,7</sup>. Droplet assisted ionization (DAI) is a newly developed method of ionization that would allow for direct measurement of particles exiting the flow tube reactor. A Waters SYNAPT G2-S time-of-flight mass spectrometer has been adapted to perform DAI in my research group's laboratory. For ionization to occur, particles are first sent through the CGC as wet particles have been shown to ionize better than dry particles. The particles are then sent through a temperature controlled capillary inlet that has been fixed to the source region of the mass spectrometer. The inlet can be heated to a maximum of 850 °C. Passing

particles through the heated capillary causes fast evaporation of solvent resulting in an ionization mechanism similar to that of electrospray ionization. Mass spectra obtained are very similar to those obtained with electrospray ionization, but with the advantages of online analysis and the ability to measure molecular species at near atmospherically relevant mass concentrations. Current work is focused on optimizing experimental conditions of DAI to best detect common molecular species in SOA. Once optimized, direct measurements of particles exiting the flow tube reactor will have many benefits over offline composition measurements as discussed above.

The work presented in this dissertation outlines the framework and foundation of studies to better understand processes impacting aerosol growth in the Aitken mode. This work has potential to improve predictions of CCN concentrations in climate models and improve our overall understanding of climate change. The experiments described here also represent a great framework for additional studies of increasingly complex particle growth mechanisms.

## REFERENCES

- (1) Casale, M. T.; Richman, A. R.; Elrod, M. J.; Garland, R. M.; Beaver, M. R.; Tolbert, M. A. *Atmos. Environ.* **2007**, *41* (29), 6212–6224.
- (2) Altaf, M. B.; Freedman, M. A. *J. Phys. Chem. Lett.* **2017**, *8* (15), 3613–3618.
- (3) Freedman, M. A. *Chem. Soc. Rev.* **2017**, *46* (24), 7694–7705.
- (4) Veghte, D. P.; Altaf, M. B.; Freedman, M. A. *J. Am. Chem. Soc.* **2013**, *135* (43), 16046–16049.
- (5) Leith, D.; Miller-Lionberg, D.; Casuccio, G.; Lersch, T.; Lentz, H.; Marchese, A.; Volckens, J. *Aerosol Sci. Technol.* **2014**, *48* (1), 81–89.
- (6) Horan, A. J.; Apsokardu, M. J.; Johnston, M. V. *Anal. Chem.* **2017**, *89* (2), 1059–1062.
- (7) Apsokardu, M. J.; Kerecman, D. E.; Johnston, M. V. *Rapid Commun. Mass Spectrom.* **2018**.

**Appendix A**  
**LIST OF ACRONYMS**

ALW – Aerosol liquid water

BVOC – Biogenic volatile organic compound

CCN – Cloud condensation nuclei

CFD – Computational fluid dynamics

CGC – Condensation growth chamber

CI – Criegee intermediate

CI-APi-TOF - Chemical ionization in an atmospheric pressure interface time-of-flight mass spectrometer

CLOUD – Cosmics Leaving Outdoor Droplets

CPC – Condensation particle counter

Cryo-TEM – Cryogenic transmission electron microscopy

CS – Condensation sink

DAI – Droplet assisted ionization

DMA – Differential mobility analyzer

DRH – Deliquescence relative humidity

E-AIM – Extended-aerosol inorganic model

ELVOC – Extremely low volatility organic compound

ERH – Efflorescence relative humidity

HOM – Highly oxidized molecule

HR-ESI-MS - High resolution electrospray mass spectrometry

LIPI – Laser induced plasma ionization  
LVOC – Low volatility organic compound  
NAMS – Nanoaerosol mass spectrometer  
NPF – New particle formation  
NVOC – Nonvolatile organic compound  
RH – Relative humidity  
sCI – Stabilized Criegee intermediate  
SMPS- Scanning mobility particle sizer  
SOA – Secondary organic aerosol  
SVOC – Semivolatile organic compound  
TOF – Time of flight  
VBS – Volatility basis set  
VOC – Volatile organic compound

## Appendix B

### COPYRIGHTS

#### Chapter 3

Parts of text and figures are reprinted or adapted with permission from:

Justin M. Krasnomowitz, Michael J. Apsokardu, Christopher M. Stangl, Lee Tiszenkel, Qi Ouyang, Shanhu Lee & Murray V. Johnston (2019) Growth of Aitken mode ammonium sulfate particles by  $\alpha$ -pinene ozonolysis, *Aerosol Science and Technology*, 53:4, 406-418, DOI: 10.1080/02786826.2019.1568381



The screenshot displays the RightsLink interface. At the top left is the Copyright Clearance Center logo. To its right is the RightsLink logo. Further right are navigation buttons for Home, Create Account, and Help, along with an envelope icon. Below the logo area is a box for Taylor & Francis, including the journal title 'Aerosol Science and Technology'. The main content area lists the following metadata:

- Title:** Growth of Aitken mode ammonium sulfate particles by  $\alpha$ -pinene ozonolysis
- Author:** Justin M. Krasnomowitz, , , et al
- Publication:** Aerosol Science & Technology
- Publisher:** Taylor & Francis
- Date:** Apr 3, 2019

Below the metadata, it states 'Rights managed by Taylor & Francis'. On the right side of the interface, there is a LOGIN button and a text box that reads: 'If you're a copyright.com user, you can login to RightsLink using your copyright.com credentials. Already a RightsLink user or want to [learn more?](#)'

#### Thesis/Dissertation Reuse Request

Taylor & Francis is pleased to offer reuses of its content for a thesis or dissertation free of charge contingent on resubmission of permission request if work is published.

BACK

CLOSE WINDOW

Copyright © 2019 Copyright Clearance Center, Inc. All Rights Reserved. [Privacy statement](#). [Terms and Conditions](#).  
Comments? We would like to hear from you. E-mail us at [customer@copyright.com](mailto:customer@copyright.com)